Molecular mechanisms of macroscopic ductility within brittle epoxy resins

Vom Promotionsausschuss der
Technischen Universität Hamburg

zur Erlangung des akademischen Grades

Doktor-Ingenieurin (Dr.-Ing.)

genehmigte Dissertation (Monografie)

von
Janina Mittelhaus
aus Bad Reichenhall

2025

Vorsitzender des Prüfungsausschusses:	Prof. Dr. habil. Michael M. Morlock (Technische Universität Hamburg)
Gutachter:	Prof. Dr.-Ing. habil. Bodo Fiedler (Technische Universität Hamburg)
	Prof. Dr. tech. Essi Sarlin (Tampere University Finland)
Tag der mündlichen Prüfung:	27.06.2025

Technisch-Wissenschaftliche Schriftenreihe

Herausgeber:
Prof. Dr.-Ing. habil. Bodo Fiedler

Anschrift:
Technische Universität Hamburg
Institut für Kunststoffe und Verbundwerkstoffe
Denickestraße 15
21073 Hamburg

Band 49:
Molecular mechanisms of macroscopic ductility within brittle epoxy resins

Janina Mittelhaus
1. Auflage
Hamburg 2025

ISSN 2625-6029

Bibliographische Information der Deutschen Nationalbibliothek: Die deutsche Nationalbibliothek verzeichnet diese Publikation in der Deutschen Nationalbibliothek; detaillierte Informationen sind im Internet über dnb.de abrufbar.

Acknowledgements

First and foremost, I would like to thank Prof. Dr.-Ing. habil. Bodo Fiedler for his guidance and support of this research. Numerous discussions and the freedom during the research have led to the success of the work. Furthermore, I would like to thank Prof. Essi Sarlin for taking on the position of second assessor and Prof. Dr. Michael M. Morlock in his function of chairman.

Great thanks go to all colleagues from the Institute of Polymer and Composites for the highly friendly working atmosphere and the many inspiring discussions. I would especially like to thank Phil Röttger, Julius Jacobs, Jonas Drummer, Dennis Gibhardt, Melissa Walter, Tobias Tiedemann, Julian Karsten and Marcel Neubacher for the numerous scientific discussions and the joint research. The last few years have been a great time. The work was related to the project „Mechanisms of thermoset plasticity explained on the basis of spectroscopic analysis and atomistic simulations“ (Project number 525597740) funded by German Research Foundation (DFG) which was worked on jointly with Prof. Robert Meißner and Dr. Julian Konrad (TUHH, Institute of soft matter modeling). I would like to thank both for the great joint research and for the valuable scientific exchange.

Part of the work was also done in collaboration with the University Tampere. I would like to thank Prof. Essi Sarlin for the opportunity of a research stay and all members of her great work group, for the experimental support, the many helpful discussions and the warm welcome. In particular, I also thank Asst. Prof. Gaurav Mohanty, Suprit Bhusare, Matti Isakov and Turkka Salminen from the Tampere University for the great scientific collaboration.

In addition, I would like to thank Dr. Holger Schmalz (BPI, University of Bayreuth) for performing Raman measurements for this project and Dr. Florian Bittner (IKK, Leibniz University Hannover) for supporting this thesis with µCT measurements.

And I would also like to thank Assoc. Prof. Masaaki Nishikawa (Dept. of Mechanical Engineering and Science, Kyoto University, Japan) and Dr. Benedikt Kötter (CompriseTec) for performing cyclic and creep tests on epoxy film samples.

Additionally, I would like to say thank you to all students I supervised for their work, which contributed a lot to the success of the research experiments.

I would like to thank my parents, Hans-Josef and Ute for their indefatigable assistance and encouragement during my whole education. And I would like to thank my sister Jessica for her creative advices. I would also like to thank my brother-in-law Malte for the material science discussions and interest in my work. And I would like to thank my parents-in-law Rita and Stefan for their lovely support over the last years.

Finally, I like to thank my lovely husband Tristan. I would like to thank him for his incredible support, his caring, and understanding over the last years. This project would not have been possible without him!

The finnish word '*sisu*' means an inner strength to go beyond present limitations, take actions against all odds and transform barriers into opportunities.
In my opinion, *sisu* describes the requirements for successful scientific research and was therefore my guidance for this thesis.

Kurzfassung

Verschiedene Studien zeigen, dass das mechanische Verhalten von Epoxidharzen neben der Testtemperatur, des Belastungsfalls und der Prüfgeschwindigkeit auch vom Volumen abhängt. Dieser sogenannte Größeneffekt (engl. *size effect*) zeigt sich bei Epoxidharzen mit einer erwarteten Zunahme der Festigkeit bei Abnahme des Volumens. Gleichzeitig kommt es auch zu einer signifikanten Erhöhung der Duktilität mit abnehmendem Prüfvolumen. Damit unterscheidet sich das Verformungsverhalten von mikroskaligen Epoxidharzen, wie sie beispielsweise als Matrixbereiche zwischen den Fasern in Faser-Kunststoff-Verbunden (FKV) vorliegen können, signifikant von dem klassisch spröden Verhalten von Standard Proben mit vergleichsweise großen Prüfvolumina.

Bisher gibt es jedoch keine umfassende physikalische, mechanisch-chemische oder molekulare Erklärung für dieses erhöhte duktile Verformungsvermögen von mikroskaligen Epoxidharzbereichen. Aus diesem Grund wurde ihm Rahmen der vorliegenden Promotion das mechanische Verhalten und die zugrundeliegenden molekularen Mechanismen von Epoxidharzfolien unter Zuglast mit im Vergleich zu Standardproben stark reduziertem Prüfvolumina untersucht. Dafür wurde zunächst ein geeignetes Verfahren zur Herstellung von Folien mit einer Dicke zwischen 15 bis 100 µm entwickelt und optimiert. Die hergestellten Folien wurden zunächst mittels Dynamische Differenzkalorimetrie (DSC) und Nahinfrarot-Spektroskopie (NIR) untersucht, um eine nahezu vollständige Vernetzung sicherzustellen. Dabei konnten keine Hinweise auf eine unvollständige Vernetzung gefunden werden. Durch anschließendes Stanzen und Laserschneiden der Folien erfolgte die Probenformgebung.

Zur Aufklärung der Zusammenhänge zwischen dem ausgeprägten Verformungsvermögen und der mikrostrukturellen Vorgänge wurden die so erzeugten Proben in Zug-, Kriech, Ermüdungs- und Relaxationsversuchen mechanisch und spektroskopisch analysiert.

Die belasteten Proben zeigten erhebliche Einschnürungen und es bilden sich Scherbänder mit im Vergleich zur Ausgangsdicke reduzierter Dicke aus, welche mittels spannungsoptischer Mikroskopaufnahmen nachgewiesen werden. Es konnte gezeigt werden, dass die Duktilität mit abnehmender Probendicke bzw. verringertem Prüfvolumen signifikant zunimmt. Folienproben mit einem Prüfvolumen von $0.06\,\mathrm{mm}^3$ erreichten im Zugversuch Bruchdehnungen von bis zu 80 %, was signifikant erhöht ist im Vergleich zu den im Rahmen der Arbeit untersuchten Standard Proben vom Typ 1BA mit einem Prüfvolumen von $500\,\mathrm{mm}^3$ (5-12 % Bruchdehnung). Außerdem zeigten sich in den Spannungs-Dehnungs-Kurven der Folien Proben Dehnungserweichungs- und Kaltverfestigungsmechanismen während des Verformungsvorgangs.

Mit spektroskopischen Methoden wurden parallel zu den makroskopischen die molekularen Vorgänge analysiert. Durch polarisierte Raman und Infrarot (IR) Messungen konnte eine molekulare Orientierung der Hauptketten in Lastrichtung nachgewiesen werden. Dies erklärt die Spannungsab- und -zunahme nach dem Erreichen der Fließspannung im Zugversuch, da die Ketten sich „entschlaufen“ und in Lastrichtung ausrichten. Nachdem die Spannung durch die Molekülbewegungen teilweise abgebaut wurde und sich in einigen Probenbereichen makroskopisch sichtbare Scherbänder gebildet haben, steigt die Spannung aufgrund der Verfestigungswirkung der in Zugrichtung ausgerichteten Molekülketten innerhalb der deformierenden Probe wieder an.

Hochauflösende mikroskopische IR Untersuchungen haben außerdem gezeigt, dass innerhalb der verformten Probenbereichen in den Scherbändern die aromatische Kohlenstoffverbindungen in den Hauptketten verstreckt vorliegen, was sich in einer Peak Verschiebung (engl. *Peak Shift*) zu geringeren Wellenzahlen zeigt. Es kommt demnach im Anschluss an die Orientierung auch zu einer messbaren Dehnung der Molekülketten in Zugrichtung.

Mittels Digitalen Bildkorrelations-Untersuchungen (DIC) konnte bestätigt werden, dass es insbesondere in den Scherbändern zu hohen lokalen Dehnungen und Verformungen kommt. IR Messungen ermöglichten zudem eine direkte Korrelation der aromatischen und spannungs-sensitiven Peak Wellenzahl und makroskopischer Dehnung. Dies ermöglichte die Untersuchung der im Epoxidharz vorliegenden Spannungszustände bei verschiedenen externen mechanischen Belastungen.

Zur Validierung wurden die mechanisch belasteten und verformten Proben oberhalb der Glasübergangstemperatur ausgelagert. Dabei konnten die eingeschnürten Proben wieder in ihre Ausgangsform zurückgeführt werden und die Scherbänder vollständig eliminiert werden. Nach der thermischen Auslagerung, liegen die molekularen Hauptketten wieder in einem amorphen, unverstreckten Zustand ohne Fernordnung vor. Bei einer erneuten Belastung nach thermischer Rückführung, entstanden die Scherbänder und Einschnürungen wieder in gleicher Art und Weise. Die hohe Duktilität von vollständig vernetzten Epoxidharzen kann somit durch reversible molekulare Strukturänderungen in Form von Ausrichtung und Strecken der Molekülketten insbesondere im Bereich der aromatischen Strukturen erklärt werden.

Die vorliegende Promotion bietet damit wertvolle Erkenntnisse in die durch ebene Spannungszustände begünstigten molekularen Vorgänge in mikroskopischen Prüfvolumina, welche zu einem erhöhten Verformungsvermögen von Epoxidharzen führen. Demnach sollten zukünftig für noch genauere FKV Modellierungen und Auslegungen in mikroskalaren Bereichen nicht die mechanischen Kennwerte von Standard- bzw. Norm-Probenkörpern verwendet werden, sondern die Kennwerter von mikroskopischen Proben, um das Materialverhalten von Epoxidharzen richtig zu berücksichtigen. Zudem könnte in kritischen FKV-Bereichen gezielt das Harzvolumen reduziert und damit die Verformbarkeit lokal erhöht werden.

Abstract

Various studies show that the mechanical behavior of epoxy resins depends not only on the test temperature, the load case, and the test speed, but also on the test volume. This so-called *size effect* is evident in epoxy resins with an expected increase in strength. At the same time, there is also a significant increase in ductility as the test volume decreases. This means that the deformation behavior of microscale epoxy resins, such as the matrix areas between the fibers in fiber-reinforced polymers (FRPs), differs significantly from the classic brittle behavior of standard bulk samples with comparatively large test volumes.

However, to date, there is no comprehensive physical, mechanical-chemical, or molecular explanation for this increased ductile deformation capacity of microscale epoxy samples. For this reason, as part of this thesis, the mechanical behavior and underlying molecular mechanisms of epoxy resin films under tensile load were investigated with a greatly reduced test volume compared to standard samples. For this purpose, a suitable process was first developed and optimized to manufacture films with a thickness between 15 and 100 µm. The films produced were first examined using differential scanning calorimetry (DSC) and near-Infrared spectroscopy (NIR) with respect to their crosslinking behavior. No evidence of incomplete cross-linking was found. The samples were then shaped by punching and laser cutting the films.

To clarify the relationships between the pronounced deformation capability and microstructural processes, the epoxy film samples were analyzed mechanically and spectroscopically in tensile, creep, fatigue, and relaxation tests. The loaded samples showed considerable necking and shear bands with a reduced thickness compared to the initial thickness. Shear bands were detected by photoelastic imaging. Ductility increased significantly with decreasing specimen thickness or reduced test volume.

Film samples with a test volume of 0.06 mm^3 achieved elongations at break of up to 80 % in tensile tests, which is significantly higher compared to standard bulk type 1BA samples with a test volume of 500 mm^3 (5-12 % elongation at break) investigated in this study. In addition, the stress-strain curves of the film samples showed strain softening and hardening mechanisms during the deformation process.

Spectroscopic methods were employed to analyze the molecular processes of macroscopic deformation. Polarized Raman and Infrared (IR) measurements revealed a molecular orientation of the main chains in the load direction. This explains the decrease and increase in stress after reaching the yield stress in the tensile test, as the chains "entangle" and align themselves in the load direction. After the stress has been partially relaxed by the molecular movements and macroscopically visible shear bands have formed, the stress increases again due to the strengthening effect of the molecular chains aligned in the tensile direction within the deformed sample.

High-resolution microscopic IR investigations have also shown that within the deformed sample areas in the shear bands, the carbon bonds of the aromatics in the main chains are stretched, which is reflected in a peak shift towards lower wavenumbers. Following the orientation, there is therefore also a measurable elongation of the main molecular chains in the tensile direction.

Digital image correlation (DIC) studies confirmed that high local strains and deformations occur particularly in the forming shear bands. *In situ* IR measurements also enabled a direct correlation of the decrease in the aromatic and stress-sensitive peak wavenumber with increasing macroscopic strain during mechanical tests. This allowed investigation of the stress states present in the epoxy under different external mechanical loads.

For validation, the mechanically loaded and deformed samples were stored in an oven above the glass transition temperature T_g. This allowed the constricted samples to return to their original shape and the shear bands to be eliminated. After thermal annealing, the molecular main chains returned to an amorphous, undeformed state without long-range order. The shear bands and constrictions reappeared in the same way when the material was mechanically loaded again after thermal annealing.

The high deformation ability of fully cross-linked epoxy can therefore be explained by reversible molecular structural changes in the form of alignment and stretching of the molecular chains, particularly in the area of the aromatic structures.

The present doctoral thesis thus offers valuable insight into the molecular processes in microscopic test volumes that are favored by plane stress states and lead to an increased deformation capacity of epoxies. For even more accurate FRP modeling and design in microscale areas, the parameters of microscopic epoxy samples should be used instead of the mechanical properties of bulk epoxy samples to exploit the full potential of epoxies. In addition, the epoxy volume could be specifically reduced in critical areas of FRP, increasing the deformability locally.

Contents

List of abbreviations

Abbreviation	**Definition**
FKV	Faser-Kunststoff-Verbund
FRP	Fiber-reinforced polymer
DGEBA	Diglycidyl ether of bisphenol A
RIM 134	Epoxy resin
RIM 137	Curing agent
HBPA-DGE	Hydrogenated bisphenol A epoxy resin
SANS	Small-angle neutron scattering
WAXS	Wide-angle X-ray scattering
AFM	Atomic force microscopy
RT	Room temperature ($23 \pm 2\,^{\circ}\mathrm{C}$)
T_g	Glass transition temperature
STZ	Shear transformation zone
FTIR	Fourier Transform Infrared spectroscopy
IR	Infrared (spectroscopy)
FIR	Far-Infrared (spectroscopy)
MIR	Mid-Infrared (spectroscopy)
NIR	Near-Infrared (spectroscopy)
ATR	Attenuated Total Reflection
DIC	Digital Image Correlation
DSC	Differential Scanning Calorimetry
RTM	Resin Transfer Molding
µ-CT	Micro-Computer Tomography
UTS	Ultimate Tensile Strength

Symbol	Definition
$A(\tilde{v})$	Absorbance at a specific wavenumber
$a(\tilde{v})$	Absorptivity at $\tilde{v}$
α	Molecular polarizability
α_0	Polarizability of a bond at the equilibrium atomic distance R_e
$\beta(\tilde{v})$	Linear absorption coefficient at $\tilde{v}$
$\vec{b}$	Burgers vector
C_i	Concentration of a component i
c	Speed of light
E_0	Amplitude of the oscillation
E_B	Bonding energy
E_{act}	Energy barrier for 1 mol molecular chain segments
E_{el}	Electric field
E_{photon}	Photon energy
$E_{pl,nu}$	Non-uniform plastic energy
$E_{pot}(R)$	Potential energy of a diatomic molecule as a function from the bond distance
$E_{vib,h}$	Harmonic vibration energy
E_1/E_2	Energetic state 1 and 2
E	Young's modulus in MPa
F	Force in N
G	Shear modulus in MPa
GC	Gas constant
ϵ_b	Elongation at break in %
ϵ_G	Global strain in %
h	Planck's quantum of action
k_{AB}	Force constant of a bond between atom A and B
k	Bond force constant
λ	Wavelength
m_r	Reduced mass of a two atomic molecule
μ	Dipole moment

Continued on the next page

Symbol	**Definition**
N	Number of atoms in a molecule
Q	Normal coordinate
R_{AB}	Bond lengths or distance between atom A and B
R_e	Equilibrium bond length or distance
R	(Current) bond length or distance
r_{y1}	Plane-strain plastic zone radius
r_{y2}	Plane-stress plastic zone radius
S	Entropy
σ	Stress in MPa
σ_1	Principal stress in plane 1
σ_2	Principal stress in plane 2
σ_3	Principal stress in plane 3
σ_y	Uniaxial yield stress in MPa
t	Time in s
T	Temperature
$T(\tilde{v})$	Transmittance at a specific wavenumber
τ_y	Shear yield stress in MPa
U	Internal energy
UTS	Tensile strengths in MPa
v	Frequency
v_0	Frequency of incident Raman laser beam
v_m	Frequency of the molecules interacted with the laser
$\tilde{v}$	Wavenumber in cm^{-1}
$\tilde{v}_{Peak}$	Wavenumber in cm^{-1} associated with a specific peak (maximum)
ϑ_i	Vibrational quantum number
$\dot{\epsilon}_0$	Strain rate before yield point
$\dot{\epsilon}_y$	Strain rate after yield point

1 Introduction

1.1 Structure of composites

Fiber-reinforced polymers (FRPs) can often be found in industrial applications that require excellent mechanical performance at low weight, e.g. in aviation or automotive industry. The structure of FRPs consists of oriented fibers surrounded by a continuous matrix material, such as an epoxy resin system. This results in a structure with areas of matrix materials that are in the sub-micrometer range, such as zones between fibers (1-25 µm, intralayer) and between reinforcing prepregs or layers (10-200 µm, interlayer) [1] as can be seen in Figure 1.1. The standard characterization of matrix materials is usually performed using macroscopic test volumes such as those specified in the standardized test methods ASTM D638 and DIN EN ISO 527. Accordingly, when modeling FRPs, it is often assumed that the epoxy-based matrix has bulk mechanical properties. However, the mechanical parameters of standard samples as input for the micromodeling of composites can lead to insufficient agreement between the modeled and the experimentally observed behavior, since the mechanical behavior of the microscopic epoxy matrix differs from that of the macroscopic standard samples [1–4]. Beside geometrical constraints, this might be due to the deviation of the mechanical behavior of the microscopic matrix from the macroscopic standard bulk specimens.

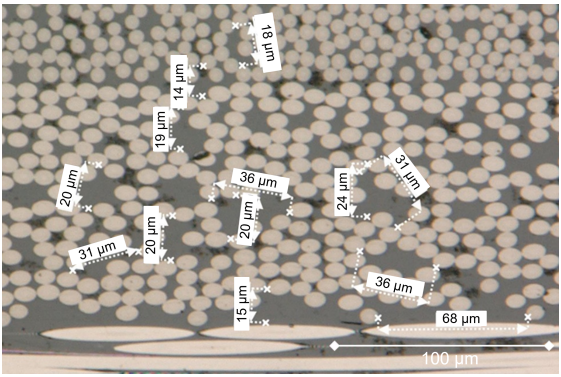

Figure 1.1: Micrograph of a carbon-fiber reinforced polymer with epoxy matrix and different fiber orientations per prepreg layer. The matrix material in the FRP is in the (sub-) micrometer range, such as resin-rich zones between fibers (intralayer) and between reinforcing prepregs or layers (interlayer)

1.2 Aims and scope

The ductility and plasticity of an archetypical brittle epoxy matrix is increased by reducing the gauge volume [1, 5–7]. However, to date, there is no complete physical, mechanochemical or molecular explanation for the observed size effect regarding the increasing deformation ability and the molecular mechanisms causing the deformation process.

In order to analyze this phenomenon, research hypotheses are formulated as separate working assumptions that can be investigated experimentally:

1. *Micro-scaled thin epoxy resin films can deform ductile under tensile loads.*
2. *High local strains and stress results in shear bands as visible deformation mechanisms under tensile loads.*
3. *Vibrational spectroscopic analysis can be performed to correlate the molecular mechanisms within epoxy with the macroscopic mechanical behavior.*
4. *The ductility in epoxy is enabled by molecular rearrangement processes in the cross-linked network.*
5. *Shear bands represent deformation areas with oriented and stretched molecular backbones in epoxy.*

6. *Shear bands and constricted regions in epoxy regress at temperatures above the glass transition temperature. The molecular structure then returns to a more favorable equilibrium conformation, and the sample returns in the initial geometric dimensions.*

Since the mechanical properties of a material are manifested in the way individual bonds within the materials respond to the applied macroscopic stress [8], Infrared (IR) and Raman spectroscopy and microscopy can be used to analyze stress-sensitive bonds within the material. By using the interaction of electromagnetic waves with epoxy materials, the load-induced deformation mechanisms of materials on a microstructural level can be investigated and insights into the molecular causes of their mechanical properties can be gained [9, 10]. It was found that during mechanically induced stretching of the carbon skeleton in molecules, the associated vibration frequency corresponding to the maximum of specific IR peaks decreases [11–16]. This behavior is explained by changes in the molecular structure and this approach is often used when studying composite materials [2, 17–23]. This indirect measurement method has also been applied, for example, to aramid, carbon, poly(p-phenylene-2,6-benzobisoxazole) (PBO) and polyethylene terephthalate (PET) fibers [24–30] or to biomaterials such as cellulose [31–35], silkworms [36] and spider silk [37]. To apply this method also to the complex 3D cross-linked thermoset and to get a deeper insight for epoxy, suitable thin microscale film samples are required. Therefore, a new manufacturing process for epoxy films with different, adjustable and reproducible thicknesses was developed. Care was taken with the film thicknesses selected to ensure that they are sufficiently thin to avoid total absorbance in IR transmission measurements. Only with sufficient IR transmittance, it is possible to acquire all spectral information.

These films were investigated by differential scanning calorimetry (DSC) and near-Infrared (NIR) spectroscopy with regard to the degree of cross-linking to ensure a maximal reaction between the resin and the curing agent despite the large surface-to-volume ratio.

The mechanical behavior was determined by tensile, creep, cyclic and relaxation tests. For film samples, with a comparably small gauge volume, a very sensitive load cell and a suitable micro tensile test device is necessary to investigate the mechanical behavior.

Performing tensile tests with an appropriate setup allows accurate measurement of changes in force (stress) due to molecular processes inside the epoxy material.

Photoelastic imaging and microscopy can be used to visualize deformation zones with shear bands. The strain analysis can be done by applying the digital image correlation (DIC) technique, where the (surface) deformation of the test specimen is observed during the test based on tracking a random speckle pattern on the sample surface. This approach has been used for several FRPs with epoxy matrix [38–43] to analyze the interphase and to correlate the local deformation mechanisms with the macroscopic mechanical parameters and was therefore used for epoxy films in this thesis as well.

To investigate the molecular orientation processes that lead to the local and global mechanical response to external stress, polarized IR and Raman spectroscopy can be used. In particular, polarized vibrational spectroscopy allows the analysis of polymer backbone orientations [5, 44–50]. The technique is usually applied to semi-crystalline polymer films, surfaces and fibers, like poly(ethylene terephthalate) [51–54], polyethylene [55] and polypropylene [56]. In this study, polarized vibrational spectroscopic measurements of the shear bands and of the constricted regions of the deformed and tensile-loaded epoxy film specimens were performed. The purpose was to analyze the molecular changes and associated local deformations in these regions. This facilitates the observation of presumed unraveling of entanglements, molecular alignment, and bond stretching due to the applied tensile load.

A combination of all these methods can provide a detailed insight into the micromechanical properties of epoxy matrix as a micro-component of composites and to do so, answer the research hypothesis of this doctoral thesis. This is important for the future matrix material development, the design and performance of polymeric composites.

Furthermore, as multiscale modeling of composite materials becomes more popular and essential for the industry, it is necessary to fully understand the increased plastic deformation ability on (sub-)micrometer scales, as usually occurs in composites, and the underlying mechanisms in epoxy.

2 Scientific and technological background

2.1 Deformation of materials

The mechanical behavior of a material is characterized on the molecular level by the reaction of molecular bonds and on the macroscopic level by the deformation process resulting from external forces. In the case of polymers made from macromolecules, a distinction is made between three components of a deformation that mainly overlap: elastic deformation (spontaneous, completely reversible), viscoelastic or relaxing deformation (time-dependent, completely reversible) and viscous or plastic deformation (time-dependent, not reversible) [57].

From a thermodynamic point of view, two types of resistance can be distinguished in the deformation of polymers under the action of an external force: the change in the internal energy ΔU and the entropy ΔS. Two ideal limiting cases of the reversible polymer deformation are the energy-elastic state (amorphous and crystalline structure) and the entropy-elastic state (amorphous structure), whereby the former takes place below the glass transition temperature T_g and the position of macromolecules is determined by a balance of forces of attraction and repulsion. When an external force is applied below T_g, the state of order (characterized by the entropy ΔS) does not change, but the internal energy ΔU as the elastic deformation of polymer materials under load is based on reversible changes in the atomic distances and the valence angles of the chemical bonds. The atoms carry out small thermal vibrations around the rest position R_e. Rearrangements of entire chain parts, which are the prerequisite for viscous deformation, are rare at temperatures below T_g. Rearrangements of molecular segments, rotations of C-C bonds, especially of the backbone, slippage of entanglements, or conformation changes are practically not possible at temperatures below T_g as well. That is why the polymer is brittle and hard at lower temperatures. Often these types of polymers are called glassy, such as thermosets like epoxies, which are usually in an energy-elastic state at room temperature (RT) [57].

In contrast, in the entropy-elastic state (normally above T_g), the polymers become more ductile. In the amorphous phases, previously hindered movement of the macromolecules or their sections is made possible. Entanglements are no longer fixed, and with less intermolecular interaction with neighboring molecules, the backbones can slip and slide more easily. The molecular bonds in the backbones take on a more or less stretched shape and the internal energy ΔU practically does not change, but the entropy ΔS. This gives rise to the term entropy-elastic. The entropy elasticity of the amorphous phase is based on the tendency of the molecules to assume their statistically most probable form, namely the entangled form. Each more elongated form of the molecules forced by an external stress corresponds to a less probable state, and therefore a lower entropy S. This change in entropy causes a restoring force that endeavors to return the macromolecules and thus the macroscopic samples to their original form. However, in order for the individual molecules to move, sufficient space must be available, which is also known as the free volume. This is understood to mean empty spaces of approximately atomic size. The reversible deformation of real elastomers, e.g. rubber, is fundamentally based on this entropy elasticity. Tests on real elastomers have shown that the proportion of entropy elasticity is 85 - 90 %. The rest is the result of the energy elasticity due to intra- and intermolecular interactions, especially when rotations are hindered [57].

When an external force is applied to a polymer at a specific temperature, the internal energy ΔU increases (elastic energy storage through valence distances and angle changes), and the entropy ΔS is reduced (away from the shape of a coil, which corresponds to the state of highest entropy), whereby the proportion of the two deformation mechanisms depends mainly on the polymer itself, time and temperature. Continuing the mechanical loading, the polymers behave viscoelastic. During viscoelastic deformations, normally the conformation of a molecule changes, e.g. due to rotation around single bonds. After stress relief, macromolecules cannot immediately return to the initial energetic and entropic state favored most, but with sufficient time, they can relax and return to the state before load application, in the entangled state with initial bond distances and angles [57].

Considering a solid polymer as a macromolecular solid made up of long molecular chains, in the following thesis called *backbones*, in general a deformation causes a disturbance of the intermolecular and further on intramolecular bonds.

In polymers, viscoelastic and viscous deformation and fracture can occur by breaking either primary covalent or secondary bonds, e.g., van der Waals bonds, through the „pull-out“ of molecules. It is assumed that both processes can occur, but the prevalence of each depends on the type of polymer, temperature, and testing conditions. When the molecules can easily slide past each other and tend to uncoil, the secondary bonds break. The result is a strain softening that can be seen in the engineering stress-strain curve as a drop of stress, because the external mechanical energy is used for the deformation. With increasing tensile test duration and elongation, strain hardening can occur due to the load-induced molecular alignment in the load direction and a new formation of intermolecular interactions. The strain hardening can be detected as an increase in stress in the stress-stain curve before finial failure, since more energy is necessary to continue the viscous deformation process due to the already solved entanglements and in load direction aligned backbones. This behavior can be observed for thermoplastic materials and often comes along with a constriction or necking of the sample, a load-induced reduction in width, and/or thickness.

Molecular fractures through the scission of primary bonds occur if, for any reason, the flow of molecules past each other is restricted due to the nature of the polymer structure. For example, in a semi-crystalline polymer, the crystals can act as anchor points and restrict flow. In cross-linked polymers the chemical cross-link points can make flow more difficult, and in high-molar-mass amorphous polymers physical entanglements will restrict flow especially at high extensions [58]. That is why a widespread assumption in the literature is that highly cross-linked thermosets such as epoxy behave similarly to diamonds, necessitating the breaking of covalent bonds and resulting in a brittle mechanical behavior. Brittle materials are much more sensitive to defects and stress concentrations because of the hindered molecular backbone movements. The nucleation and growth of the voids are strongly related to the acting stress state, which finally controls the experimentally observed strength values and the ability of the polymer to deform plastically. In general, the strength of glassy polymers, such as epoxy resins, is dominated by the presence of defects (e.g., voids, micro-cracks) and the generation of tensile stresses at these defects [59–61]. The presence of defects is strongly correlated with the test volume of the sample under stress, making a mechanical analysis of brittle materials more complicated compared to more ductile thermoplastics or metals. This phenomenon is identified as the size effect (see Chapter 2.2.2).

All materials contain defects at some level. However, it is the manner in which the material responds to these that determines whether there is a size effect. For a brittle material, the stress concentration due to a flaw can not be diminished by molecular movements. As a result, the material is subjected to the entire stress concentration. The local fracture (primary covalent bond breaks) is initiated and propagated, leading to global failure of the material. It is this local material response that leads to the presence of a size effect with regard to the strength [62, 63].

In contrast, in a ductile material like most thermoplastics at room temperature, a defect-induced stress concentration is diminished by localized deformation without breaking intramolecular bonds because molecules can easily slide past each other and thereby release stress concentrations resulting in a viscous deformation.

In the following, the focus is on non-linear, plastic, or viscous and heterogeneous deformation mechanisms in amorphous polymers such as shear bands and crazes. The latter occurs exclusively perpendicular to the load direction. These are local bands of plastically deformed polymer material consisting of polymer fibrils. The fibrils are formed by the stretching of the macromolecules in the load direction. In addition, nano-cavities are formed. These stretched cavities separate the fibrils from each other. The formation of crazes in polymers is not the focus of the following thesis and details can be found elsewhere [64–66].

Shear banding refers to material instability and inhomogeneity occurring during large-strain plastic deformation in solids, where the otherwise uniform flow becomes concentrated in narrow bands on the micrometer scale where large shear strains are localized due to a stress heterogeneity [67, 68]. Shear bands have been widely observed in metals, polymers, the earth's mantle, granular solids, and many other materials (e.g. [68–73]), but as far as the author knows, not for highly cross-linked epoxy resins under tensile load in a significant scope.

During shear yielding in polymers, the molecules slide clearly past each other. They illustrate a type of inelastic response of the material under mechanical loading. The molecules in the shear band zones are oriented by molecular position changes and slipping in semi-crystalline polymers due to the external load [58, 74, 75]. The shear bands are oriented in the direction of maximum shear stress and can occur as a short necking area or a longer strain hardening zone, both of which result in a permanent change of the initial sample geometry.

In Figure 2.1, the macroscopic structure of the shear bands and the orientations on the molecular level in the load direction are shown schematically. The latter results in the strain hardening phenomenon as already mentioned.

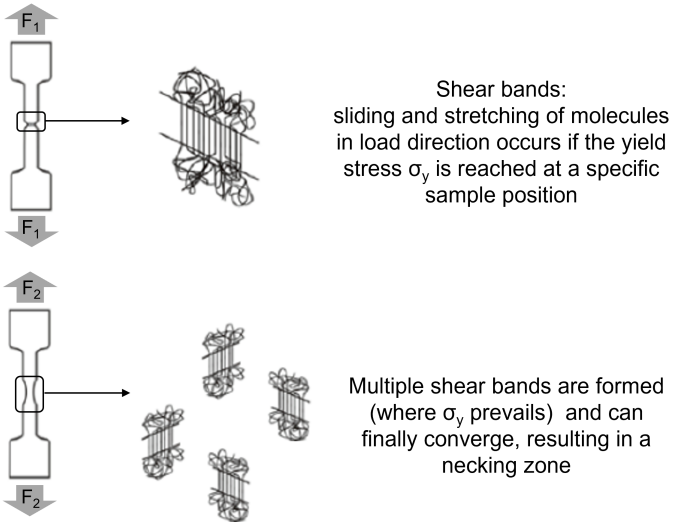

Figure 2.1: Macroscopic structure of shear bands and the orientations of the macromolecules or backbones in load direction are schematically shown. F_1 and F_2 refers to the time t_1 and t_2 during the tensile test, where $t_2 > t_1$. Modified from [76].

However, when a deformed glassy polymer (illustrated schematically in Figure 2.1) is annealed above its glass transition temperature (T_g), it frequently regains its original shape due to a restoring force to a state with higher entropy. The molecules in thermoplastics are securely anchored at entanglement points within the structure and these entanglements can be removed or changed to a certain extent by relaxation processes, e.g. during deformation or thermal annealing. Once the backbones gain sufficient mobility above (T_g), they return to an energetic and entropic favored conformations and the shear bands are recovered [58, 75, 77–79].

The Tresca criteria can be used to determine the required stress tensor for shear yielding to occur. This criterion states that the yield will occur when the maximum shear stress on any plane in the material reaches a critical value and initiates a local stretching and slipping of molecules.

It may be written as follows:

$$\sigma_y = |\sigma_1 - \sigma_3| = 2 \cdot \tau_y \tag{2.1}$$

where σ_1 is the largest principal stress and σ_3 is the smallest principal stress, τ_y is the yield stress of a material under pure shear and σ_y is the uniaxial yield stress.

Another criterion for shear yielding is the von Mises criterion [80]:

$$\sigma_y = (\sigma_1 - \sigma_2)^2 + (\sigma_2 - \sigma_3)^2 + (\sigma_3 - \sigma_1)^2 = 6 \cdot \tau_y^2 \tag{2.2}$$

Shear yielding in glassy polymers is relatively rare and can occur through highly localized shear bands or more widespread shear deformation zones [81]. Localized shear yield can occur in archetypical brittle epoxy resins at stress concentrations or crack tips. These highly localized processes are typically favored by plane-strain conditions, which are commonly found in thick fracture specimens. In contrast, thinner specimens experience more widespread plastic deformation under plane-stress conditions, and most brittle polymers exhibit a transition from brittle to ductile behavior as the specimen thickness decreases. In thin sheets, there is less constraint, which results in extensive shear yielding instead of localized shear yielding or crazing. This described thickness effect occurs because the stress state near the crack tip shifts: in relatively thin plates, it can vary from plane stress at the surface regions to plane strain at the center. This is also the case in thicker plates, but relatively the amount of plane stress is greater for thin samples since the volume-to-surface ratio is increased. This concept is illustrated schematically in Figure 2.2 where the significantly reduced plasticity occurring at the crack tip under plane-strain conditions is apparent, as the effective yield stress is higher in these constrained situations. In a triaxial stress field (plane strain), the stress required for a material to yield is higher than in a biaxial stress field (plane stress) as it occurs at stress-free surfaces ($\sigma_3 = 0$). Consequently, under plane-strain conditions ($\epsilon_3 = 0$), where constraints are higher, there is less plastic deformation at a crack tip. As a result, the limited plasticity at a crack tip, due to the higher effective yield stress under these constrained conditions, leads to a steeper strain gradient immediately ahead of the crack tip, causing the strain to be more concentrated, resulting in less yield flow [58].

A low material thickness and relatively larger resulting plane stress regions are therefore advantageous for viscous shear yielding in polymers.

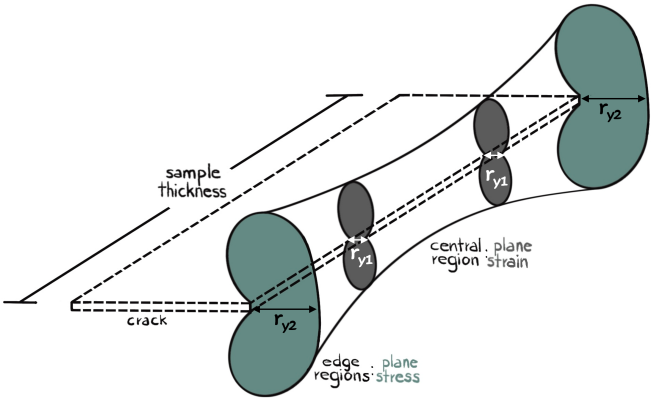

Figure 2.2: Shape of plastic zone at crack tip, according to a von Mises yield criterion (see Equation 2.2), shown schematically as a function of specimen thickness. r_{y1} refers to the plane-strain plastic zone radius and r_{y2} refers to the plane-stress plastic zone radius. Modified from [58, 80].

The energy approach states that viscous flow begins as soon as sufficient chain sections exceed an activation energy. The coordinated movement over energy barriers, of the molecular units comprising a flow unit, results in yield. According to Eyring's flow model [82], the yield stress σ_y is

$$\sigma_y = \frac{2T}{V_{act}} \cdot \left(\frac{\Delta E_{act}}{T} + GC \cdot \ln \frac{\dot{\epsilon}_y}{\dot{\epsilon}_0} \right) \tag{2.3}$$

with the gas constant GC, the energy barrier E_{act} for 1 mol chain segments, the volume of these chain segments V_{act} and the stretching speed or strain rate before $\dot{\epsilon_0}$ and after the yield point $\dot{\epsilon_y}$. Haward and Thackeray [83] interpreted the Eyring activation volume V_{act} as the volume that represents the polymer segments that have to move as a whole in order for flow to take place. Lim et al. [84], have used the definition of activation volume, which states that it can be obtained as the product of the cross-sectional area of the moving molecular segments and the distance covered by it, in its motion during yield. The energy needed for viscous flow E_{act} is provided by mechanical stress and temperature.

According to this theory, deformation in polymers is assumed to be a rate-activated process, where segments must surpass energy barriers as they move between different *vibrational states* (details in the following Chapter 2.3). When stress is applied, these energy barriers change, facilitating molecular transitions in the direction of the applied stress while inhibiting them in the opposite direction [82, 85]. Experiments indicate that for DGBEA epoxy resins, the activation volume V_{act} depending on the composition, ranges from 1 to 4 nm^3 at room temperature. This equates to roughly three chain segments between cross-linking points. The energy barrier can be described as a higher-energy conformational state or as a decrease in entropy [82, 85, 86].

Another approach to describe shear bands is the nucleation approach which focuses on the development of stress-induced deformation zones, known as shear transformation zones (STZs). When a cluster of neighboring STZs grows to a critical size, a micro-shear band forms. During loading, the activation of STZs results in an increase in free volume, which aids in the rearrangement of the polymer chains. The free volume might be stabilized at a constant level where there is a balance between its increase and its decrease due to the rearrangement of the chains [87–89]. The concept of STZ was originally developed by Argon [90] for amorphous metals [91] and was later adapted to amorphous polymers. Therefore, the molecular interpretation of the deformation of the plastic glassy polymer flow can also be addressed by the theoretical models proposed by Argon [92–94]. According to the yielding theory in glassy polymers proposed by Argon and Bessonov, the phenomenon arises from the thermally induced formation of local molecular kinks. They used the concept of wedge disclinations to model this process. Although the mathematical analysis is complex (see [93] for details), the equations derived to explain the relationship between the shear yield stress τ_y and the shear modulus G are relatively simple [95]:

$$\left(\frac{\tau_y}{G}\right)^{\frac{5}{6}} = A - B \cdot \frac{T}{G} \tag{2.4}$$

where T is the absolute temperature and the parameters A and B can be calculated from the Poisson ratio, the Boltzmann constant, the net angle of rotation of the molecular segment between the initial conformation and the activated conformation, the mean molecular radius and the strain rate (see [93, 95] for details).

Bowden and Raha [81, 96, 97] developed another approach based on physical descriptions of plastic flow at the molecular level. The Bowden model proposes that the critical step in the yield process is the stress-induced, thermally activated nucleation of small, disc-shaped sheared regions within the polymer. The strain fields of these sheared areas are considered analogous to those of dislocation loops, with a Burgers vector equal to the shear displacement. Although this theory uses the dislocation concept merely as an analogy, a brief explanation of the dislocation concept in metals is provided before delving into the specifics of the Bowden flow model for amorphous polymers.

The relationship between plastic deformation and microstructure is well recognized in metals [80, 98–100]. In a metallic crystal lattice, atomic defects, such as linear lattice defects known as dislocations, are present. These dislocations move through the crystal lattice under external shear stress, facilitating the plastic deformation of metals by allowing crystal planes to slide over one another without fracturing the entire crystal. Figure 2.3 presents a model of two rows of atoms subjected to shear stress, where the application of shear stress shifts the atomic rows over each other to a new equilibrium position, resulting in macroscopic plastic deformation in the metal. The Burgers vector $\vec{b}$ defines a dislocation, indicating the direction of displacement or slip within the atomic lattice. The force on a dislocation is the product of shear stress and the corresponding Burgers vector $\vec{b}$, acting along the slip plane normal to the dislocation. The movement of a dislocation line along a crystal's slip plane overcomes the interatomic forces across the plane through a series of localized movements dictated by the periodic stress field of the lattice [98]. A ductile phenomenon which can be found in ductile fracture of metals is a neck formation. At a point close to the maximum or the required yield stress in a metallic sample, the yield starts and the described atomic slipping takes place. When an increase in stress due to the cross-sectional sample area exceeds that due to work or strain hardening, an unstable conditions exists and necking begins, a further reduction of the metallic cross-section area occurs. In the following thesis, the therm necking is used for the sake of simplicity as well for thin epoxy film samples to mention a load-induced combined reduction in sample width and thickness even if the mechanisms are not equal to metals and less pronounced.

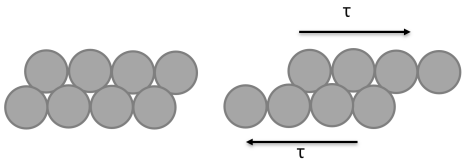

Figure 2.3: Model of an ideal metallic crystal and its reaction to external shear stress τ. Modified from [98].

A schematic illustration of molecular displacements in a sheared region or *dislocation loop* in amorphous polymers is shown in Figure 2.4 according to Bowden [96]. In both amorphous solids and metallic crystals, a *dislocation line* or a slip dislocation marks the boundary between sheared and unsheared regions. Within a crystal, the dislocation core must remain localized because all atoms in this region are in high-energy states. Similarly, in an amorphous structure, the core must remain localized as the dislocation moves. This is because concentrated stress at the core triggers the shearing of adjacent segments and a shear displacement equivalent to a full Burgers vector $\vec{b}$ is required to move these segments to a new equilibrium position. As the sheared polymer region expands, molecular segments at its boundary transition through a high-energy state to achieve a more stable low-energy state. Achieving this requires simultaneous shear displacement of all segments in the sheared region. In real amorphous polymers, the Burgers vector $\vec{b}$ is influenced by several factors, including the width of the molecular chain, the displacement needed to kink a single chain, the length of the chain links, e.g. the cross-linking density, and the spacing of any side groups [96].

A possible explanation consistent with the current model is to suggest that in the random structure of a glassy and amorphous polymer there are many regions where local yield can take place at stresses below those necessary for general yield, e.g. due to small volume differences (vacancies and interstitials) [96].

Strain softening is explained with this approach as follows: The critical step in the process of yielding is the nucleation of small sheared regions since once such regions have grown past their critical dimension they can expand further and further strain will be produced in the sample under a much lower stress [96].

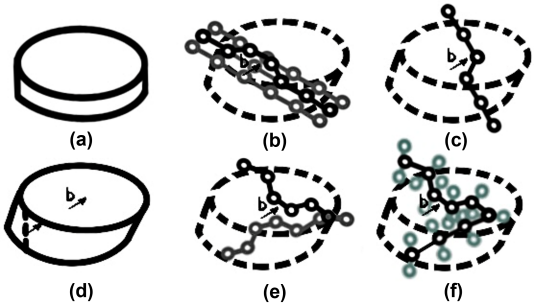

Figure 2.4: Analogous model for amorphous glassy polymers. Modified from [96]. (a) is the initial state and (b) and (c) illustrates molecular backbones and the Burgers vector $\vec{b}$. The latter can be seen in (d) as well together with the shear deformation. (e) shows that more than one backbone chain is involved and (f) illustrates the effect of side chains (mint colored).

With the parameters derived from the Argon theory, the values of $\vec{b}$ for different polymers were determined and it was possible to show that the Burgers vector $\vec{b}$ of epoxy is greater than those of the thermoplastics PS and PMMA. The fully cured epoxy has Burgers vectors that are similar to that of PC [95]. Bowden and Reha [96] noted that polymers with small side groups or small repeat units tended to have small Burgers vectors, while those with large side groups or repeat units tended to have larger values of $\vec{b}$. The results in [95] are consistent with this suggestion. This is an indication that the yield behavior of the epoxy under specific conditions can be compared with that found for amorphous thermoplastics and that the presence of cross-links does not completely prevent viscous shear yielding and the formation of shear bands below T_g.

2.2 Epoxy

Epoxy resins are a subgroup of thermosets with high mechanical and thermal performance. That is why epoxies are often used in high-performance products, e.g. as matrix materials in carbon or glass fiber reinforced polymers (FRP). Further areas of application for epoxy resin include plant engineering, electrical engineering, and adhesives.

2.2.1 Chemical structure

Epoxy parts are made by a reaction of resin with a suitable curing agent which are mixed in a stoichiometric ratio. Both components in turn often result from several chemical components as well. A frequently used raw material for epoxy resin is bisphenol A, which reacts with epichlorohydrin to form bisphenol A diglycidyl ether (DGEBA). DGEBA resin is used mainly in the corresponding thesis. The chemical structure is shown in Figure 3.1.

Cross-linking is carried out with curing agents such as polyfunctional amines, phenols, or acid anhydrides. Amine-based aliphatic curing agents (e.g. ethylenediamine or propylenediamine) have reactive hydrogen atoms in the molecule and can react with DGEBA epoxy resin in a polyaddition. In this process, the reactive groups of the resin and the curing agent react with each other, that is, in a resin system consisting of DGBEA and an amine-based curing agent, the epoxy group and the amine group react and form a dense 3D network. First, epoxy or oxirane rings (cyclic ethers or ethyleneoxide) react with primary amines of the curing agent (initial cross-linking). Secondary amines and the hydroxyl groups can also react with unreacted oxirane rings. The latter, the etherification reaction of the epoxy groups with hydroxyl groups that are formed during the curing process contributes only minimally to the overall conversion of the epoxy groups. Because the reaction between an epoxide and a hydroxyl group requires more activation energy and is thus less thermodynamically favorable than the reaction between an epoxide and an amine [101, 102]. The curing reactions end when most of the oxirane rings have been consumed or to be more precise, the remaining reactions partners are unable to combine due to spatial restrictions of the developing network and lack of molecular mobility. These presented reactions result in linear molecular chains, chain branching, entanglements, and cross-linking between the molecular chains. The average molar mass increases as a result of the ongoing chemical reactions. This results in an increase in viscosity. The viscosity can be reduced by increasing the temperature. At the same time, the energy supplied via the temperature accelerates the chemical reaction, so that the viscosity increases more. An interplay of different factors occurs. With increasing cross-linking, the mobility of the molecular chains is severely restricted, and flow is no longer possible. As a result, the polymer is no longer in a liquid state but in a rubbery state, which is known as the gel point. The subsequent curing is controlled by diffusion.

Due to the increase in the average molar mass, the glass transition temperature T_g increases and becomes higher than the present temperature T ($T < T_g$). This is known as vitrification, and the polymer changes to the glassy state. T_g is characteristic for the degree of cross-linking. Even if it is assumed that the reactive molecules are evenly distributed at the beginning of the reaction due to the mixing of the resin and the curing agent and a perfectly stoichiometric ratio of both reaction partners exists, a 100 % curing with the reaction of all reactive groups is not possible due to the spatial arrangement [5, 57, 103–107]. But technical system which reach the maximum realizable curing degree are treated as fully cured.

Process parameters such as the processing temperature and pot life vary depending on the chemical components and structure. Often additives such as thinners or accelerators are used for the chemical reaction to improve the resulting material properties or optimize the processability.

Furthermore, the physical properties of epoxy-amine thermosets are strongly influenced by the molecular network structure. For a long time, it was assumed that a homogeneous network is formed during the cross-linking reaction. However, for many years, distinct submicrometer nodular morphologies have been observed on scanning electron micrographs of cured epoxy amine systems [108–111]. This observation has also been confirmed by other non-microscopic methods [112, 113]. These findings initiated an active debate about the intrinsic heterogeneity of the cross-linked molecular network [114]. The majority of researchers now agree that epoxy systems indeed exhibit a non-homogeneous molecular network structure. This point of view has been reinforced by recent investigations using small-angle neutron scattering (SANS), wide-angle X-ray scattering (WAXS), and atomic force microscopy (AFM) to examine epoxy systems, which have identified non-homogeneous domains [115–117]. Several researchers have assumed that these nodular structures consist of regions with a relatively higher cross-linking density surrounded by an interstitial phase with a comparatively lower cross-linking density, a perspective that this work also supports [102, 113, 116, 118, 119].

Lower temperatures favor the formation of linear molecular chains, which are cross-linked later. Higher temperatures, on the other hand, favor the formation of cross-linked nodes, which then cross-link with each other.

These processes influence the homogeneity of the polymer, so the latter leads to a heterogeneous structure with strongly and weakly cross-linked areas. Shrinkage occurs during curing, but the free volume increases. This volume not occupied by the polymer chains is higher than in thermodynamic equilibrium. MD simulations show that larger pores grow, in particular, during curing [102, 104, 120–122].

The connectivity within the molecular network between the different domains significantly affects the physical properties of epoxy by creating low-energy pathways that facilitate fracture propagation or dividing the molecular network into two separate sub-networks. In the case of a highly cross-linked, glassy elastic material such as cured epoxy, the fracture surface progresses along a path that breaks the fewest number of strong covalent bonds. Consequently, the advancing crack tip tends to move through areas with a relatively lower covalent bond density (or lower cross-linking density) while maintaining areas with a higher concentration of covalent bonds at the fracture surface. Sahagun et al. [102] showed that with increasing network homogeneity, fracture toughness also increases. The study also demonstrates that the morphology of the fracture surface is directly linked to the structure of the underlying molecular network, particularly in terms of the distribution of cross-linking density within the network. The perceived homogeneity of the molecular network can be enhanced by post-curing the material above its glass transition temperature. This process allows unreacted species to increase molecular connectivity in interstitial regions [102].

2.2.2 Mechanical behavior

Thermosets in general and epoxies in particular are often classified as a brittle materials due to their low fracture toughness and their apparently elastic stress-strain response [62, 123]. Due to the 3D molecular network and the comparatively high cross-linking density, the standard bulk sample at room temperature shows no significant yielding or deformation under tensile load unlike a thermoplastic material. Bulk epoxies usually reach elongation at break values between 5-10 % with a sudden failure resulting from multiple molecular chain scissions as the bond energy is exceeded due to external loading.

Because the molecular chains within the epoxy can not easily move or slip due to the cross-linked structure, the molecules cannot counteract the excess stress with movement or reduce it through molecular rearrangement, different from non cross-linked polymers.

The fracture of cross-linked polymers is closely associated with the breaking of primary covalent carbon backbone bonds as well as the disruption of secondary bonds such as dipole, van der Waals, and hydrogen bonds. Calculating the theoretical strength of amorphous polymers is relatively straightforward [58]. This strength is approximately 10 % of the Young's modulus [124]. For most thermosets, such as epoxy, the theoretical tensile strength usually falls within the range of 200 to 400 MPa. These values represent the theoretical maximum limits for the strength observed experimentally. In comparison to the strength of carbon-carbon (C-C) bonds, the experimentally determined strength of macroscopic samples is significantly lower due to the presence of defects.

Additionally, the mechanical properties of thermosets or epoxies are influenced not only by the density of the network but also by physical entanglements and network heterogeneity. In-depth investigations can be helpful for material development and design of functional parts [125, 126]. That is why Demleitner et al. used a special Nuclear Magnetic Resonance (NMR) technique, the time Domain^{1}H DQ NMR method, to determine the amount of free and dangling chains together with the physical entanglement ratio for a DGEBA epoxy resin (D.E.R. 331) with a polyetheramine curing agent (Jeffamine® D-230). The measurement technique can probe physical entanglements [19-22]. By analyzing the NMR dipolar coupling constant, it could be proven that defects, hence free and dangling chains, have a higher impact on the creep properties than physical entanglement for low loadings. For higher loads, it seems that physical entanglements have an increasingly greater role in creep properties [126]. The percentage of physical entanglement for a DGEBA-polyetheramine system was found to be above 6 %. It is observed that the percentage of physical entanglements increases when the non-stoichiometric ratio increases. A hypothesis to explain this would be that, due to the fact that less three-dimensional cross-links are formed, there would be more free volume between cross-links. This would yield less constrained, more mobile polymer chains, which would easily physically entangle with each other [126].

Only under specific conditions cross-linked epoxies can deform and yield, e.g. under uniaxial compression or in pure shear [58, 127, 128]. Another way to increase the ductility of the archetypical brittle epoxy material is to decrease the test volume.

Size effect

Odom and Adams [62] first observed a significant scale effect, a so-called size effect, in the toughness and tensile strength of epoxy. They tensile tested epoxy dogbone-shaped samples with different test volumes and a crosshead speed of 1.27 mm/min (strain rate: 10 %/min). The particular material selected in this study was Hercules 3501-6. Different sample sizes were tested; the smallest samples investigated had a test volume of approximately 66 mm^3 and showed the highest fracture toughness and tensile strength. The observation of the fracture surface showed that the average flaw size was smaller for smaller specimens. The authors explained this behavior with two different mechanisms. Firstly, the observed strength increases as the sample size decreases. This is expected based on the arguments presented by Griffith [59], and that smaller specimens have a lower probability of having larger flaws. Data on the size of the flaw that caused a failure support this latter contention. Secondly, the observed strength increases due to a transition from plane strain to plane stress for specimens with smaller gauge volume (see Chapter 2.1). So, the existence of a size effect suggests that the measured tensile strengths should not be presented as if the value is intrinsic to the material. Instead, the tensile strength should always be accompanied by the dimensions of the specimen [62]. A comprehensive review of the of size effects with regard to the strength can be found in [129].

Hobbiebrunken et al. [63] could further reduce the epoxy test volume to 0.006 mm^3 by developing a manufacturing process for epoxy fibers (RTM 6 resin) with an average diameter of 36.7 µm and investigating their performance under uniaxial tensile testing with a constant deformation rate of 1 mm/min. The measured strength data of these epoxy resin fibers were close (60 %) to the theoretical strength and before the final failure, the fibers showed necking and plastic deformation. The results also show an increase in the scattering of the tensile strength data with reducing the test volume. This effect arises from the fact that the sensibility of the specimen to existing voids increases when the dimension of the specimen decreases [63].

Misumi et al. [130] manufactured fibers (test volume between 0.05 and 2 mm^3) and bulk samples (test volume 2130 mm^3) from five different epoxy systems ranging from DGEBA to higher cross-linked TGDDM and TGMAP. These fibers were investigated in tensile test with a 1.27 mm/min crosshead speed (strain rate: 10 %/min). The reference DGEBA bulk samples showed the highest failure strain of 5 % due to their lower cross-linking density compared to the other epoxy systems, as can be seen in Figure 2.5 (a). In contrast, epoxy microfibers exhibited ductile behavior with a distinct yield point in all epoxy systems, as shown in Figure 2.5 (b). The failure strains were greater than 20 % for all resin systems, with the highest failure strain being 50 % for DGEBA microfibers (about 10 times higher than the macroscopic sample). Furthermore, when compared to the maximum stress of the macroscopic specimens, the epoxy microfiber specimens exhibited a relatively high yield stress across all the resin systems examined in this study [130].

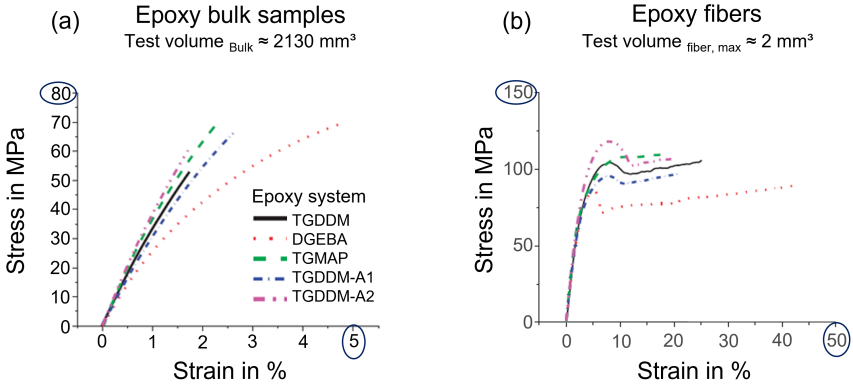

Figure 2.5: Stress–strain curves of tensile tests using macroscopic bulk specimens made from five different epoxy systems (a) and stress–strain curves of tensile tested epoxy micro-fiber made from the same epoxy systems (b). Modified from [130].

Sui et al. [6] used a DGEBA (EP828) epoxy resin with a polyether amine based curing agent (EP304) to manufacture epoxy fibers with diameters between 40 and 160 µm and a test length of 10 mm, as well as standard bulk reference samples. Tensile tests were performed with a crosshead speed of 1 mm/min.

Below a critical diameter, the mechanical behavior changed from defect- controlled to a yield and plastic deformation-controlled strengthening, showing an extreme ductile behavior compared to bulk epoxy. The deformed and necked fibers were subjected to a second tensile test. They showed strain hardening and exhibit higher stiffness and even higher strengths than in the first tensile test. The authors postulated that the ductility, necking behavior, and size effect in highly cross-linked epoxy fibers could be linked, if not attributed, to macromolecular realignment during necking. The latter was validated with wide-angle X-ray scattering (WAXS), which visualized a clear structural orientation in the deformed and constricted fibers. So even highly cross-linked necked epoxy fibers exhibit macromolecular anisotropy, which likely explains the high mechanical characteristics observed (e.g., increase in strength and Young's modulus) [6]. In another study, Sui et al. [5] investigated deformed and necked epoxy fibers with polarized Raman measurements. It was possible to detect a stress-induced alignment of the side groups perpendicular to the load direction in the deformed fibers.

Verschatse et al. [1] made fibers from the standard epoxy system of the samples in this thesis (see Chapter 3.1). The authors performed tensile tests on a large set of epoxy microfiber specimens with diameters ranging from 30 to 400 µm. Extreme ductility was observed for microscale epoxy specimens, while bulk scale epoxy specimens showed typical brittle behavior. The epoxy fibers had a plastic deformation behavior resulting in a significantly increased tensile strength (up to 380 MPa) and strain at break (up to 130 %) compared to their bulk counterpart (68 MPa and 8 %). This might indicate that for epoxy fibers there is somewhat less restriction for the epoxy network to deform and the authors assume that network chains may slip over one another resulting in reorientation of the chains in the internal network [131, 132], somewhat similar to the deformation behavior of thermoplastics [133]. Polarized light microscopy confirmed a rearrangement of the internal epoxy network structure during loading as well [1]. This supports the WAXS and polarized Raman results from Sui et al. [5, 6].

2.3 Vibrational spectroscopy

Vibrational spectroscopic investigations like Infrared (IR) and Raman spectroscopy are based on the interaction of molecules with electromagnetic radiation, which is a type of energy that is transmitted through the space at comparatively enormous velocities. Electromagnetic radiation can be described by means of a classical sinusoidal wave that contains parameters such as wavelengths λ and frequency v. The electric field $\vec{E_{el}}$ can be described as

$$\vec{E}_{el} = \vec{E}_0 \cos(2\pi v_0 t) \tag{2.5}$$

where $\vec{E_0}$ is the amplitude of the oscillation and v is the frequency of the applied electromagnetic radiation and t is the time.

To fully understand spectroscopic methods, it is necessary to present another additional model. Electromagnetic radiation can be seen also, as a stream of discrete wave packets of energy called *photons* [134]. When electromagnetic radiation is incident to a molecular system, an absorption can take place if the energy of the photons is equal to the difference of energies between two vibrational states of the system. The energy of photons is proportional to its frequency and causes the molecules to change their energetic state and vibrate in a characteristic way. If not absorbed, the radiation may be transmitted. Both cases can be observed in IR investigations. A third option is that radiation may be scattered by the molecular system, which can be observed in Raman measurements [135, 136].

According to the different interaction phenomena and different types of energetic radiation, vibrational spectroscopy includes several different techniques to detect and analyze molecular vibrations. The most important spectroscopic methods are Raman and Infrared (IR), mostly mid-Infrared (MIR) and near-IR (NIR), which are used in the following thesis. Both MIR and Raman spectroscopy provide characteristic fundamental vibrations that are employed for the analysis of molecular structures and can be applied to investigate a vast array of sample types. MIR measurements can be performed from a basic identification test to an extensive and comprehensive spectrum analysis, both qualitative and quantitative. Samples can be analyzed in bulk or in microscopic quantities in a wide range of temperatures and physical states [137].

In the most common form of IR spectroscopy, a substance is irradiated with IR radiation of varying frequencies v or wavelengths λ (both related to radiation or photon energy) and the absorption caused by the material is plotted against the wavelength. In Raman spectroscopy, on the other hand, a substance is treated with a laser. Due to the interaction of laser photons and molecules, the frequency v_m of a small fraction of the laser radiation scattered by certain molecules differs from the incident laser beam v_0. The difference in wavelength between the incident laser and scattered material radiation corresponds to wavelengths in the MIR region. In spectroscopic analysis the reciprocal of the wavelength λ, the wavenumber $\tilde{v}$ is usually used instead of the wavelength since the wavenumber $\tilde{v}$ is directly proportional to the photon energy of the radiation and the frequency v. The wavenumber $\tilde{v}$ is given in cm^{-1} which corresponds to $10^4\ \mu\mathrm{m}^{-1}$. For Raman spectra the wavenumber means the difference between the laser wavenumber and the scattering radiation from the material ($\tilde{v}_0$-$\tilde{v}_m$), which is why the term Raman shift (also given in cm^{-1}) is often used instead of wavenumber since the shift in the wavenumber $\tilde{v}$ depends on the chemical structure of the molecules responsible for the scattering [134, 138, 139].

IR and Raman spectroscopy both involve examining the interaction of radiation with molecular vibrations, but they differ in how photon energy from the applied electromagnetic radiation is transferred to the molecule, changing its vibrational state. MIR spectroscopy observes transitions between molecular vibrational energy levels as IR radiation is absorbed. This interaction between light and matter occurs under resonance conditions and involves electric dipole-mediated transitions between vibrational energy levels. In contrast, Raman spectroscopy involves a two-photon inelastic light scattering process. Here, the incoming photon from laser radiation has much more energy than the vibrational quantum energy and transfers part of its energy to the molecular vibration, with the rest being scattered as a photon with reduced frequency. In Raman spectroscopy, the interaction between light and matter takes place under non-resonance conditions and involves the Raman polarizability of the molecule [137].

IR and Raman vibrational bands are characterized by their frequency or wavenumber (energy), intensity (reflecting polar character or polarizability), and band shape (reflecting the environment of the bonds). Because the vibrational energy levels are unique to each molecule, both the IR and Raman spectra provide a *fingerprint* of a specific molecule.

The wavenumbers or frequencies of these molecular vibrations depend on the masses of the atoms, their geometric arrangement, and the strength of their chemical bonds. These spectra offer information on molecular structure, dynamics, and environment [137]. That is why in the following thesis the focus is on the *fingerprint* regions in the recorded Raman and MIR spectra, especially under simultaneous applied mechanical stress.

Raman and mid-IR spectroscopy are complementary methods, and it is often necessary to employ both methods to fully capture the vibrational modes of a molecule. Although some vibrations can be active in both Raman and IR, these two spectroscopic techniques are based on different processes and follow different selection rules. Generally, Raman spectroscopy is most effective for observing symmetric vibrations of non-polar groups, whereas IR spectroscopy excels at detecting asymmetric vibrations of polar groups [137]. This is the reason why both spectroscopic techniques are used in the following thesis.

2.3.1 Fundamental principles

In the following, the basic physical relationships between covalently bonded atoms and their vibrations, which are necessary for the understanding of this work, will be briefly discussed. For the sake of simplicity, the basic physical concepts of diatomic molecules are presented and molecular rotations are not discussed. A comprehensive description of the mathematical and physical relationships of molecular physics and quantum mechanics is not the subject of this work and can be found in the corresponding literature [140–145].

The potential energy term of molecules includes the attraction of the negative electrons by the positive atomic nucleus, Coulomb repulsion between the atomic nuclei, and mutual electron repulsion. Therefore, it depends on the relative distances between the atoms which are related to the orbitals of electrons or clouds (regions where electrons are located with increased probability) [140]. The potential energy of the molecules tends towards a minimum, so that an equilibrium distance R_e, often called the averaged bond distance or lengths, is established between the two covalently bonded atoms in a diatomic molecule. In this case, the potential energy corresponds to the bonding energy E_B. The interaction of molecules with energetic electromagnetic radiation changes the potential energy of certain molecules. By absorbing the energy of electromagnetic photons E_{photon}, the molecule changes from the energetic state E_1 to the state E_2.

The energy of the electromagnetic photon is made up of Planck's quantum of action and the frequency v. Taking into account the law of energy conservation, the following applies.

$$E_{Photon} = h \cdot v = |E_2 - E_1| \tag{2.6}$$

Planck's quantum of action h ensures the quantization of energy, i.e. the energy values do not change continuously, but only discrete energy values exist. For this reason, the excitation of molecules with electromagnetic radiation only results in defined energy transitions, i.e. a molecular change of state occurs only for discrete energy values. According to Equation 2.6, the energy of electromagnetic radiation therefore depends directly on the frequency v. Thus, transitions only occur at certain frequencies v or wavenumbers $\tilde{v} = v/c$ used as an energetic measure [140, 146]. The higher the wavenumber $\tilde{v}$, the higher the energy of the photons E_{photon} of electromagnetic radiation.

Infrared spectroscopy

Depending on the photon energy, IR radiation can be classified as far-(FIR), mid-(MIR), and near-IR (NIR). In this thesis IR is used synonymously with MIR and explicit reference is made to measurements in other wavenumber ranges. Depending on the type of radiation or wavenumber $\tilde{v}$, different changes in molecular state are caused in the material.

When molecules interact with radiation from the mid-Infrared range (MIR, 400 to 4000 cm^{-1}), a change in the potential energy or the bond distance R occurs primarily due to vibrational excitation. The molecular vibration of a non-rotating diatomic molecule generated in this way can be approximated for small displacements R from the equilibrium distance R_e between the two atoms by the harmonic oscillator model. This model is based on classical mechanics, in which the molecular bond is treated as a spring according to Hook. After deflection R from the equilibrium distance R_e, the bound molecules experience a restoring force F which, according to Hooke's law, is as follows:

$$F = -k \cdot (R - R_e) = -k \cdot \Delta R \tag{2.7}$$

The constant k in Equation 2.7 represents the bond force constant of a molecule and is a measure of the bond strength [140, 145]. The harmonic parabolic potential energy curve follows from the restoring force by integration and is shown as a dashed line in Figure 2.6.

The Newtonian law of classical mechanics is used to describe the vibration frequency v or the wavenumber $\tilde{v}$ of the molecular vibration. By using the Newtonian law of classical mechanics, Hook's law, the following equation is valid:

$$\tilde{v} \cdot c = v \sim \frac{1}{2\pi} \cdot \sqrt{\frac{k}{m_r}} \tag{2.8}$$

This equation relates the frequency v and, by using the speed of light c, the wavenumber $\tilde{v}$ to the bond force constant k. The reduced mass $m_r = \frac{m_A m_B}{m_A + m_B}$ of the molecule AB can be calculated from the mass of the atom A (m_A) and the atom B (m_B).

It follows from equation 2.8 that the oscillation or vibration frequency v of the atoms depends not only on the atomic mass but also on the bond force constant. However, with this relationship, it can be explained that only photons from the electromagnetic radiation with a specific energy can be absorbed from the material, changed the energetic state and caused specific molecular vibrations. The vibrating atoms can be treated as harmonic oscillators, the energy values are equidistant, i.e. the vibrational quantum number ϑ exists for the i-th quantized vibrational mode ($\vartheta_i = 0, 1, 2, \cdots$). For harmonic oscillations, the oscillation energy state can be described as follows

$$E_{vib,h} = h \cdot v_i \cdot (\vartheta_i + \frac{1}{2}) \tag{2.9}$$

The actual change in potential energy as a function of the atom displacement from their equilibrium position as a consequence of the absorbing photon energy is shown as a solid line in Figure 2.6. From this curve it can be seen that equation 2.9 is only valid for low values of the vibrational quantum number ϑ_i, since with increasing nuclear distance the real molecular potential E_{vib} does not go toward ∞, but converges towards the bonding energy E_B of the molecule. In practice, E_{vib} must therefore be described for large ϑ_i values by an anharmonic potential function, the so-called Morse potential. If the vibration modes were strictly harmonic, no transitions involving changes in ϑ_i by more than ± 1 would be allowed. Since the energy difference for transitions between the ground state $\vartheta_i = 0$ and the first excited state $\vartheta_i = 1$ of most vibration modes corresponds to the radiation energy in the MIR spectrum (400 to 4000 cm^{-1}), the harmonic potential can be used as an approximation for any mode in which the atoms vibrate with simple harmonic motion (that is, obeying Hooke's law) caused by MIR radiation.

Overtone ($\vartheta_i = 2, 3, \cdots$) and combination bands generally appear only weakly in the MIR spectrum of organic compounds along. The NIR spectra include overtone bands due to higher energetic radiation [146].

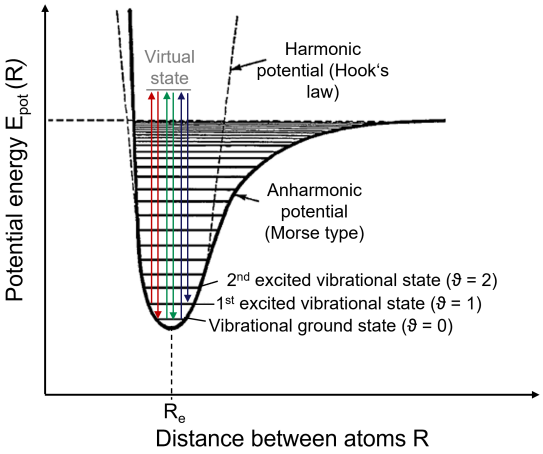

Figure 2.6: Potential energy of a diatomic molecule as a function of the atomic displacement R during a harmonic and anharmonic oscillation. The energy levels symbolizing the scattered radiation from the Raman technique are shown as well (green: Rayleigh scattering; red: anti-Stokes Raman scattering, blue: Stokes Raman scattering) (modified from [138, 146]).

The molecular vibrations arising from the quantized vibrational energy levels (e.g. from the fundamental transitions between $\vartheta_i = 0$ and $\vartheta_i = 1$), can vary from the simple coupled motion of two atoms in a diatomic molecule to the much more complex motion of each atom in a large polyfunctional molecule or an aromatic ring such as benzene. Molecules with N atoms have $3N$ degrees of freedom. Three of these represent translational motion along the x, y, and z axes, which are perpendicular to each other, and another three represent rotational motion around these axes. The remaining $3N - 6$ degrees of freedom determine the number of ways in which atoms in a non-linear molecule can vibrate (i.e., the number of vibration modes). The movement of atoms during vibration is typically represented by the normal coordinate Q.

A molecule can only be excited from the ground state to a higher energy state by IR photons if there is a change in its dipole moment μ during vibration, meaning that

$$\frac{\partial \mu}{\partial Q} \neq 0 \tag{2.10}$$

In molecules with certain symmetrical properties, some vibrational modes might be degenerate (because $\frac{\partial \mu}{\partial Q_i} = 0$), which results in multiple modes sharing the same vibrational frequency, while other modes might not be present at all. Consequently, degeneracy often leads to the observation of fewer fundamental absorption bands than the theoretical maximum of $3N - 6$. Furthermore, since the rotation of a linear molecule about its bond axis does not cause atomic displacement, it lacks one rotational degree of freedom, resulting in an additional vibrational mode for linear molecules. Thus, the number of modes of a linear molecule is $3N - 5$, so that a diatomic molecule ($N = 2$) has a single vibrational mode [146].

Often only a few atoms have large displacements during molecular vibration and the rest of the molecule does only perform minimal vibrations. The frequency of such vibration modes is characteristic for the specific functional group in which the motion is centered and is minimally affected by the nature of the other atoms in the molecule. Thus, observing spectral features in a particular region of the spectrum often suggests the presence of a specific chemical functional group within the molecule. These modes are often known as *fingerprint* peaks and can be found in the wavenumber $\tilde{v}$ range from 800 to 1800 cm^{-1} . For most pure substances, a sample thickness in the (sub)micrometer range is generally sufficient to produce an MIR fingerprint spectrum with the transmission method where the bands are not saturated (with maximum transmittance below 1 %) and are also not so weak that they require ordinate expansion [146]. Thus, the maximum suitable thickness d of a specific material depends on the minimum transmittance $T(\tilde{v})$ which is given by Beer's law as

$$T(\tilde{v}) = exp[-\beta(\tilde{v}) \cdot d] \tag{2.11}$$

where $\beta(\tilde{v})$ is the linear absorption coefficient at $\tilde{v}$.

The absorbance $A(\tilde{v})$ of a sample or mixture of N components where more than one component absorbs at a specific wavenumber $\tilde{v}$, is given by the base 10 logarithm of $T(\tilde{v})$ and the absorptivity $a(\tilde{v})$ $(= \beta(\tilde{v})/ln10)$:

$$A(\tilde{v}) = \sum_{i=1}^{N} [a_i(\tilde{v}) \cdot d \cdot C_i] \tag{2.12}$$

The parameter C_i refers to the concentration of specific molecules or functional groups in the material with a (transmission) thickness d. This form of Beer's law is the fundamental law of quantitative spectroscopy [146]. If it is not possible to create suitable thin samples from the material of interest, either the energy of the Infrared radiation can be increased (NIR) or the examination can be carried out in reflection mode (e.g. Attenuated Total Reflection (ATR)), whereby the material is only examined in the vicinity of the surface.

Raman spectroscopy

Raman scattering is recognized as the process in which light is scattered inelastically as it interacts with molecules [147–149]. Because of the interaction of the electric field of the radiation with an electron cloud of a bond, the *polarizability* of the molecule causes the electric field of the radiation to generate a dipole moment within the molecule. That is why the polarizability in molecules refers to how easily the electron cloud around a molecule's nucleus can be distorted by an external electric field. This distortion results in the molecule developing a temporary dipole, where one molecule side becomes slightly positive and the other side slightly negative. The magnitude of this induced dipole moment μ is determined by

$$\mu = \alpha \cdot \vec{E_{el}} \tag{2.13}$$

where α refers to molecular polarizability, which is a measure of the deformability of the bond or molecule's electron cloud in response to electric fields nearby, e.g., the electric field of incident laser light $\vec{E_{el}}$ [148, 149].

The equation for the oscillation of the electric field $\vec{E_{el}}$ can be found in Equation 2.5. As a result of the electric field oscillating, the molecule's induced dipole moment μ oscillates as well.

In contrast, an oscillating dipole moment can absorb or release energy through transitions between various oscillation energy levels [150]. This energy absorption is the basis for IR spectroscopy, which observes how energy is transferred from incoming light photons to molecules, causing molecules to move to higher energy levels (see previous section). Once excited, these molecules eventually return to lower energy levels, emitting scattered light in the process. This type of energy transition typically remains energetically elastic, meaning that the scattered photons retain the same energy as incident laser light (with a wavenumber $\tilde{\nu}_0$), a phenomenon known as *Rayleigh scattering* which causes the vibration of the electric dipole of the molecule ($\tilde{\nu}_m$) at the same frequency or wavenumber. This results in a peak at a wavenumber $\tilde{\nu}$ ($\tilde{\nu} = \tilde{\nu}_m = \tilde{\nu}_0$) related to the representation of intensity via wavenumber in a Raman spectrum. However, when the energy of the incoming light closely matches the energy difference between different vibrational energy levels of the molecules, the scattering process can cause the excited molecules to switch to a different energy level than where they started. The incoming radiation induces the movement of atomic nuclei as a consequence of electron migrations due to the electric field, and an energy exchange between the molecule and the photon or vice versa takes place during the scattering process. This phenomenon is known as inelastic scattering or *Raman scattering*. However, this process is quite weak, since only about one photon of every 10^6 to 10^8 incident photon is scattered inelastically. The Raman scattering for which the vibrational energy of the molecule moves to a higher energy level than its initial energy level is called *Stokes Raman scattering* and can be observed at a Raman shift or wavenumber $\tilde{\nu} = \tilde{\nu}_0 - \tilde{\nu}_m$. In contrast, scattering with the vibrational energy transition of the molecule from its initial energy level to a lower energy level is called *anti-Stokes Raman scattering* and can be found at a wavenumber $\tilde{\nu} = \tilde{\nu}_0 + \tilde{\nu}_m$ [139, 146, 149, 151]. The different types of scattering are shown in Figure 2.6.

So in order to be Raman active, the polarizability of a molecular bond must vary as a function of distance between nuclei according to the equation

$$\alpha = \alpha_0 + (R - R_e)\frac{\partial \alpha}{\partial \mu} \tag{2.14}$$

where α_0 is the polarizability of the bond at the equilibrium atomic distance R_e (see Figure 2.6) and R is the internuclear separation at any instant [134].

The change in polarizability with the normal coordinate Q of the vibration can also be given by $\frac{\partial \alpha}{\partial Q}$ [146]. For a diatomic molecule, say H_2, the polarizability is anisotropic. Because the electrons that form the bond are more easily displaced by electric fields applied along the bond axis than across the bond direction, for detailed investigations, the polarizability α of a molecule in various directions is defined as a tensor and is conventionally represented by drawing a polarizability ellipsoid [139, 148].

From Equation 2.14 analogously to IR, there is a simplified condition for a vibration mode to be Raman active by

$$\frac{\partial \alpha}{\partial \mu} \neq 0 \tag{2.15}$$

which indicates that the molecular polarizability of the vibration mode should be neither maximum nor minimum when the atoms are at their equilibrium positions [151].

For active IR and Raman vibration modes of a molecule, the Raman shift, which is defined as the difference in wavenumbers between the observed or scattered radiation ($\tilde{v}_m$) and that of the laser source ($\tilde{v}_0$), is identical with the IR peak wavenumber $\tilde{v}$ [134].

Polarized vibrational spectroscopy

When photons move through space, they create an electromagnetic field with two perpendicular components: an electric field (see Equation 2.5) and a magnetic field, both orthogonal to the direction in which the photon travels. These fields share the same frequency. However, only the electric field vector significantly interacts with the vibrational modes of molecules found along the photon's path. As a result, the focus is mainly on the electric field vector. This vector can lie anywhere in a plane that is perpendicular to the direction of travel. When numerous photons move in the same direction, their electric fields tend to be oriented in various planes. This type of radiation is referred to as natural light or unpolarized radiation [146]. Radiation can be polarized, so *polarization* is a property of a radiation beam and describes the plane in which the radiation vibrates [134] and should not be confused with the polarizability of molecules in a material (see Chapter 2.3.1).

When the electric fields of all photons moving in the same direction are restricted to a single plane, the radiation is known as plane-polarized or linearly polarized. This polarized state will remain unchanged unless the radiation encounters certain types of disturbances. Plane-polarized radiation is created using an optical device called a polarizer, specifically a linear polarizer. By placing a polarizer in the radiation path, the radiation is polarized. For samples without specific orientation, like gases, liquids, and isotropic solids, the absorbance of all spectral bands remains constant regardless of the polarizer's alignment. Since a polarizer allows only the electric field component in one plane to pass through, plane-polarized radiation is useful for determining the orientation of functional groups within a sample. When a sample is oriented, it will absorb plane-polarized radiation differently depending on the direction of polarization, which is a phenomenon known as linear dichroism. The highest intensity for each spectral peak is observed when the radiation is aligned with the direction of the maximum change in dipole moment $\frac{\partial \mu}{\partial Q}$ and the direction of vibration for the corresponding vibration mode. If the spectrum of an oriented film is measured with polarized radiation, its dipole moment derivative, $(\frac{\partial \mu}{\partial Q})$ must have a component that is nonzero in the direction of the polarization if that band is to be seen in the Infrared spectrum [146]. Polarized IR technique was applied to different (stretched) polymer films, made from polystyrene [50], highly oriented polypropylene [49], poly(ethylene terephthalate) [146] and polyethylene [152]. Films are often used since for the IR recording in polarized transmission mode, the samples must be sufficient thin to avoid totals absorbance (Beer's law). Scherzer investigated orientation phenomena in highly crosslinked epoxy/amine networks during uniaxial deformation above their glass transition temperature [153].

For polarized Raman spectroscopy, it is again important to distinguish between the term *polarizability* and *polarization* as explained above. Raman scattering involves the interaction between the electric vector of incoming laser light and the differential polarizability $(\frac{\partial \alpha}{\partial Q})$ or as explained above the ellipsoid, directional information are provided. By measuring the angular distribution of Raman scattering intensity using a monochromatic plane polarized laser beam and often additionally an analyzer, the shape and orientation of the differential polarizability $(\frac{\partial \alpha}{\partial Q})$ or ellipsoid within a sample can be accurately determined [151].

When exciting radiation interacts with the molecule, the induced dipole moment will be greatest along the direction of easiest polarizability along a molecular bond or in other words, the interaction of the electric field of the radiation with the electric field, which is caused by the vibration of the dipole moment. The degree of polarization of the spectral lines can easily be estimated by noting how the intensity of each band varies by placing a polarizer in the laser beam [148]. By using a so-called plane-polarized laser radiation, the analysis of polymer backbone orientations independent of the sample thickness can be performed [44–48]. The technique is usually applied to semi-crystalline polymer films, surfaces, and fibers, such as poly (ethylene terephthalate) [51–54], polyethylene [55], and polypropylene [56], as this method is surface sensitive. In the study of Sui et al. [5] polarized Raman analysis was performed on epoxy fibers after they were mechanically stretched. Molecular alignment was indeed found to be induced during plastic deformation of epoxy fibers, and furthermore, a possible explanation for the extremely high mechanical properties of the epoxy fibers was proposed. In another study related to this thesis, polarized Raman measurements were performed on the shear bands and the deformed regions of tensile-loaded epoxy film specimens manufactured in the same manner (see Chapter 3.2) [154]. The aromatic peak at a wavenumber of $1605\,\mathrm{cm}^{-1}$ had shown a polarization mode-dependent intensity that indicates a load-induced molecular backbone orientation, as will be further discussed later in this thesis.

2.3.2 Load-induced IR peak shifts

The mechanical characteristics of a material reflect how individual bonds within the material react to the applied macroscopic stress [8]. Infrared (IR) spectroscopy serves as a useful technique for examining the mechanisms of deformation of materials at the molecular level [9, 10]. Research studies have shown that when a carbon backbone of molecules is mechanically stretched, the vibration wavenumber that corresponds to the peak of certain Infrared signals decreases and a so-called peak shift can be detected. A peak shift towards lower wavenumber values is specified as a red-shift, and an increase in a peak wavenumber is called a blue-shift [11–16].

A theoretical explanation for these so-called peak shifts can give the Badger's rule (Equation 2.16) and the relationship between the peak wavenumber and the bond force constant k of the corresponding vibrational bonds (Equation 2.8). The Badger rule asserts that the bond force constant k_{AB} of a diatomic molecule AB is anti-proportional to the length of the bond R_{AB} between two atoms A and B [155, 156].

$$\boldsymbol{k_{AB}} \sim \frac{1}{\boldsymbol{(R_{AB})^{p}}} \tag{2.16}$$

Values from 2 to 6 can be found in the literature for the exponent p [157]. If an external stress is applied and transferred to the covalent bonds that carry skeletal load within the sample material, the bonds are stretched and R_{AB} increases. Using the Badger rule, this leads to a reduced bond force constant k_{AB}, since the bond is less strong after the stretching process. The consequence is that less photon energy is necessary to cause specific bond vibrations and a red-shift towards lower wavenumbers $\tilde{v}$ of the corresponding peaks can be detected. Different studies show that the red-shift of a peak is proportional to the applied stress [14, 49, 158].

Doblies et al. [159] investigated *in situ* loaded epoxy samples made from the same epoxy system as used in this thesis. The samples had a reduced test volume compared to the standard bulk samples, since samples with thickness 1 mm and geometry A were investigated under tensile load (see Figure 3.6). In that study, it was possible to detect a load-induced red-shift for an overtone of the C-O-C ether vibration at a wavenumber of $2070\,\mathrm{cm}^{-1}$. To analyze the behavior of intermolecular bonds under load, in this study the peak shifts of the C-H bonds in the aromatic ring at $1886\,\mathrm{cm}^{-1}$, which are associated with van der Waals interactions, were also analyzed, even if the C-H bonds are not directly involved in stress transfer. Nevertheless, they contribute to the load-bearing capacity of a polymer because they have a strong dependence on distance, and thus even small changes in distance can enable for a higher load-bearing capacity of the polymer. The authors assumed that it is therefore possible to obtain additional information on the intensity of the intermolecular forces and the free volume by the position of the peak. During mechanical testing, a peak shift towards higher wavenumbers, a so-called blue-shift, was observed for the C-H bond in bending vibration at $1886\,\mathrm{cm}^{-1}$.

The authors explain the peak shift by a decrease in free volume and a higher contribution of intermolecular forces to the load-bearing [159]. In general, a blue-shift can be correlated with a contraction and a resulting increase in bond force constant k (see Equation 2.8) [160, 161]. Different studies have investigated a hydrogen blue-shift experimentally and theoretically [160, 162–165]. Dykstra and co-workers have developed a theory of vibrational frequency shifts in hydrogen bonding based on monomer properties such as electrical moments and polarizabilities [161, 166, 167].

For load-induced changes in Raman spectra, polarizability is crucial (see Equation 2.13). When a bond is stretched, the electrons that form this bond are less strongly held by the nuclei, and hence the bond becomes more easily polarizable, so α increases when the bond is stretched and decreases when it is contracted (Equation 2.13) [136]. Yeh et al. detected a load-induced Raman shift for aromatic high modulus polymer fibers due to mechanical stretching [24]. The peak at $1605\,\mathrm{cm}^{-1}$ for the investigated and loaded fibers shifted towards lower values since α increases as a result of the aromatic bond stretching.

3 Manufacturing methods

3.1 Material

A low viscosity system consisting of EPIKOTE™ Resin MGS RIMR 135, which is based on diglycidyl ether of bisphenol A (DGEBA), combined with a liquid aliphatic diamine curing agent, EPIKURE™ Curing Agent MGS RIMH 137 (Westlake, International: USA/Europe) was used. Both components were mixed in a weight ratio of 100:30 in a mixer (Thinky ARE-250) at 3500 rpm for 5 min. Due to the manufacturing method developed (see 3.2), it was not advisable to degas the resin system, which is why this step was deliberately omitted. However, care was taken to ensure that the epoxy resin system was filled into the mold always immediately after the mixing procedure.

The backbone structure of DGEBA is shown in Figure 3.1. The resin includes also up to 20 % of 1,6-bis(2,3-epoxypropoxy)hexane to reduce the viscosity.

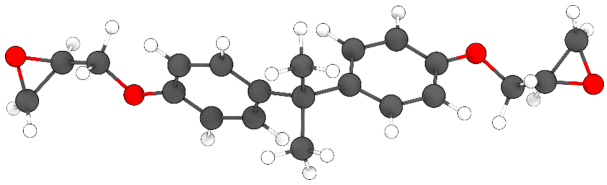

Figure 3.1: Chemical structure of a DGEBA backbone molecules (red = oxygen, white = hydrogen and gray = carbon atoms).

The curing agent constituents are poly(oxypropylene) diamine (weight percentage between 50-75 %) and 3-aminomethyl-3,5,5-trimethylcyloexylamine (weight percentage between 25-50 %). The chemical structures can be seen in Figure 3.2.

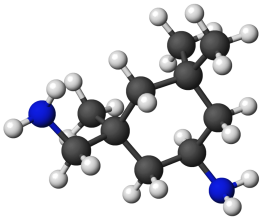

(a) 3-aminomethyl-3,5,5-trimethylcyclohexylamine

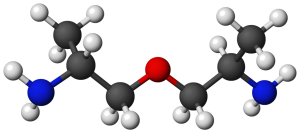

(b) Poly(oxypropylene) diamine

Figure 3.2: Chemical structure of the curing agent compounents (red = oxygen, white = hydrogen, blue = nitrogen and gray = carbon atoms).

In addition, some epoxy films are made of EPALLOY 5000 resin (CVC, Thermoset Specialist, Netherland) and the previously chosen aliphatic diamine curing agent EPIKURE™ MGS RIMH 137 (see Figure 3.2). The epoxy equivalent weight is about 220 g/eq and therefore, both components were mixed in a weight ratio of 100:24 in a mixer (SpeedMixer DAC 150.1 FVZ) at 3500 rpm for 5 min. EPALLOY 5000 is the diepoxide of the cycloapliphatic alcohol, hydrogenated bisphenol A (HBPA-DGE), with a saturated ring structure and low viscosity. Due to hydrogenation, the aromatic rings in BPA are converted into saturated cyclohexane rings as shown in Figure 3.3. For this reason, the system was selected to rule out aromatic structures as the cause of the increased ductility and corresponding molecular mechanisms in epoxy films. In the following, explicit reference is made to samples with this resin system. In all other cases, the results refer to the standard DGEBA resin system mentioned first.

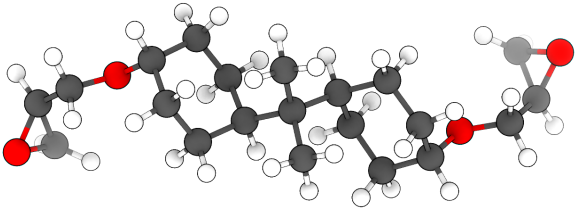

Figure 3.3: Chemical structure of a HBPA-DGE backbone molecules (red = oxygen, white = hydrogen and gray = carbon atoms).

3.2 Epoxy film manufacturing

A sophisticated infusion manufacturing process was developed to produce epoxy films in a suitable reduced thickness (µm range) to avoid total absorbance (Beer's law, see Equation 2.12) and to achieve the low sample thickness for the plasticity tests from the resin systems presented. For this purpose, two glass plates with identical dimensions of 250 mm × 250 mm were placed on top of each other. A „seal" with an identical thickness to the selected or target epoxy film thickness, was placed between these glass plates, thus creating an infusion chamber or cavity. To obtain a resulting film thickness of 15 µm, 30 µm, 50 µm and 100 µm, feeler gauges with defined and appropriate thicknesses depending on the target film thickness and double-sided 5 µm thick transfer adhesive tape (Supplier FFT Group) were used. Therefore, the transfer adhesive tape was placed on both sides of the chosen feeler gauge. Two frames of 80 mm × 40 mm were created side by side with the „seal system". Because the films cannot be removed from the glass plates without causing defects and the use of a release agent is not appropriate (risk of influencing the cross-linking reaction), a suitable carrier film was required. In the course of preliminary tests, a series of substrate materials were extensively analyzed with regard to wetting behavior and release properties. A low density polyethylene (LDPE) film (DM Folien GmbH) met the requirement profile and was therefore positioned between the glass plates and the „seal". The setup is shown in Figure 3.4. In the next step, the entire set-up was placed between two metal plates (including rubber protection) with several screws. They were used to tighten the seal across the entire surface so that the gap was maintained and no resin could escape through the seal. In the last step, the entire construction was placed upright, and the liquid resin system was gradually filled into the gap between the two glass plates using a syringe. After approximately 2 h, the cavity was completely filled with the liquid resin system due to gravitational and capillary forces acting.

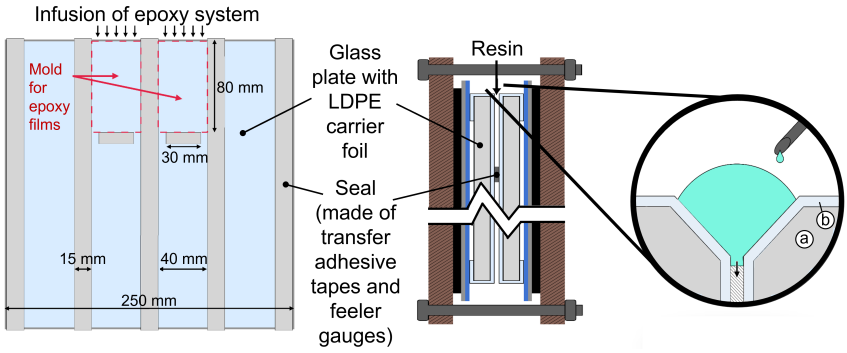

Figure 3.4: Schematic setup of the standard manufacturing process of epoxy films. A glass plate with LDPE carrier foil and the seal frames or cavity for the epoxy films is shown in top view (left). Both glass plates between the metallic frame are shown in side view (right). The glass plates (a) wrapped in LDPE foil (b) are labeled.

As part of this thesis, the glass plate infusion process was optimized in two steps. The aim of the first optimization step was to minimize the time required. The focus here was on the infusion process, as the time required to manually fill the resin into the gap between the bevels of the two glass plates took 2 h. Using a reservoir (see Figure 3.5), which only needs to be filled at the beginning, the time required could be reduced, making the process more economical. The aim of the second optimization step was to increase the production quantity of epoxy resin films. The production quantity was increased from two films measuring 40 mm x 80 mm to four films measuring 40 mm x 220 mm using a vacuum setup. This was possible because the epoxy resin system no longer only flows into the mold gap by gravity and capillary forces, but is also drawn into the mold by an applied vacuum. The optimized setup is shown in Figure 3.5. The quality of the epoxy films with regard to the uniform thickness distribution close to the target thickness were increased as a result of the optimization and the number of unusable film areas (due to voids or deviating thickness) was reduced.

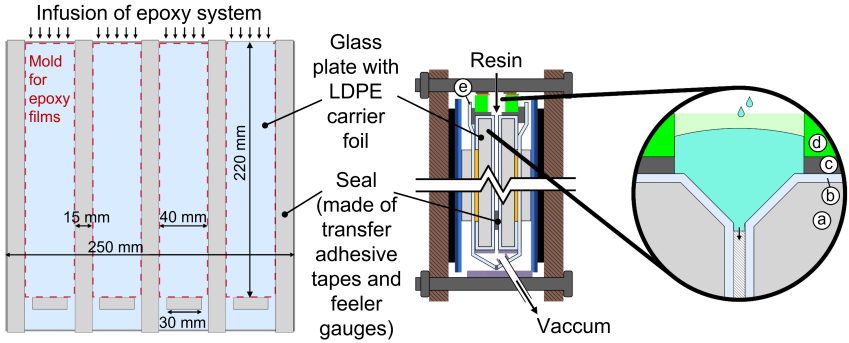

Figure 3.5: Schematic setup of the standard manufacturing process of epoxy films. A glass plate with LDPE carrier foil and the seal frames or cavity for the epoxy films is shown in top view (left). Both glass plates between the metallic frame are shown in side view (right). The optimized manufacturing method includes a reservoir and a vacuum bag. The glass plates (a) wrapped in LDPE foil (b), the vacuum sealing tape (Tacky tape) (c), the reservoir (d) and the vacuum foil (e) are labeled.

In both methods (see Figures 3.4 and 3.5), subsequently, curing took place inside the cavity at room temperature for 72 h. During demolding, care was taken to avoid introducing additional, extensive stresses and strains into the epoxy films. After demolding, the cured DGEBA and HBPA-DGE epoxy films were post-cured at 80 °C for 15 h in a convection oven. For the post-curing process, the films were clamped in a metallic frame to prevent the films from curling. Care was taken to ensure that the films were not stretched during this process. With this manufacturing procedure, films with thicknesses close to the chosen target thickness were available.

3.3 Sample preparation

After the film manufacturing process, the films were investigated with a dial gauge to determine the resulting thickness distribution. Every 5 mm in the width and length directions there was a measurement point in the manufactured epoxy films where the thickness was determined (this was possible by using a corresponding template under the transparent films as orientation for marking the measurement points). All film regions with a thickness deviation greater than 5 µm from the selected target thickness were not used for sample production.

Figure 3.6 shows the dogbone geometries used for the samples. The samples were shaped from defect free film regions (confirmed via microscopy analysis) by punching (geometry A and B) or femto-second laser cutting (geometry C). A dial gauge was used after the shaping process to determine the thicknesses approximately every 1 mm at 7 measurement points within the gauge lengths. Film specimens (geometry A) with a thickness of $14.36 \pm 3.35\,\mu m$, $32.36 \pm 2.01\,\mu m$, $50.94 \pm 1.02\,\mu m$ and $102.11 \pm 3.16\,\mu m$ were obtained. In the following thesis, for reasons of simplicity, the target thickness is generally given for specimens for orientation purposes, as a huge thickness deviation due to the multiple inspection of the thickness can be ruled out.

The geometric dimensions of geometry A and B, which were created by punching, deviate from the established standard DIN EN ISO 527-3, as they were predefined by the Deben microtest stage used, which was located in the IR sample cabinet for *in situ* IR measurements during mechanical loading. Geometry B was even more suitable for this setup, as the necking and shear band formation took place in the specimen center due to the reduced width there. Thus the *in situ* spectroscopic tracking of the deformation processes of the center sample region, in the gauge length, was more feasible with this geometry. By contrast, geometry A was mainly used for the mechanical characterization without IR tracking since the dogbone shape was more similar compared to the bulk sample shape. The type A and type B samples used for the tests on the Deben microtest device have small semicircular recesses for the screws of the clamping units on both sides of the clamping region as can be seen in the Appendix in Figure 1. The recess is included in the punching device at the required position. The gauge volume for a 30 µm thick epoxy film samples was about $1.8\,mm^3$ for geometry A and $0.06\,mm^3$ for geometry B (see Table 4.1).

For samples from the other EPALLOY 5000 epoxy resin system, only geometry A was selected.

To further reduce the test volume, an alternative shaping method to punching was necessary as the limits of accuracy of the punching tools had been reached. A femto-second laser with a wavelength of 343 nm and a beam size (in focus) of approximately 10 µm was used. The cutting speed was set to 175 mm/s which amounts to a pulse energy of 4.6 µJ. With these laser parameters, film samples with geometry C dimensions and a further reduced gauge volume of about $0.06\,mm^3$ were created.

This sample geometry also deviates from the DIN 527-3, as the geometry was predefined by another microtest stage (Alemnis *in situ* indenter) with a smaller load cell.

To ensure that a heat application at the edges during the laser cutting did not affect the mechanical properties due to an increasing cross-linking degree or due to thermal degradation there, both different shaping methods were used for type A sample to ensure a comparability and investigate the impact of shaping method on the mechanical performance.

In the following the samples are called A, B or C regarding the chosen sample geometry.

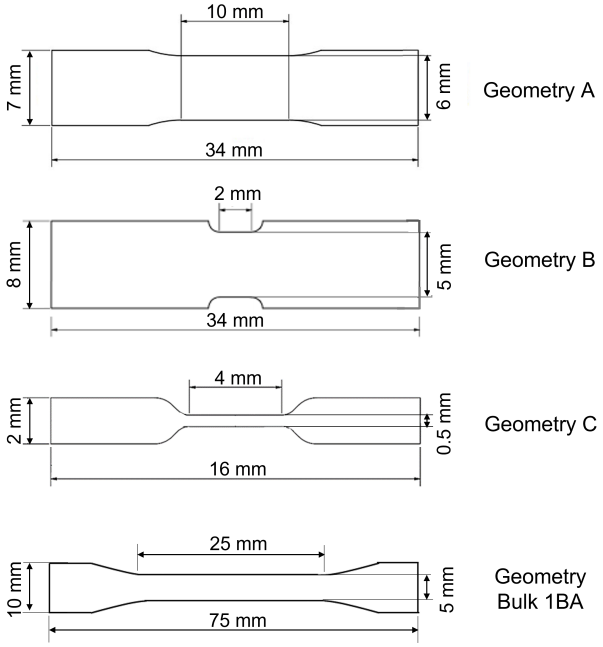

Figure 3.6: Sample shape A and B are created by punching and the sample geometry C is produced by femto-laser cutting the films. The bulk sample geometry 1BA was created by milling.

In addition to epoxy film samples, bulk standard DGEBA epoxy plates with a thickness of 2 mm were produced with a standard Resin Transfer Molding (RTM) process as a reference. The RTM process was followed by a curing and post-curing process identical to that of the film samples (72 h at RT and 15 h at 80 °C). The standard 1BA sample shape according to DIN 527 was created by milling and is shown also in Figure 3.6.

To exclude any possible influence of the sample shape on DSC measurement, bulk sheets were also created from cast rod samples (diameter: 10 mm, height: 50 mm, similar curing profile as films and RTM plates) with a rotation microtome (Thermo Scientific Microm HM 340 E, thickness approximately 70 µm), but only for the DSC measurements.

The epoxy bulk and film samples were conditioned at 23 ± 2 °C and 30 ± 10 % relative humidity for at least 96 h prior to testing.

4 Experimental methods

Figure 4.1 shows the experimental and analytical methods applied to answer the research hypotheses presented (see Chapter 1.2). The details of the specific methods can be found in the corresponding chapters in the following.

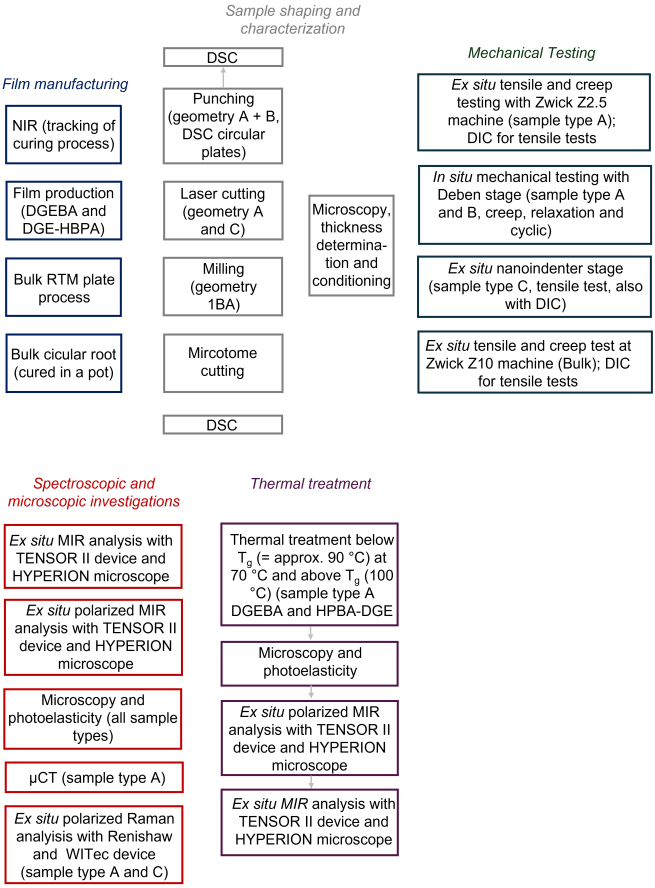

Figure 4.1: Experimental and analytical methods applied in this thesis.

4.1 Epoxy film characterization

To avoid possible defects caused by the demolding or punching process, microscope images were taken after machining using a Keyence VHX-6000 digital microscope and a VK-X3000 laser microscope. The VK-X3000 laser microscope was also used for the inspection of the sample cutting edges, exemplary sample thickness control and inspection of the sample surface roughness.

The possibility of whether components of the LDPE carrier foil diffuse into the epoxy films or whether the curing agent diffuses away into the LDPE carrier foil during manufacturing or cross-linking reaction was to be ruled out. For this purpose, surface-sensitive attenuated total reflectance (ATR) measurements in the MIR range were carried out on the manufactured epoxy films and LDPE carrier foils additionally as a method to analyze the chemical structure of the surface areas. Moreover, the spectra of epoxy films (transmission IR) were compared with spectra of the RTM bulk plate (ATR).

By using a NIR source, spectra in the NIR range from 2500 to 7500 cm^{-1} were recorded to investigate the cross-linking state of the epoxy films produced. A series of publications [168–171] showed that the appearance or disappearance of specific absorption peaks in a NIR spectrum allows quantitative statements to be made about chemical groups and their concentration C_i according to Beer's law (see Equation 2.12). In particular, the epoxide and amino groups disappear during their reaction, and hydroxyl groups were formed simultaneously. Thus, the cross-linking reaction can be tracked via the change in area below the corresponding absorption peaks. The NIR range is advantageous here, as the glass used as the carrier material has no absorption in this spectral range. In addition, there is no overlap of the absorption bands, as would be the case in the MIR range [168]. The method was used as an example to investigate the cross-linking of an epoxy resin film between two microscope slides. The slides were brought to a distance of 50 µm using the same sealing material as during manufacturing. The liquid resin system was filled into the resulting gap or mold. Spectra were recorded over three days during the curing at room temperature (RT). After the post-cruing process (15 h at 80 °C), spectra were recorded again to investigate the effect of post-curing with respect to a cross-linking reaction. The evaluation of the spectra was based on Unger et al. [169]. As the method only makes relative changes visible, it is not possible to say with certainty whether the measured state corresponds to the maximum achievable state in reality.

However, the absence of the absorption peaks of epoxy and amino groups in the NIR spectrum can serve as an indicator of almost complete cross-linking.

For further characterization of the epoxy system and the film specimens, standard and temperature-modulated differential scanning calorimetry (TM-DSC) measurements were performed with a DSC 204 F1 (Netzsch). To analyze and predict the curing behavior of the epoxy system used, DSC measurements with different heat rates (1, 5, 10, 20 and 40 K/min) of liquid stoichiometric resin and curing agent mixtures in crucibles (approximately 25 mg) were necessary. The corresponding heat flow for each heat rate is measured from room temperature to 330 °C. This DSC data can be used in the Netzsch Kinetics Neo 2.0.1.2 software. To do so, the time-temperature transition (TTT) diagram can be determined and the conversion can be predicted for the multiple-step temperature curing process with different models. In this thesis, the isoconventional, differential Friedman model was used to predict the curing behavior. The primary kinetic equation was converted into a logarithmic form and the Friedman plot technique can be utilized. This involves transforming the DSC measurement data into a coordinate system, plotting the degree of conversation γ related to the time t as $ln(d\gamma/dt)$ against 1000/temperature T. Points that share the same degree of conversion γ are then linked linearly and assessed as a linear function. More details about the model can be found elsewhere [172, 173].

For the TM-DSC measurements of post-cured film samples, sheets were punched from the films using a circular punch with a diameter slightly smaller than that of the DSC crucibles. The generated epoxy film sheets were then flat stacked on top of each other in the crucible as can be seen in Figure 4.2. The number of film sheets was selected according to the target weight of 9-11 mg and therefore depended on the thickness chosen for the corresponding films. In total, at least three different epoxy films per thickness were analyzed with TM-DSC. To rule out a difference between films and bulk samples in terms of cross-linking behavior or glass transition temperature (T_g), the T_g of three bulk samples from the 2 mm thick RTM plates were also investigated. To exclude any possible influence of the sample shape on DSC measurement, bulk sheets were also created from the cast rod samples.

Afterwards these sheets were also punched with a circular punch with a diameter slightly smaller than that of the DSC crucibles and they were also positioned on top of each other in the crucible in a way analogous to that of the punched-out film sheets. In summary, there were three different sample configurations for the DSC measurements: 1. films with different thicknesses 2. bulk samples from the RTM plates 3. Microtome cuts from bulk samples.

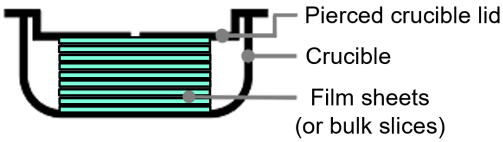

Figure 4.2: Schematic setup of the stacked epoxy film sheets in the DSC crucibles.

For the determination of the glass transition temperature, a linear heating of 2 K/min from 20 °C to 150 °C was applied to all samples. Modulation was carried out with a period of 60 s and an amplitude of 1 K. According to DIN EN ISO 11357-2, the glass transition temperature can be identified by the inflection point method [174]. In this case, the glass transition temperature was determined by using the maximum negative slope via the first derivative of the first heating curve in a specified interval. In addition, the first heating curve was checked with regard to exothermic reactions, in order to obtain information about any unreacted resin or curing agent components that may remain after the post-curing process, since the surface area of the films is very large compared to its volume. This can promote evaporation of the curing agent, which in itself results in a non-stoichiometric ratio of the resin and curing agent and thus incomplete cross-linking.

The thickness distribution of the manufactured epoxy films and samples was determined with a Mitutoyo dial gauge with a precision of ± 0.003 mm. This enables measurements with an accuracy of thousandths of a millimeter. An indentation made by the dial gauge was not optically visible in the post-cured samples under the microscope.

4.2 Mechanical testing

Previous to mechanical testing, the initial or as-produced state of the film samples were analyzed by (polarized) IR (see Chapter 4.4.2, 4.4.3 and 4.5) or Raman (Chapter 4.6). For all mechanical tests, unless otherwise specified, at least five samples in longitudinal direction and five samples in transverse direction in respect to the resin flow direction in the manufacturing process were used.

In the following thesis, stress is defined as engineering or technical stress if not explicitly specified otherwise.

Table 4.1 provides an overview of the geometric sample properties (see Chapter 3.2) and information about the mechanical tests performed.

Table 4.1: Overview of the different mechanical investigated sample types and the corresponding mechanical tests and the respective strain rates. The geometric information and corresponding thicknesses d are listed as well. Only for type A and B samples, different thicknesses were investigated. The crosshead displacement was about 1 mm/min for all samples and all mechanical tests.

Sample type	Gauge volume in mm^2	Gauge length in mm	Strain rate in 10^{-3} s^{-1}	Performed mechanical tests
Film sample A	0.09 (d = 15 µm) 0.18 (d = 30 µm) 0.3 (d = 50 µm) 0.6 (d = 100 µm)	10	1.67	tensile (Z2.5+Gabo)+DIC creep (Deben+Z2.5) cyclic (Deben+MMT)
Film sample B	0.03 (d = 15 µm) 0.06 (d = 30 µm)	2	8.33	creep, relaxation, cyclic (Deben)
Film sample C	0.06 (d = 30 µm)	4	1.25	tensile (Alemnis)+DIC
Bulk 1BA	500 (d = 2000 µm)	25	0.67	tensile, creep (Z10)

4.2.1 Tensile tests

The mechanical properties of the type A film specimens were determined by tensile tests according to DIN EN ISO 527-3. A Zwick Roell Z2.5 tensile machine was used for the tests at room temperature. Preliminary tests showed that the films frequently failed in the clamping jaw area, probably due to a three-dimensional stress state and damage to the specimen caused by contact pressure and the clamping jaw surfaces. Furthermore, it was difficult to clamp and align the thin film specimens between the clamping jaws. For this reason, a suitable paper frame was used to fix the film specimens analogue to ASTM D3379 for single-fiber tensile tests.

The schematic setup is shown in Figure 4.3 and photos from the setup are shown in the Appendix in Figure 2. The samples (glued onto the paper frame) were clamped in the jaws and care was taken to ensure that the specimen was clamped vertically and without applying tension. After clamping, the two paper bars of the paper frame were carefully cut. Samples with geometry A and different thicknesses (15, 30, 50 and 100 µm) were tested at room temperature. The samples were loaded with a constant crosshead speed or displacement rate of 1 mm/min. The change in length or strain was recorded via a video extensometer. The testXpert-II program and a 50 N load cell were used. Only for the film samples with a thickness of 100 µm a 2.5 kN load cell was used. The strain rate of the type A sample tensile tested is $1.67 \cdot 10^{-3}$ s^{-1} to provide the epoxy material with sufficient time to undergo the (molecular) deformation processes.

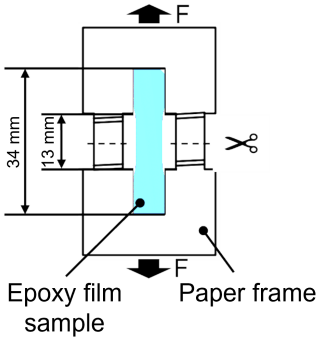

Figure 4.3: Schematic depiction of a film specimen glued onto a paper frame as it was inserted to a Zwick Z2.5 tensile machine in top view.

An Alemnis *in situ* nanoindenter was modified with grippers to perform tensile tests at samples of type C and more precise force determination at room temperature. An Alemnis sample-side load cell (SLC-2.5) was used. This load cell has a load range of 2.5 N and a load resolution of < 15 µN. Therefore, all experiments were limited to less than 2 N and only film samples with a thickness of 30 µm were tested. The displacement was applied using the Z stage of the nanoindenter which is based on the piezoactuation mechanism and has a resolution < 10 nm. The compliance of the nanonindenter is 4.3 nm/mN. All tests were performed in displacement-controlled mode, and compliance is taken into account in the mechanical data evaluation. A displacement rate of 0.3 mm/min was imposed, resulting in a nominal strain rate for the type C samples of $1.25 \cdot 10^{-3}$ s^{-1}.

In total, six samples (three longitudinal and three transverse to the direction of the resin flow in the film manufacturing process) were tested with this set-up.

As a reference, six standard bulk samples of RTM plates (type 1BA test sample with a test length of 25 mm according to DIN EN ISO 527-2) were additionally tensile tested. These tests were performed with a Zwick Z10 tensile machine and a 10 kN load cell with constant displacement rate of 1 mm/min and a resulting strain rate of $0.67 \cdot 10^{-3}$ s^{-1}. The strain was determined via the crosshead displacement. This allows a comparison of bulk and films, i.e. the influence of the test volume on the mechanical behavior. The bulk epoxy sample type 1BA has a test volume of approximately 500 mm^3 and the epoxy type A films with a thickness of 30 µm generated a gauge volume of approximately 1.8 mm^3 (see Figure 3.6). That is a factor of approximately 280 times less than the test volume of standard bulk samples. For the type C samples with a gauge volume of 0.6 mm^2 the the gauge volume is about a factor over 8000 less.

Tensile tests at different temperatures

In addition, film specimens of type A with a thickness of 50 µm were subjected to tensile tests at different temperatures that deviate from room temperature. This was done to analyze the influence of the test temperature on the ductility and molecular processes that could occur during plastic deformation. The test temperatures were set to T = 3, 13, 33, 43 and 53 °C, respectively. Before mechanical testing, the specimens were analyzed by IR (see Chapter 4.4.2). Tensile tests were performed on a Gabo 500 N type dynamic mechanical thermal analysis (DMTA) test machine with a constant displacement rate of 1 mm/min. During the mechanical test, the specimen was placed in a climatic chamber with a defined and controlled test temperature. Here, the specimen was clamped without a paper frame, but with gripping tabs in the clamping area made of crepe tape. Five type A samples (see Figure 3.6) were tested for each temperature. The strain was determined by the displacement of the crosshead. After mechanical testing and failure, some specimens were analyzed a second time by IR (see Chapter 4.4).

4.2.2 Digital Image Correlation

A second set of tensile tests was carried out using a Zwick Roell Z2.5 tensile machine and DIC Aramis analysis software to obtain information on the local strain distribution in type A samples. For this purpose, white and black paint was applied to some film samples in a speckled pattern after the samples were placed and glued onto the paper frame. In order to exclude an influence of the DIC paint on the mechanical properties, films with DIC paint were not taken into account in the determination of the mechanical properties.

In preparation for tensile tests with samples of type C and a modified Alemnis *in situ* nanoindenter, a fine stochastic speckle pattern was applied onto the epoxy film samples using only black spray paint. The spray paint was sprayed against a plastic disk in an approximately 45° angle where the spray paint bounced off and fell onto the samples which were horizontally placed on a paper. To do so, the DIC paint was not applied as a continuous layer; thus, the mechanical response should be similar to the previously tested samples without paint and the influence of the color particles was therefore considered negligible. After the applied color had dried, the pattern was checked for DIC applicability under an optical microscope. The samples with a feasible speckle pattern were tensile tested in combination with DIC immediately after the application and check of the pattern. For this purpose, the loading stage with the clamped sample was positioned under a Leica stereo-optical microscope with a camera and a USB connection for video and image storage. This can be seen in the Appendix in Figure 3. To realize the required black-white contrast, a white piece of paper was positioned behind the prepared and clamped film sample with the black pattern. The magnification was set so that an optical resolution of $\sim 10\,\mu m$ / pixel was achieved in a gauge section. The DIC system was calibrated using a calibration plate (a glass plate with a rectangular grid of dots placed at 0.5 mm from each other). During the mechanical loading of the samples, 15 images per second were recorded. For the DIC analysis and results presented in this study, every 100th image is used, resulting in an effective frame rate of 0.15 images per second, which is considered sufficient for the present purposes (the analysis of every 10th image generated no further insights). The DIC analysis was performed with LaVision DaVis 10.2.1 software with the following correlation parameters: correlation relative to first frame, 2nd-order shape functions, and subset size/step size ranging from 19/6 to 23/7 pixels.

It is noteworthy that due to the evident challenges related to the creation of the speckle patterns in such a small length scale, the resulting pattern speckle size was not homogeneous as highlighted by an example in the Appendix in Figure 4. Most speckles were less than 10 pixels in size, the smallest being in the 3-5 pixel size, which is considered optimal [175]. However, there were also some notably larger speckles (up to 30 pixels). In order to obtain sufficient spatial resolution, the subset and step sizes were selected based on the smaller speckles. This choice led to some loss of data at the vicinity of the larger speckles and in areas with lower local speckle density; this loss was deemed acceptable in the present work. The resulting deformation data were analyzed in terms of strain fields obtained directly from the calculations as well as in terms of data obtained via post-processing, that is, virtual extensometer and strain along a line placed longitudinally on the gauge section. The DIC data were additionally used to check the global strain determined by the displacement of the microtensile test device based on the piezoactuation mechanism.

4.2.3 Creep test

The creep tests were carried out according to EN ISO 899-1 to analyze the impact of time on the microstructural changes under constant mechanical stress which was applied at the beginning of the test with a displacement rate of 1 mm/min. The samples were clamped without a paper frame, but with gripping tabs in the clamping area made of crepe tape. Since in metals, the stress exponent m (slope in $\log(\dot{\epsilon})$-$\log(\sigma)$ curve) is an indicator of the atomic creep mechanism [176], creep tests at different stress levels were performed to checked whether there is a comparable relationship between the creep rate $\dot{\epsilon}$ and the stress level σ (given in percent of determined UTS) for the epoxy resin system used.

Some creep tests were performed with a Deben microtest stage MT200 and a 20 N load cell at stress levels of approximately 56 MPa (80 % of Ultimate Tensile Strength (UTS)), 49 MPa (70 % UTS) and 42 MPa (60 % UTS) for 50 µm, 30 µm and 15 µm thick samples of type A and B. Here, the specimen was clamped without a paper frame, but with gripping tabs in the clamping area made of crepe tape. With an initial clamping distance of 17.5 mm and a maximum distance of 20.5 mm between the inner edges of the clamping jaws, the maximum nominal strain achievable by the Deben stage was approximately 17 %.

In this strain range, all film specimens were necked and formed shear bands, but not all failed. Film samples with a initial strain application rate of $1.67 \cdot 10^{-3}$ s^{-1} (geometry A) and $8.33 \cdot 10^{-3}$ s^{-1} (geometry B) were investigated.

With a servo-controlled Shimadzu MMT-101NV-10 test machine and a 100 N load cell, creep tests were performed for three longitudinal and three perpendicular type A samples with a thickness of 30 µm at a stress level of 45 MPa (65 % UTS) and 42 MPa (60 % UTS) as well.

As a reference, six standard bulk samples of RTM plates (type 1BA specimen according to DIN EN ISO 527-2) were also tested under creep. These tests were performed with a Zwick Z10 tensile machine and a 10 kN load cell with a constant displacement rate of 1 mm/min at the beginning until the specified stress level was reached. The strain was determined via the crosshead displacement. The creep tests were performed at a constant load level of 55 MPa (70 % UTS) for three samples and at 63 MPa (80 % UTS) for three samples.

4.2.4 Relaxation test

The *in situ* relaxation tests were carried out on the Deben microtest stage according to DIN 53441 to investigate molecular relaxation processes due to a constant strain application. The strain value was set to 4 %, which corresponds to a strain value above the yield strain. The displacement rate to reach the defined strain value was 1 mm/min. Epoxy samples of type B with thicknesses around 30 µm were investigated in relaxation tests. The film samples were clamped without a paper frame, but with gripping tabs in the clamping area made of crepe tape for protection.

4.2.5 Cyclic loading

The material behavior under a cyclic load was referred to a fatigue behavior. The increase in strain due to viscoelastic and viscoplastic deformation under *in situ* cyclic or stepwise loading and unloading was analyzed with the Deben microtest device. Type B samples with thicknesses around 30 µm were clamped with gripping tabs in the clamping area made of crepe tape and tested under cyclic loading. The maximum stress was approximately 70 % of UTS of the corresponding tensile tested epoxy films, which corresponds to approximately 50 MPa. The minimum stress was set to approximately 0 MPa.

This resulted in a mean stress of 25 MPa and a pure tensile swelling load with a stress ratio R = 0. The stresses were kept constant for 10 min and applied at a displacement rate of 1 mm/min. A holding time of 10 min for the maximum and minimum stresses was selected in such a way that the epoxy film specimens have time to respond to the applied load. Thus, one load cycle took around 20 min.

In addition, more typically, cyclic tests with type A samples (thickness around 30 µm) were performed at a frequency of 1 Hz. Therefore a MMT-101NV-10 test machine (100 N load cell, 4830 servocontroller) was used. The maximum stress was set to 45 MPa (65 % UTS) and the minimum stress to 4.5 MPa. This results in a stress ratio R = 0.1 and a mean stress of 20.25 MPa. The free test length was defined with 10 mm and three longitudinal and three perpendicular samples were tested.

4.2.6 Photoelasticity and microscopy

All mechanically tested specimens were also examined using photoelasticity to further visualize shear bands and neck zones. Polarized light was used to study the stress distribution in the translucent epoxy films. A Keyence VHX-6000 microscope was used with a VH-Z20 objective and a polarization adapter after mechanical loading and before IR analysis. Therefore, two different polarization filters were used. These two polarizing filters were aligned in 90° to each other. The photoelastic measurement was performed in transmitted light mode, i.e. the translucent and deformed epoxy films were positioned on a glass sample holder between the two polarizing filters which allowed an analysis with cross-polarized light.

4.3 Micro-Computertomography (µ-CT)

To investigate load-induced changes in the sample geometry more in detail, micro-computertomography (µ-CT) measurements with a Zeiss Xradia 520 Versa device were performed together with a 0.4x objective. The voxel size was 5.5 µm, the applied X-ray voltage was 60 kV and the X-ray power was set to 5 W. The number of projections amounted to 3201. Deformed samples of type A with a thickness of 30 µm were investigated after creep tests at 70 % UTS. The initial or as-produced sample state of the same sample type was investigated as a reference.

4.4 Infrared analysis

Except for the NIR network tracking measurements, all IR spectra were recorded in the mid-Infrared (MIR) range of $500\,\mathrm{cm}^{-1}$ to $4800\,\mathrm{cm}^{-1}$ in transmission mode with a resolution of $1\,\mathrm{cm}^{-1}$. Before starting a sample measurement, 40 background spectra were taken from the atmospheric environment in the sample chamber without a specimen and the average background spectrum was used for the determination of the sample spectra. In the following thesis, IR explicitly refers to the recording of MIR spectra in transmission mode. NIR and ATR measurements are mentioned individually.

4.4.1 Spectral data evaluation

Due to comparatively small load-induced changes in the recorded spectra, a thorough evaluation of the spectral IR raw data was required for an identification of changes. Different options exist for the IR data evaluation with respect to load-induced peak shifts. When a load-induced peak shift is comparatively large, such as for oriented isotactic polypropylene samples with a maximum peak shift $\Delta\tilde{\nu}_{max}$ of $2\,\mathrm{cm}^{-1}$ for the skeletal C-C stretching at $975\,\mathrm{cm}^{-1}$ and $1165\,\mathrm{cm}^{-1}$ [16, 177, 178], an analytical evaluation is possible by means of a difference spectrum, as described by Wool [179]. Two spectra (recorded in initial state and deformed/loaded state) are subtracted from each other. In the difference spectrum, peak shifts often appear as characteristic positive and negative peak pairs. A shifted peak is indicated by a positive peak followed by a negative peak (or vice versa), depending on the direction in which the shift occurred. The difference between the wavenumbers of the negative and positive peak maximum represents the peak shift.

Another analysis method, also based on difference spectra, is presented by Šturcová et al. [10]. The difference spectra between the initial and loaded states resemble the negative first derivative of the peak. By numerically integrating this difference spectrum, the original shape of the shifted peak can be recovered and adjusted in size based on the peak shift's magnitude and direction. By dividing the difference integrals by the initial state spectrum, the peak shift is determined. However, with this method, it was found that extremely precise normalization was required and was difficult to achieve. Any inhomogeneity in the sample leads to small variations in the overall signal intensity or absorbance, which severely distort the difference integral spectra.

Similar problems result from dimensional changes controlled by the Poisson ratios of the material [10]. Because epoxy film samples deform and constrict, this method was used comparatively only to a peak-fitting approach as a validation.

The peak shifts of epoxy ($\Delta\tilde{\nu}_{max} = 0.2\,\mathrm{cm}^{-1}$ [159]) are significantly lower than those of thermoplastic materials such as polypropylene due to the 3D cross-linked structure, making an evaluation necessary using methods with numerical calculations. In this study, data processing, peak fitting, and feature extraction were performed mainly with Python to analyze comparatively small spectral changes and peak shifts. This is a procedure by which a peak fitting algorithm optimizes the model to best fit the original data. For the peak fitting approach, different models exists to approximate the statistically distributed excitation of the molecules. That is why the Gaussian profile can be used to describe the spectral shape of solids, which is also true for epoxy samples [10, 159, 180–182].

The Gaussian profile describes the absorbance $A(\tilde{\nu})$ as a function of the wavenumber $\tilde{\nu}$. The shape of a peak centered at a wavenumber $\tilde{\nu}_{Peak}$ can be therefore described as follows [182]:

$$A(\tilde{\nu}) = A_{Peak} \exp\left(-\frac{4\ln(2)(\tilde{\nu} - \tilde{\nu}_{Peak})^2}{FWHM^2}\right) \tag{4.1}$$

where A_{peak} is the maximum absorbance of the peak, $FWHM$ is the *Full Width at Half Maximum* of the peak and $\tilde{\nu}_{Peak}$ is the peak wavenumber of the center of the peak [146].

Lorentzian peak fitting is often applied for gases [180], but solid Infrared spectral peaks can also have a band shape that is very close to a Lorentzian function [146]:

$$A(\tilde{\nu}) = A_{Peak} \frac{FWHM^2}{FWHM^2 + 4(\tilde{\nu} - \tilde{\nu}_{Peak})^2} \tag{4.2}$$

Voigt profiles are often used for liquids, but cannot be expressed analytically, as they result from the convolution of a Lorentzian and Gaussian shape [146]. To model the behavior of peaks in the spectra of liquids, peaks are sometimes expressed also as the sum of Gaussian and Lorentzian shapes (called *Gaussian-Lorentzian*, see Equations 4.1 and 4.2) [182]).

Similarly to the study by Doblies et al. [159], the peak fitting in this study was carried out primarily by approximating a Gaussian model function to stress-sensitive peaks from the IR spectra, and the characteristic features of the distribution were extracted. The Gaussian model is defined as a function of area, mean, and standard deviation and is fitted to the measured data using Python-Library *lmfit* to approximate the measured data. The approximation is based on the method of the smallest squares and minimizes thereby the sum of the error squares between the model function and the measured or interpolated data. To investigate the impact of the selected model function on feature extraction, especially on peak shift $\Delta\tilde{v}$, the Lorentzian and Voigt profiles were also used for peak fitting, but only if these two model functions are explicitly mentioned. In all other cases Gaussian is used.

Figure 4.4 and 4.5 shows the whole procedure performed with Python, from raw data through the optimized model function to feature extraction.

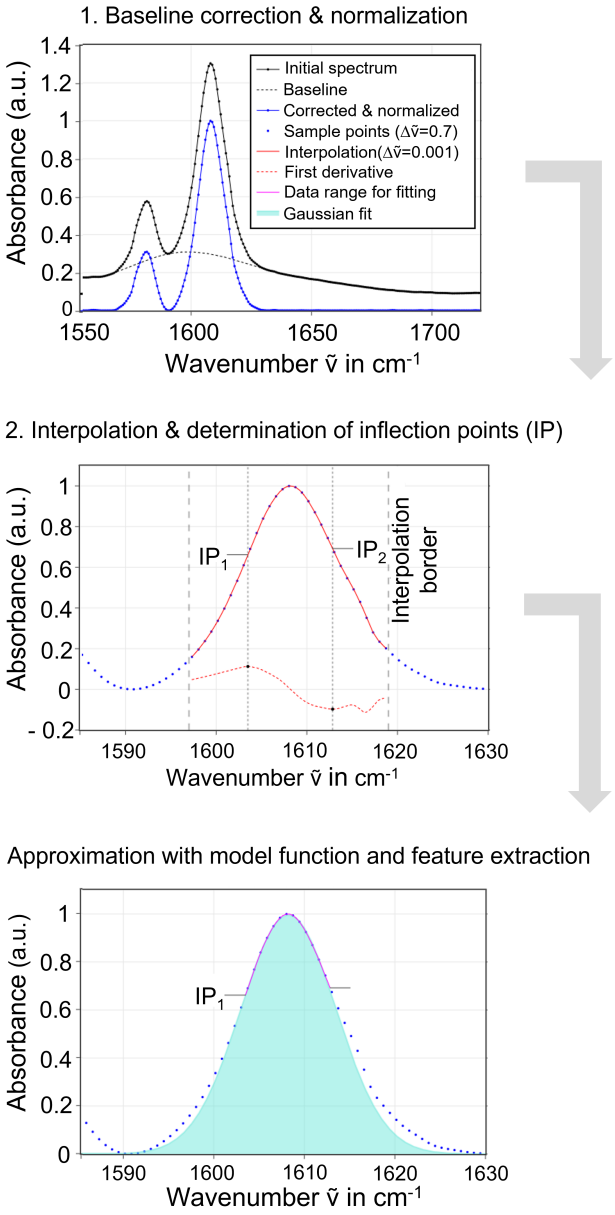

Figure 4.4: Pre-processing of the IR raw data. First a baseline correction and a min-max normalization is applied. In the next step a third-degree spline interpolation is performed and the corresponding inflection points are determined. Finally a model function is approximated, e.g. a Gaussian fit. In the last step the desired features (e.g. peak maximum absorbance A_{Peak} and the corresponding peak wavenumber $\tilde{\nu}_{Peak}$) can be determined from the model function.

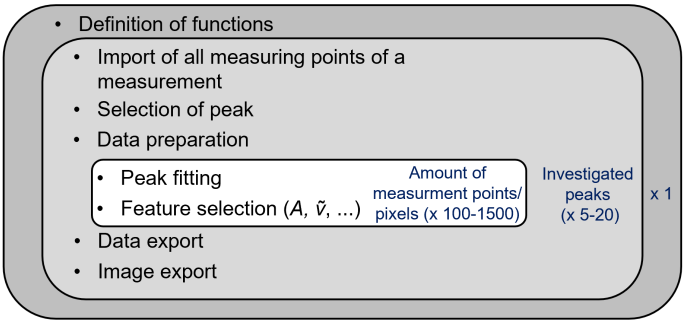

Figure 4.5: Schematic sequence of the Python script used. The number of runs of each loop is shown in dark blue.

First, the raw IR data were read in (.dpt files). All individual measurements were combined into a data frame using a loop. Measurements with an IR microscope (see Chapter 4.4.2) were imported directly into a single file. The analyzed peak was then selected. Individual peaks and their assignment to specific vibrations are listed in Table 5.4. The data were then prepared. Each step was repeated with a loop for each individual measurement (see Figure 4.5). At the beginning of data processing, the transmission values $T(\tilde{v})$ in percent ($\frac{I_0(\tilde{v})}{I(\tilde{v})} \cdot 100\,\%$) were converted into absorbance values $A(\tilde{v})$ with

$$A(\tilde{v}) = 2 - \log_{10}\left(\frac{I_0(\tilde{v})}{I(\tilde{v})}\right) \tag{4.3}$$

This is because the absorbance describes the quantitative relationships, as explained in Beer's law (see Equation 2.12).

In the next step, a baseline correction with the *arpls* - algorithm (correction factor lambda λ set between 1 and 50, adjusted to the selected peak) was performed to reduce background signals as can be seen in Figure 4.4 (1.) and 4.6. The settings *diff_order=2* and *max_iter=50* were used. A correction factor lambda $\lambda = 1$ was used for most of the peaks. Only for the peaks at $1185\,\mathrm{cm}^{-1}$ and $1608\,\mathrm{cm}^{-1}$ $\lambda = 20$ was more suitable. For the peak at $1362\,\mathrm{cm}^{-1}$ the optimized value of 50 was chosen for λ. Afterward, a normalization was performed since a normalization compensates the thickness differences of the films and the changes in the thickness of the film caused by the load-induced deformation (Beer's law, Equation 2.12).

For this purpose, a Min-Max normalization was used, which scales all absorbance values of the recorded IR data to a range between 0 and 1. The absorbance values were scaled using the absorbance of the peak at 1608 cm as maximum absorbances.

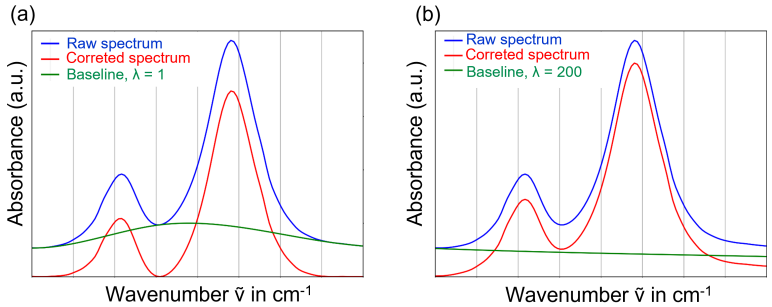

Figure 4.6: The effect of a baseline correction with the correction factor λ is shown (λ=1 (a) and λ=200 (b)).

As a further step of the data processing, an interpolation of the measured IR data was carried out (see Figure 4.4 (2.)). With the selected settings for the IR devices, two measured wavenumbers within a spectrum have a distance of approximately $\Delta\tilde{v} = 0.7\,\mathrm{cm}^{-1}$. A third-degree spline interpolation was used to compact the data and reduce the distance to $0.001\,\mathrm{cm}^{-1}$. This was done using the *scipy.interpolate.InterpolatedUnivariateSpline()*-function. From this, the first derivative was determined with *scipy.interpolate.UnivariateSpline.derivative()* and the inflection points of the peak were determined with *scipy.signal.find_peaks*. The data were then trimmed to the area between the inflection points. This enables reliable and comparable peak fitting even if load-induced peaks shift or change shape occurs.

Afterwards, the model function was approximated between the inflection points. Therefore, a pre-programmed curve was laid through the data points. This was used for experimental data, as noise can be compensated in this way [183]. The model functions were defined manually (see Equations 4.1 and 4.2) and implemented with the *lmfit*-class *.model()*. The Voigt curve was implemented directly with the *lmfit*-class *VoigtModel()*. The starting or input parameters of A_{Peak} and $FWHM$ were set to 10 because these were suitable as starting values.

Using its *Model.fit()*-function, the selected curve was placed through the data points in such a way that the deviation was as small as possible. To do this, the function used a *non-linear least squares* algorithm. In this, the function

$$S = \sum_{\tilde{\nu}_{IP1}}^{\tilde{\nu}_{IP2}} \left(A_{processed}(\tilde{\nu}) - A_{fit}(\tilde{\nu})\right)^2 \tag{4.4}$$

was minimized. $A_{processed}$ is the absorbance A_{Peak} of the processed data (baseline corrected, normalized, and interpolated) and A_{fit} is the absorbance of the approximated or fitted model profile [183]. Figure 4.4 (3.) shows the peak fitting for a representative epoxy film sample.

After the peak-fitting algorithm had optimized the model to best fit the processed data, the Levenberg-Marquard method was used as a metric to determine the goodness of fit [24, 146, 184]. The corresponding parameter χ^2 (chi-squared) can be determined as follows:

$$\chi^2 = \frac{\sum_{\tilde{\nu}_{IP1}}^{\tilde{\nu}_{IP2}} \left(\frac{A_{\text{processed}} - A_{\text{fit}}}{RMS_{\text{noise}}}\right)^2}{n} \tag{4.5}$$

The python *Model.fit()*-function can output the χ^2 values for fitted peaks calculated from this formula. *RMSnoise* is the root-mean-squared noise as estimated from the provided input spectral data. The wavenumber $\tilde{\nu}$ limits were the previous from the interpolated curve calculated inflection points (IP_1, IP_2) as they were defined as boarders for the Gaussian model function (see Figure 4.4). n corresponds to the number of data points between the calculated inflection points IP_1 and IP_2. The resolution of the interpolated data is about $\Delta\tilde{\nu}_{Peak} = 0.001\,\mathrm{cm}^{-1}$ and thus specifies the number of data points n. The smaller the residues, meaning the absorbance difference between the processed and the fitted peak ($A_{processed}(\tilde{\nu}) - A_{fit}(\tilde{\nu})$), the better the fit and the smaller the χ^2 value.

Finally, the desired features, such as the peak maximum or absorbance A_{Peak} and the corresponding peak wavenumber $\tilde{\nu}_{Peak}$ can be output and used for the analysis procedure.

Further investigations with scripts without baseline correction and with truncation to a fixed interval instead of to the region between the inflection points provided comparable results. This ensures that the evaluated results were valid.

The peak width $FWHM$ was examined with the created Python script as well. All dynamics (motion and energy loss) affect the peak width, and there are many theories that explain the influence of different environments on the width. On a simple level, the width is inversely proportional to the effective lifetime τ of the corresponding molecular vibration. A fast loss of vibrational excitation (short τ) leads to broad peaks and a long lifetime (long τ) leads to narrow peaks. Collisions between molecules can also increase the rate of energy loss and broaden the peaks [180]. The width of the peaks in this study is determined at a defined height of 50 % of A_{Peak}. This is shown in Figure 4.7 and 4.8.

Another extracted feature was the asymmetry of the peak. This asymmetry factor ASF is determined at a defined level, often at 50 % of A_{Peak} ($FWHM$):

$$ASF_{Peak} = \frac{\tilde{\upsilon}_{Peak} - \tilde{\upsilon}_{right}}{\tilde{\upsilon}_{left} - \tilde{\upsilon}_{Peak}} \tag{4.6}$$

The extracted peak wavenumbers $\tilde{\upsilon}_{Peak}$ were used for the determination of ASF. An $ASF = 1$ stands for a symmetrical peak, with $ASF > 1$ the right side of the peak is wider (and vice versa). In this work, the asymmetry factor was determined at a level of 20 %, 50 % and 85 % of A_{Peak} as shown in Figure 4.7. $\tilde{\upsilon}_{Peak}$ corresponds to the wavenumber peak maximum (A_{Peak}). The parameter $\tilde{\upsilon}_{left}$ and $\tilde{\upsilon}_{right}$ are the wavenumber values of the peak on the left and right sides at a specific absorbance level (e.g. 50 % = $FWHM$, see Figure 4.7).

To determine the peak area (PA_{Peak}), for each peak a specific wavenumber range was defined, for example, for $\tilde{\upsilon}_{1608}$ from 1591 to 1630 cm^{-1}. For each fitted peak of interest, the two neighboring peak minima in the defined peak wavenumber range were determined by the function *idxmin()*. The corresponding peak wavenumbers of the determined peak minima were used as integration boundaries to calculate the peak area (PA_{Peak}) of the fitted peaks.

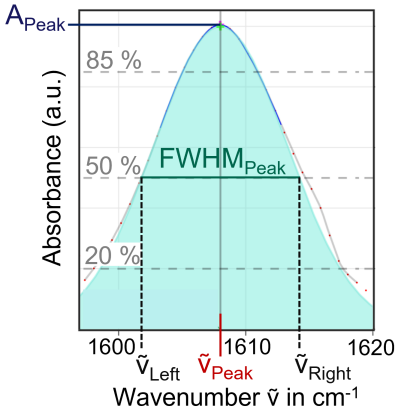

Figure 4.7: The Gaussian fitted peak at a wavenumber of 1608 cm^{-1} is schematically shown together with the $FWHM$, $\tilde{v}_{left}$ and $\tilde{v}_{right}$ positions and the specific absorbance levels for the ASF determination, as well as the peak maximum A_{Peak} and the corresponding wavenumber $\tilde{v}_{Peak}$.

4.4.2 Ex situ Infrared spectroscopy

Samples were analyzed before and after the examination (*ex situ*) and during the examination (*in situ*).

For the *ex situ* IR measurements performed with a Bruker TENSOR II instrument and OPUS 7.5 software, eight sample spectra were recorded per specimen position (circular area with a diameter of 4 mm), and from this an averaged spectrum for the specific sample position was generated by OPUS. This was done for the tensile samples tested at room temperature and at other temperatures.

An HYPERION 2000 Infrared microscope from Bruker was additionally used for the spectroscopic investigation of deformed sample regions due to the significantly higher spatial resolution. A ×15 objective was selected to investigate a sample areas of a square with a size of 165 × 165 μm^2. Thus, the investigated sample area or volume is significantly reduced compared to the IR measurements with a TENSOR II spectrometer (circular sample area with a diameter of 4 mm). To do so, the spectra were recorded from a decreased epoxy volume, and the distinguishing of the deformed and non-deformed sample regions was feasible. The software allows the placement of a grid for multiple measurements.

By placing these square measurements edge to edge, without gap, a detailed overview („IR-mapping“) of the specimen can be obtained. This made it possible to investigate a deformed epoxy film sample and specific shear bands in detail.

4.4.3 In situ Infrared spectroscopy

Using the *in situ* IR method, the spectra were recorded during mechanical creep, relaxation and cyclic tests (see Chapter 4.2) as can be seen schematically in Figure 4.8 and in the Appendix in Figure 5. For *in situ* IR mechanical tests, the Deben tensile microstage presented in the previous chapters 4.2.1 and 4.2.3 was used and inserted into the Tensor II sample chamber. For this purpose, a single spectrum was recorded every 7 seconds at a defined and fixed position of the clamped and loaded sample. This allows the wavenumber of selected bonds or vibrational modes to be tracked over time or during mechanical testing.

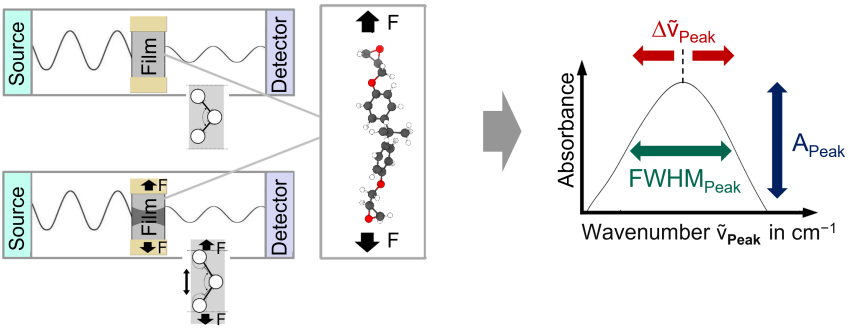

Figure 4.8: Schematic overview of in-situ setup (mechanical testing + IR). The molecular structure changes due to mechanical load introduction and thus causes changes in the IR spectra. Resulting changes could be peak shifts ($\Delta\tilde{v}_{Peak}$), a change in the peak width ($\Delta FWHM_{Peak}$) and a variance in the peak absorbance (ΔA_{Peak}).

4.5 Polarized Infrared spectroscopy

Polarized IR spectroscopy can be performed to detect a change in peak absorbance (ΔA_{Peak}) of oriented molecular bonds or vibration modes depending on an adjusted polarization angle.

If the spectrum of an oriented sample is measured with polarized IR radiation, its dipole moment derivative must have a component that is nonzero in the direction of the polarization so that this peak is visible in the IR spectrum (see Chapter 2.3). For the molecular orientation analysis of the deformed epoxy film samples with shear bands, *ex situ* polarized IR measurements on the loaded and deformed epoxy film samples were performed with the TENSOR II spectrometer and HYPERION microscope. To exclude molecular orientations caused during the manufacturing process (see Chapter 3.2), polarized measurements of as-produced type A samples (longitudinal and transverse to the resin flow direction) were performed. For these polarized spectroscopic measurements, a Bruker polarizer (BaF_2) was connected to the TENSOR II sample holder in front of the aperture. This filter polarizes the IR radiation linearly and the desired angles can be set via the OPUS software.

To investigate comparatively small sample regions, a polarizer can be installed in the beam of the IR microscope as well, and the entire sample can be scanned. The polarization angle was manually set by rotating the polarizer to a specific marker.

For all polarized measurements the investigated polarization angles were set to 0° (parallel to load direction), 45° and 90° (transverse to load direction). Some samples were investigated with even more polarization angles in 22.5° steps (see Figure 5.42).

The raw polarized data processing was done without a normalization, as this would distort the absorbance or peak high at the peak maximum. But, in contrast to the previous description (see Figure 4.4), no normalization was necessary for the *ex situ* polarized IR measurements, as this was done after the sample was mechanically deformed. The spectra from different polarization angles were only compared with each other for the same sample measuring positions. This means that there was no variation in the sample thickness at the individual sample measurement positions. The absorbance A_{Peak} was determined from the processed polarized IR data for different polarization modes.

One way to demonstrate molecular orientation is to determine the molecular orientation factor f for each peak as follows:

$$f_{IR} = 1 - A_{90}/A_0 \tag{4.7}$$

A refers to the absorbance of a corresponding IR peak, where 0° and 90° indicate the polarization mode with regard to the tensile direction. The factor f is not an absolute value of molecular orientation, but can be used for comparative studies [5, 185]. To compare the initial state with the deformed sample state or visually deformed with optically undeformed sample regions, the molecular orientation factor f was calculated with regard to Equation 4.7 for different peaks in this study.

4.6 Polarized Raman spectroscopy

The polarized Raman Spectroscopy measurements were performed with a Renishaw inVia Qontor Raman microscope using a 50x long working distance objective (NA 0.55). The laser wavelength was 532 nm and the spectrometer had a grating with 1200 grooves per millimeter (spectral resolution of 2 cm^{-1}). The resolution was 0.5 µm in 0° and 90° directions. To achieve a strong Raman signal, a depth of 2-3 µm close to the surface was chosen. Before mechanical testing, six type C film samples (without DIC pattern) were analyzed in the as-produced state by the polarized Raman microscope to identify the initial molecular state. Therefore, polarized Raman spectra at four different sample positions in the gauge length were recorded. For every measurement position, measurements in polarization mode or setup 0° (in load direction) and 90° (perpendicular to load direction) (see Figure 5.46) for 120 seconds was performed. After mechanical loading and final failure, Raman spectra were recorded in both different polarization modes in the macroscopically deformed and necked sample regions with shear bands, as well as in the undeformed areas. The raw data were processed by removal of spikes caused by cosmic rays and background noise and by a 4th-order polynomial baseline correction.

Additional measurements were made using a confocal WITec alpha300 RA+ Raman imaging system, equipped with a UHTS 300 spectrometer (grating: 600 groves per mm) and a back-illuminated Andor Newton 970 EMCCD camera together with the WITec Suite SIX 6.1 software package. Measurements were conducted with the same laser wavelength as described above, employing a 50x long working distance objective (Zeiss LD EC Epiplan-Neofluar Dic 50x, NA 0.55), a typical laser intensity of 22 mW (integration time 0.5 s, 50 accumulations). All spectra were subjected to a cosmic ray removal routine and baseline correction (shape mode) implemented in the WITec Project SIX 6.1 software.

After recording, first a comparatively marginal baseline corrected with a correction factor of $\lambda = 5000$ was performed analogously to IR data preprocessing. Because the Raman data are independent from the sample thickness because of the measurement principle, a normalization was not necessary. As a further step of the data processing, an interpolation of the measured Raman data was carried out. A third-degree spline interpolation was used to compact the data and reduce the wavenumber distance to $0.01\,\mathrm{cm}^{-1}$. This was done using the *scipy.interpolate.Interpolated UnivariateSpline()* function in a Python script. The model profile was not approximated, since the peak position or wavenumber $\tilde{v}_{Peak}$ was not the focus of the polarized Raman analysis. Instead, the intensity of the peak I_{Peak} was extracted from the interpolated data. This was done to demonstrate molecular orientations by determining the molecular orientation factor f for each Raman peak analogous to the polarized IR measurement as follows:

$$f_{Raman} = 1 - I_{90}/I_0 \tag{4.8}$$

I refers to the intensity of a corresponding Raman peak, where 0° and 90° indicate the polarization mode with respect to the tensile direction. The factor f was also not an absolute value of molecular orientation, but can also be used for comparative studies with Raman data [5, 185].

4.7 Thermal annealing of deformed epoxy samples

The reversibility of shear band formation that occurs during mechanical loading was investigated by applying heat to the deformed epoxy film specimens. A temperature below and above the glass transition temperature T_g was selected. Mechanically loaded and deformed DGEBA film samples with a glass transition temperature $T_\mathrm{g} \approx 90$°C and shear bands were stored in an oven (Memmert UF 55 PLUS) for 3 h at a defined temperature of T=70°C ($T < T_g$) and T=100°C ($T > T_g$). The deformed HBPA-DGE films with a glass transition temperature $T_\mathrm{g} \approx 70$°C were placed in an oven at T=85°C ($T > T_g$). For this purpose, the samples were positioned freely suspended (only loosely fixed on both clamping ends with crepe tape on a frame) in an oven so that other surfaces had no influence on possible heat-induced molecular relaxation processes.

5 Results and discussion

5.1 Characterization of as-produced epoxy films

In order to exclude influencing factors that could falsify the results as far as possible, the results from these investigations are described in detail in the following Chapter 5.1. The results based on this are presented from the Chapter 5.2 onwards.

Comparing the recorded spectra of epoxy films (transmission IR) and the spectra of the RTM bulk plate (ATR), no significant spectral variations were observed, which would indicate a chemical difference (see Appendix Figure 6). The differences in absorbance are due to the different measurement methods. The intensities in ATR spectra are usually reduced compared to transmission measurements. The reason for this is the manually adjusted contact pressure with the ATR crystal and the smaller test volume due to the bulk surface investigation.

An influence of the LDPE carrier foil on the curing process could not be detected as the surface of the epoxy film that was in contact with the LDPE carrier foil is spectral almost similar to the surface that was in contact with the atmospheric environment (see Appendix Figure 7). Conversely, to ensure that no curing agent diffuses into the LDPE foil, the surface of the LDPE foil was investigated by ATR before and after contact with the manufactured epoxy film sample. Both spectra (before and after epoxy film manufacturing) seem to be almost identical and no difference can be measured. This indicates that no component of the epoxy system diffuses in the LDPE carrier foil (see Appendix Figure 8). As expected, there is no indication of curing agent evaporation or migration in the mold due to the large surface of the films compared to volume, which would results in an incomplete crosslinking as it was found for epoxy microdroplets under atmospheric environments [186].

The cross-linking process between two microscope glass slides observed by means of NIR spectroscopy yielded the following results shown in Figure 5.1. The first recorded NIR spectrum can be seen, which was recorded directly after filling the 50 µm wide gap between the microscope slides. In addition, the peak areas, whose values could be used to track crosslinking, are shown in black. Table 5.1 shows the exact assignment of molecular vibrations and the integration limits according to Unger et al. [169] which are used for the determination of the peak area.

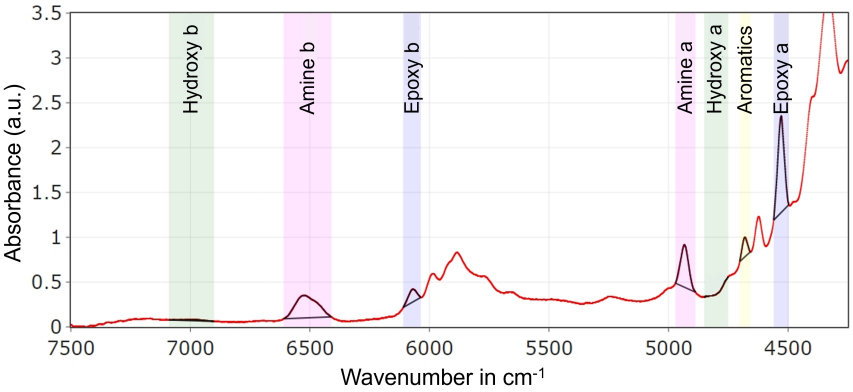

Figure 5.1: NIR spectrum at the beginning of cross-linking reaction. The tracked peak areas during the cross-linking reactions are marked. The „*hydroxy a*“ and „*hydroxy b*“ peak appears in the spectrum after the cross-linking reaction has started.

Table 5.1: NIR absorption bands or peaks and integration boundaries of epoxy according to Unger et al. [169].

Peak	Molecular vibrations	Integration boundaries in cm^{-1}
Epoxy a	CH stretching and CH_2 deformation	4560-4497
Epoxy b	Overtone of CH stretching	6110-6036
Amine a	Primary NH_2 stretching and bending	4971-4887
Amine b	Overtone of primary and secondary NH_2 stretching	6610-6410
Hydroxy a	Combination of OH vibrations	4851-4750
Hydroxy b	Overtone of OH stretching	7090-6901
Aromatics	Aromatic CC and CH stretching	4702-4658

Epoxy and amino groups, in particular, are suitable for observing the cross-linking reaction (see Chapter 2.2.1), as their number is reduced by the reaction and the initial state thus represents a material completely non cross-linked with both resin and curing agent molecules [169] (see Chapter 3.1). To track the amount of non cross-linked epoxy, the vibrational mode of CH stretching and CH_2 deformation at a wavenumber range of 4560 to 4497 cm^{-1} was used, which is known as „*epoxy a*“ in the following. For primary amines, the combination of primary NH_2 stretching and bending vibration from 4971 to 4887 cm^{-1} was used, which is called „*amine a*“. For secondary amines, in addition to the absorption band of *amine a*, the overtone of primary NH_2 and secondary NH stretching from 6610 to 6410 cm^{-1} was also used, which is called „*amine b*“ in the following. Because *amine a* only contains vibrations of primary amines and *amine b* includes additionally secondary amines, *amine a* can be subtracted from *amine b* to obtain a normalized quantitative value for the amount of secondary amine groups present [169]. To analyze the curing process, it is beneficial to determine the normalized change in reactive groups using the absorption band measurements. Therefore, the initial state refers to the reference value of the uncured system that is related to 100 % of each absorption band. Based on the integration parameters, an integrated peak area of zero refers to 0 % of the absorption band. Once normalized, the concentration of functional groups can be determined from the normalized absorption band concentration. The relationships between the functional groups and the absorption bands, as illustrated in Table 5.1, also apply to the normalized absorption bands. The determined curves of the normalized molecule concentration calculated as a function of time are shown in Figure 5.2 (a). The irreversible cross-linking reaction between epoxy groups and primary amines leads to a steady decrease in the corresponding concentration. Secondary amines formed during the reaction reach a maximum concentration before this concentration also decreases as a result of a further reaction with epoxy groups. The post-curing performed leads to a repeated drop in the concentration of epoxy groups and secondary amines. This indicates that the highest possible degree of cross-linking was not achieved without post-curing. This was to be excepted, and it is true for bulk samples as well.

No change in primary amines was observed as a result of post-curing. This indicates that the reactions between primary amines and epoxy groups were already largely complete prior to post-curing.

Because these measurements are based on standardized relative changes in the absorption bands, it cannot be assumed with certainty that the highest possible cross-linking is achieved even in the post-cured state. However, the absence of the epoxy absorption band (Figure 5.2 (b)) in particular is an indication of almost complete cross-linking [169].

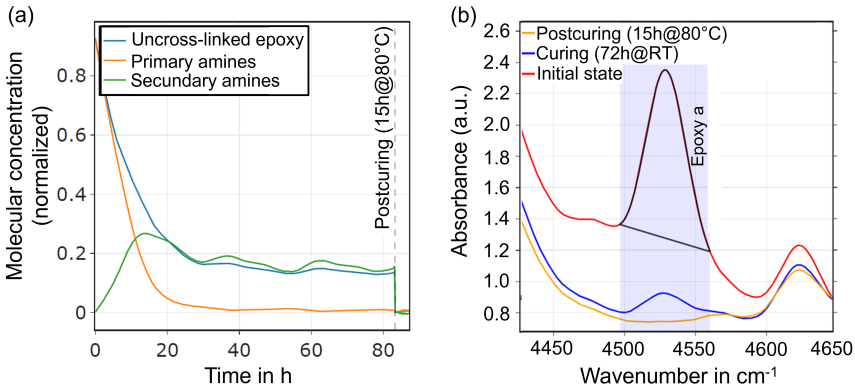

Figure 5.2: Normalized molecular concentration evaluation of non cross-linked epoxy, primary and secondary amines during the curing and post-curing (a) and NIR *epoxy a* peak of the initial state, after curing and after post-curing (b).

None of the investigations had provided evidence that the manufacturing process has an influence on the degree of cross-linking of the films. Furthermore, a time-temperature transition (TTT) diagram for the DGEBA epoxy system, which was determined with the Netzsch Kinetics Neo software and the DSC curing measurements, is shown in the Appendix in Figure 9. It is obvious that complete curing at room temperature is not possible. That is why a post-curing process (15 h at 80 °C) was performed for all samples. By using the Friedman model within the software, a prediction about the conversion with regard to the for epoxy films applied overall (post-)curing temperature profile can be determined. This is shown in the Appendix in Figure 10. Almost complete curing was predicted for the chosen (post-)curing temperature profile.

The other results from the DSC measurements support the modeled results and are presented in the following.

For the DSC measurement, in total, three different post-cured DGEBA epoxy film samples per thickness were investigated. The glass transition temperature T_g determined from the first heating curve (thermal mechanical material history) of the DSC measurement after the post-curing process for all epoxy films is 89.0 ± 3.1 °C. In Table 5.2 the detailed T_g values are listed. The T_g of the samples made of films with a thickness of 15 and 30 µm is slightly higher than for the film samples with a thickness of 50 and 100 µm, but all values are in the data sheet range (T_g around 90 °C). The T_g of three samples taken from RTM plates is 87.1 ± 0.7 °C. The bulk microtome slice or cuts of three different bulk samples have a T_g of 88.0 ± 0.9 °C. The three post-cured HBPA resin film samples with a thickness of 30 µm exhibit a T_g of 73.7 ± 2.4 °C which is in the CVC data sheet range. An exothermic reaction in the first heating cycle is excluded for all DSC samples. All T_g values for DGEBA samples correspond to the Westlake data sheet as well, so that an intended degree of cross-linking can be assumed for bulk samples and for films with different thicknesses. There is no indication of incomplete cross-linking in the DSC results.

Table 5.2: Determined Glass transition temperature T_g values from the first TM-DSC heating cycle for epoxy samples with different thicknesses.

	Film thickness in µm				Bulk	Bulk-Slices
	15	30	50	100		
T_g in °C	91.1 ± 1.0	90.5 ± 0.5	87.4 ± 1.1	87.4 ± 1.5	87.1 ± 0.7	88.0 ± 1.0

Before film samples were shaped by punching or laser, the thickness of the films was analyzed using a dial gauge. Figure 5.3 shows the thickness distribution for a film with the target thickness of 30 µm that was produced using the non-optimized manufacturing method (see Chapter 4.1). It can be seen that not the entire film has the target thickness. In the filling area, in particular, the epoxy film thickness is above the set gap distance between the glass sheets wrapped in LDPE. Due to optimization of the manufacturing process, the reproducibility is increased, larger film regions with suitable thickness close to the target thickness could be manufactured, and the film area can be used for sample production could be further increased. From all manufactured films, only regions that are close to the target thickness were used for sample production.

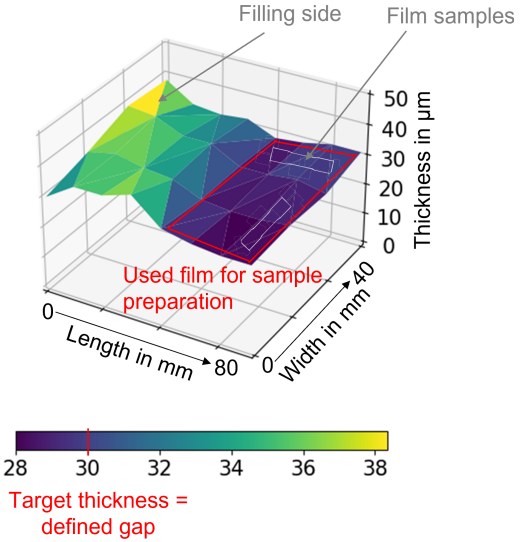

Figure 5.3: Thickness distribution of a manufactured epoxy film with a target thickness of 30 µm.

The sample thicknesses of some punched type A samples were additionally determined using a Keyence VK-X3000 microscope in laser scanning mode. The thickness distribution is visualized in Figure 5.4 for a sample with an average thickness of 28.02 µm in a sample area of approximately 200 x 300 µm^2.

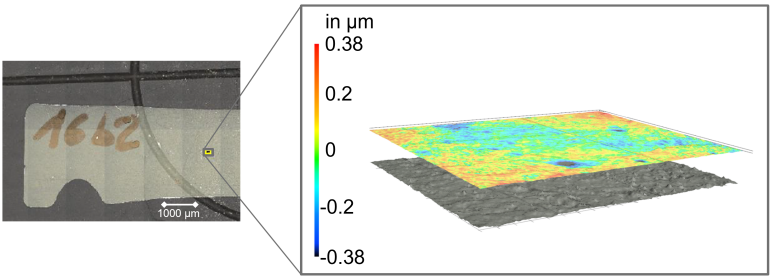

Figure 5.4: Thickness distribution in an area of approximately 200 x 300 µm^2 of a manufactured epoxy film with a target thickness of 30 µm.

After sample shaping and thickness determination, the samples were microscopically examined with respect to defects or voids, surface roughness, and quality of the cutting edges. Samples with detected defects were excluded from further testing and analysis. The cutting edges of a punched and laser-cut film sample are shown in Figure 5.5 and 5.6. It can be seen that the laser-cut specimens have a uniform cut edge with no major defects. In contrast, the cut edge of the punched sample resembles a fracture zone in some areas of the cut edge. This may lead to higher stress concentrations under tensile load in these zones. Nevertheless, most samples in this thesis were shaped by a punching process since the laser device used was not available for the whole duration of the project.

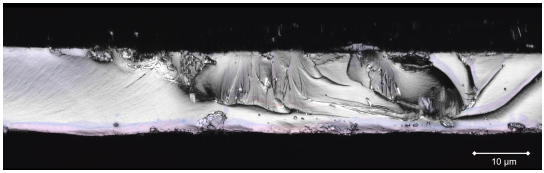

Figure 5.5: Cutting edge of an as-produced sample type A with a thickness of 15 µm create by punching.

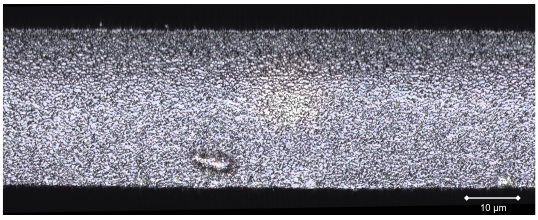

Figure 5.6: Cutting edge of an as-produced sample type C with a thickness of 30 µm create by laser.

The surface roughness determination with a Keyence VK-X3000 microscope in laser scanning mode is depictured in Figure 5.7 for a 1.5 mm long line measurement of a longitudinal type A sample in the width direction. The extrusion lines of the LDPE carrier foil are visible. The value of R_a is about 0.06 µm with a standard deviation of 0.005 µm and R_z amounts to 0.434 µm and a standard deviation of 0.072 µm in the corresponding sample region across the extrusion lines pressed from the LDPE carrier foil. It can be seen that the depth of the pressed main extrusion lines is negligible with regard to the overall roughness due to the surface of the LDPE carrier foil.

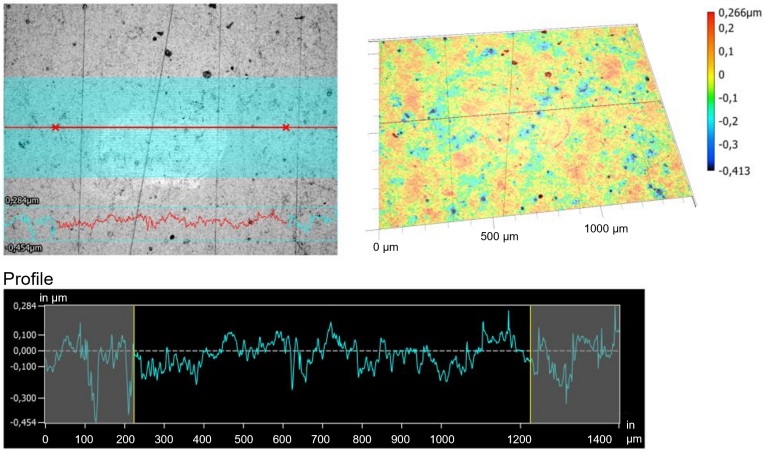

Figure 5.7: Roughness determination across a 1.5 mm long line through extrusion lines pressed from the LDPE carrier foil of a manufactured longitudinal type A film sample with a target thickness of 30 µm. The line is positioned in the width direction of the punched sample.

To exclude molecular orientation or anisotropy due to the epoxy film manufacturing process (see Figure 3.4 and 3.5), polarized IR measurements with a Bruker Tensor II and a polarizer made out of BaF_2 were performed. The absorbance has the same intensity for all polarization directions, so no significant molecular anisotropy as a consequence of the resin flow direction is detectable as can be seen in the Appendix in Figure 11.

5.2 Mechanical testing

The results of the mechanical tests are mainly descriptive presented in the following chapter. The discussion about the molecular processes and mechanisms which lead to the ductile deformation behavior are discussed more in detail in Chapter 5.3 and 5.4 together with the spectroscopic results.

5.2.1 Tensile tests

At least ten film specimens of type A were subjected to tensile tests at room temperature for each sample thickness. Five samples each were examined parallel and perpendicular to the epoxy flow direction during the manufacturing process according to DIN EN 527-3. The elongation at break and tensile strength is slightly higher for the specimens that are punched out in the epoxy flow direction. The cause of the slightly different mechanical properties of both types of film specimens may be due to the extrusion grooves of the LDPE carrier foils, which are to some extent transferred to the epoxy films in the flow direction due to the applied pressure of the screws and the flow behavior during the manufacturing process (see Figure 3.4). This was also verified by an investigation of as-produced epoxy film samples with a digital microscope (see Figure 5.7). A molecular orientation in the as-produced samples could be ruled out as the cause.

Figure 5.8 shows the mechanical properties for type A samples as a box plot with different thicknesses. The detailed mechanical property values are listed in the Appendix in Table 1 and can be found also in [187]. The Young's modulus of type A film sample tested with a thickness of 30 µm in the epoxy flow direction is 3043 ± 170 MPa, the tensile strength UTS can be reported as 69.8 ± 1 MPa and the elongation at break is 7.5 ± 2.9 %. This corresponds to the mechanical results of samples of other thicknesses (see Figure 5.8 and Appendix Table 1). All these values are within the range of the Hexion data sheet (UTS = 60-75 MPa, E = 2700-3200 MPa, ϵ = 5-12 %). The results of the mechanical tests also show that there is no measurable anisotropy in the specimens due to the manufacturing process, since the respective mechanical properties along and across the epoxy flow direction do not differ significantly from each other. Even films with a greatly reduced thickness behave isotropically. This can be seen in the box plot in Figure 5.8) as well. This is in line with the microscope analysis that shows that the extrusion lines pressed from the LDPE carrier foil on the epoxy films during the manufacturing process are of relatively low depth (see Figure 5.7). The defects on the cutting edges, especially of the punched film samples, and the defects that may occur due to the difficult handling of the sensitive films may cause higher stress concentrations and masking or reducing the impact of the extrusion lines. Therefore, and for the sake of simplicity, in the following longitudinal and transverse samples are mostly not distinguished.

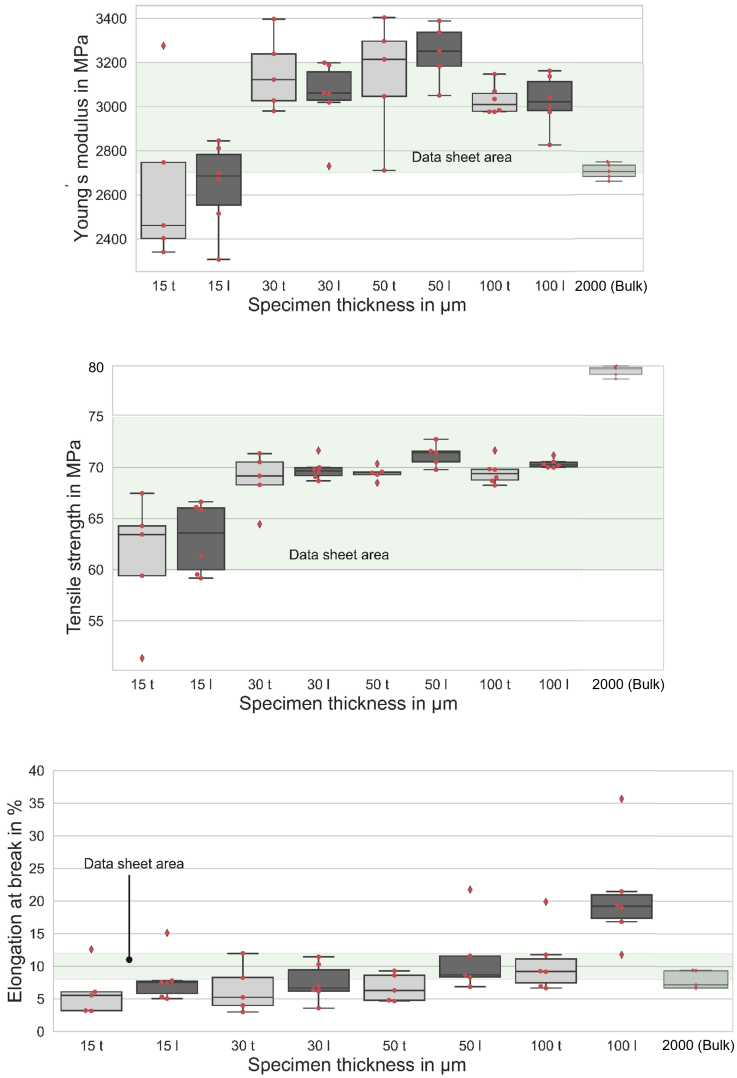

Figure 5.8: The mechanical properties as a box plot of type A epoxy film samples with different thicknesses and bulk samples as a reference are shown. At least five film samples per flow direction of the liquid epoxy system in the manufacturing process and per thickness d were tensile tested with the Zwick Z2.5 and a displacement rate of 1 mm/min at room temperature. „l“ represents „longitudinal“ and refers to samples that were punched parallel to the epoxy resin flow direction. „t“ denotes „transversal“ and refers to all samples that were punched perpendicular to the flow direction. The bulk samples were tensile tested with the Zwick Z10 and the same displacement rate.

For each thickness a representative stress-strain curve in epoxy flow direction is shown in Figure 5.9. In addition, a representative curve of a standard RTM bulk specimen is included as reference. It should be noted that the strain rate of the bulk samples is lower due to the greater gauge length in comparison to all different film samples (see Table 4.1).

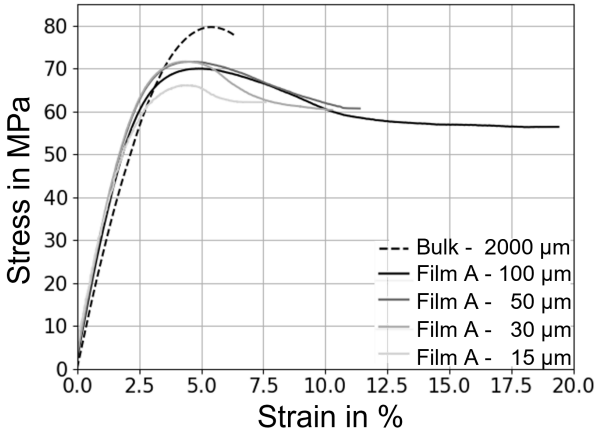

Figure 5.9: Stress-strain curves of film samples of type A and a thickness of 15, 30, 50 and 100 µm. A type 1BA bulk reference with a thickness of 2000 µm is shown as well. All samples loaded with a crosshead speed of 1 mm/min at room temperature.

When comparing the curves and the mechanical properties (see Appendix Table 1), it is noticeable that the bulk specimens tend to have lower elongation at break values than that of the film specimens, but the bulk samples achieve higher strengths despite the lower strain rate. The slightly reduced strength of the films samples may be due to the manufacturing process and the challenging handling and clamping of thin film samples. The punched edges exhibit increased roughness, which under load leads to stress concentrations and earlier failure at lower stresses. This effect is more severe for thinner films. This has also been previously described by other researchers [6, 130] and is due to the fact that at these small scales, any defects in the samples will have a greater influence on the mechanical properties, for example, premature failure) than in specimens with bulk dimensions (see Chapter 2.2.2).

This is probably the reason why the size effect in terms of ductility is not as pronounced with a further reduction in thickness below 100 µm as in the comparison of bulk and films with a thickness of 100 µm.

It is noticeable that the bulk and film curves differ significantly, since the film curves indicate a necking behavior and a steady-state viscous flow, which leads to a drop in the engineering stress. This was also obtained for microscale epoxy fibers, for example, in the study by Verschatse et al. [1], but not to a significant extent for bulk samples (see Chapter 2.2.2). The larger amount of plane stress regions in the tensile-loaded films due to the great surface-to-volume ratio, might be a favorable precondition for an increased ductility (see Chapter 2.1), but it cannot explain the molecular mechanism and the significant increased ductility.

To discuss the impact of the shaping method (punching and laser cutting, see Chapter 3.1) on the mechanical behavior, representative stress strain curves of type A samples with a thickness of 30 µm which were created by laser cutting or punching are shown in Figure 5.10. The Young's modulus and tensile strength do not differ significantly, but the elongation at break for the laser cut type A samples is significantly higher for all samples. Due to the more smooth cutting edges as a result of a laser application instead of a punching tool, there are fewer large defects and less high stress concentrations (see Figure 5.6). The high stress at specific sample positions causes an earlier failure without significant deformation after reaching the yield point. This is in line with other studies, for example, Doblies et al. [159] were also able to achieve a significantly higher strain at break (18 % instead of 10 %) by polishing 0.5 mm thick samples (geometry A, same resin system) and thus reduced the number of edge defects and stress concentrations.

A representative stress-strain curve of a punched type A HBPA-DGE sample with a thickness of 30 µm is also pictured in Figure 5.10. Mechanical performance is significantly reduced compared to that of the punched DGEBA samples (including Young's modulus, UTS, and elongation at break) which can be explained by the different chemical structure (see Figure 3.3) since no stiff aromatic rings are included in the backbones. Argon and Bessonov [78] investigated the impact of incorporating long rigid segments such as aromatic rings or phenylene groups into the molecular structure of aromatic polyimides.

They proposed that this modification would increase the distance between the inherent hinges within the polymer molecules. Their findings indicated that this alteration led to less localized plastic like deformation [95]. This phenomenon may be transferred to the difference described between the HBPA-DGE and DGEBA samples, as the shear bands in HBPA-DGE tend to be more local (see Figure 5.19).

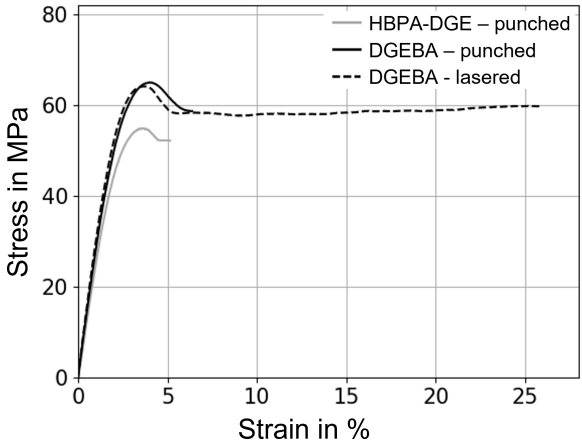

Figure 5.10: Representative stress-strain curves of film samples of type A and a thickness of 30 µm made of HBPA-DGE and DGEBA resin. The sample geometry is created via punching and for DGEBA by laser as well. All samples loaded with a crosshead speed of 1 mm/min at room temperature.

Figure 5.11 shows a representative stress-strain curve of a type C epoxy film specimen with a thickness of 30 µm. The elongation at break is 85 % and the tensile strength is about 54 MPa for this sample. The general mechanical properties for the samples tested without DIC pattern is about 77.3 ± 6.1 % for the elongation at break and 52.0 ± 2.8 MPa for the tensile strength. The latter is reduced compared to the film sample with geometry A (probably due to the even more challenging handling), but the global strain at break is remarkable for an archetypal brittle epoxy material and is significantly increased compared to the standard bulk samples (mostly less than 10 %) and the other epoxy film samples with a larger test volume (geometry A). The global strain values measured by the crosshead displacement were validated with the global strain values determined by the DIC software, and they are almost identical.

After yielding, the engineering stress decreases and strain softening takes place. Especially around global strains of 32 %, 52 % and 72 % (see Figure 5.11 the black arrows), stress decreases followed by an increase (strain hardening) with further tensile deformation. This type of behavior can also be found for epoxy volumes tested under pure shear [188], but not for standard bulk samples under tension at room temperature [189]. This macroscopic strain softening and hardening might be explained as follows. Global stress decreases due to the presumed unraveling of entanglements and molecular alignments inside the material. After the stress is partially relaxed by the molecular movements and visible shear bands are formed in some sample areas, the stress increases again because of the hardening effect of the molecule chains aligned in the tensile direction inside the deforming sample.

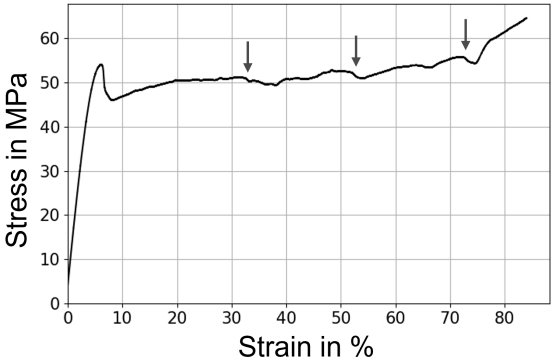

Figure 5.11: Representative stress-strain curve of an epoxy type C film specimen with a thickness of 30 µm (Nanoindenter tensile stage). The black arrows indicate strain softening.

Strain softening and hardening can be found, for example, in glassy thermoplastics [190, 191] or some amorphous thermosets under compression load [192]. To the knowledge of the authors, strain softening and hardening with accompanying formation of shear bands for neat epoxy has so far only been observed sporadically in compression tests and tensile tests at elevated temperatures [193], but not yet for tensile tests at room temperature. In the study of Sui et al., microscale epoxy fibers having a gauge length of 10 mm and diameters between 30 and 120 µm exhibited strain softening and hardening under tensile load, but shear bands were not observed in these necked fibers and no complete explanation for this phenomena on a molecular level was presented [6].

Tensile tests at different temperatures

According to DIN EN ISO 527-3, at least five film samples with a thickness of 50 µm per temperature are tested with the Gabor Eplexor DMTA test machine. In Figure 5.12 representative stress-strain curves of three different temperatures are shown, and in Table 5.3 the mechanical properties at different test temperatures are listed.

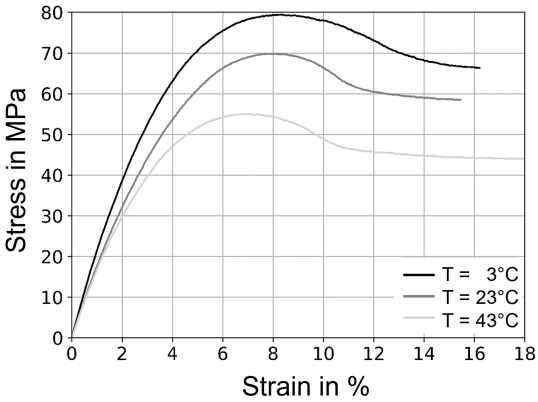

Figure 5.12: Representative stress-strain curves for film samples of type A with a thickness of 50 µm and a crosshead speed of 1 mm/min at different test temperatures (DMTA).

Table 5.3: Mechanical properties (tensile strength (UTS), Young's modulus (E), and elongation at break (ϵ_b) of type A epoxy films with a thickness of 50 µm determined in a tensile test using a DMTA machine with a crosshead speed of 1 mm/min at different test temperatures.

	Test temperature T in °C					
	3	**13**	**23**	**33**	**43**	**53**
***UTS* in MPa**	79.2 ± 1.0	70.7 ± 1.2	69.3 ± 2.4	61.6 ± 3.4	52.2 ± 3.3	49.4 ± 1.1
***E* in MPa**	2244.3 ± 36.3	1941.6 ± 50.5	1884.6 ± 67.6	1817.2 ± 120.5	1673.5 ± 160.1	1498.4 ± 189.6
ϵ_b in %	13.8 ± 4.5	10.9 ± 1.9	11.9 ± 3.8	18.0 ± 10.6	22.5 ± 8.0	31.6 ± 18.2

The pronounced plastic like behavior of the film specimens is noticeable in these curves, even at lower temperatures (T = 3 °C). It can be seen that tensile tested specimens at higher temperatures (T = 43 °C) are associated with a lower tensile strength, a higher elongation at break and a lower Young's modulus.

These mechanical behaviors at lower and higher temperatures as room temperature correspond to other studies on thermosets in general and on the same epoxy material in particular [189]. The main difference is that epoxy as the film specimen shows plastic like deformation in the form of pronounced shear bands, even at low temperatures.

5.2.2 Creep test

The (*in situ* IR) creep test approach is expected to provide a deeper insight into the deformation process by acquiring time-dependent mechanical data. A total of twelve samples are examined with a thickness of 30 µm by using the Deben microstage. Figure 5.13 shows the creep curve of a type A sample with a thickness of 30 µm, which has reached the maximum elongation of 17 % that can be performed with the Deben tensile microstage without failure.

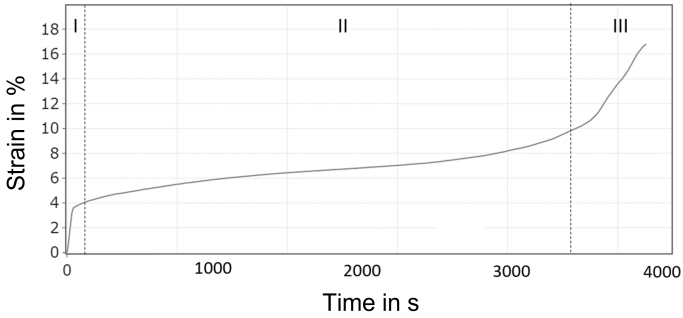

Figure 5.13: Creep curve of a type A film specimen with a thickness of 30 µm (Deben tensile microstage). The creep curve shows the strain evolution over time for 56 MPa (80 % UTS) and the three creep phases. A photoelastic image of this creep loaded and deformed sample is shown in Figure 5.33 (left)

The creep curve in Figure 5.13 represents the three typical phases of creep behavior. Within the first few seconds, spontaneous elastic and viscoelastic deformations cause the specimen to elongate during initial loading and decrease in creep velocity due to hardening processes (creep phase 1). As time progresses, there is a constant and low creep rate where hardening and softening processes are roughly balanced and the beginning of a continuous reduction in the transverse section due to constant load application (creep phase 2).

This can be seen in the Appendix in Figure 12 and in Figure 13 in the photo and photoelastic images. As a result, the true stress in the contracted test area is increased accordingly, whereas the engineering stress in the graph is constant. Finally, the creep strain increases rapidly until the fracture occurs (excess stress due to local necking or irreversible material changes) (creep phase 3). However, the deformation behavior observed here is unusual for the typical at room temperature brittle epoxy resin.

Figure 14 in the Appendix shows the creep curve for a type A sample (thickness of 30 µm) at a stress level of 60 % UTS and Figure 15 pictured the recorded creep curve of type A sample (thickness 30 µm) at 65 % UTS. Both figures show the corresponding photoelastic image of the tested sample as well. Regardless of the stress level, the shape of the creep curves and the creep phases mentioned for the film samples are quite similar, but the strains reached and the test duration differ, as well as the deformation and shear band intensity (as can be seen in the Appendix in Figure 14 and 15). This might be due to the challenging sample handling and clamping. For some samples the elongation at break is greater than for the creep tested samples with the Deben microstage with a maximum strain of 17 % (see Appendix Figure 14).

It was not possible to detect a linear relationship between the logarithm of creep rate $\dot{\epsilon}$ and stress level σ for epoxy film samples tested at the stress levels presented as it is often the case for metals [176]. This approach is therefore not further elaborated in this thesis.

5.2.3 Cyclic loading

In Figure 5.14 a creep and cyclic strain curve recorded during the testing time of type A film specimens with a thickness of 30 µm is shown. The creep stress level and the maximum stress in the cyclic loading are approximately 70 % UTS. It can be seen that the cyclic viscous strain component follows the creep strain curve. The gray cyclic strain curve indicates a nearly linear increase of strain during the loading cycles and a sudden decrease of the elastic deformation component with the beginning of the unloading cycles. During the unloading cycles a time-dependent, almost linear viscoelastic strain decrease can be observed with increasing time of the unloading phases due to molecular relaxation processes.

It turns out that the mechanical material behavior is not only elastic, but also viscoelastic and plastic. The corresponding molecular processes are explained and discussed more in detail in Chapter 5.3.

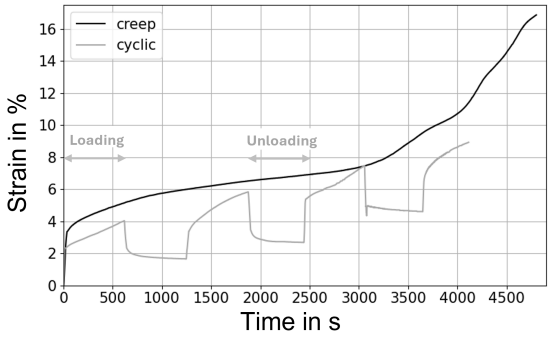

Figure 5.14: Creep and cyclic strain during the testing time of type A film specimens with a thickness of 30 µm (Deben tensile microstage). The creep stress level and the maximum stress in the cyclic loading is about 70 % UTS.

The results of the cyclic test of a type A sample (thickness 30 µm) with a frequency of 1 Hz, a stress ratio $R = 0.1$ and a maximum stress of 45 MPa (65 % UTS) with a MMT-250NV-10 test machine are shown in Figure 5.15.

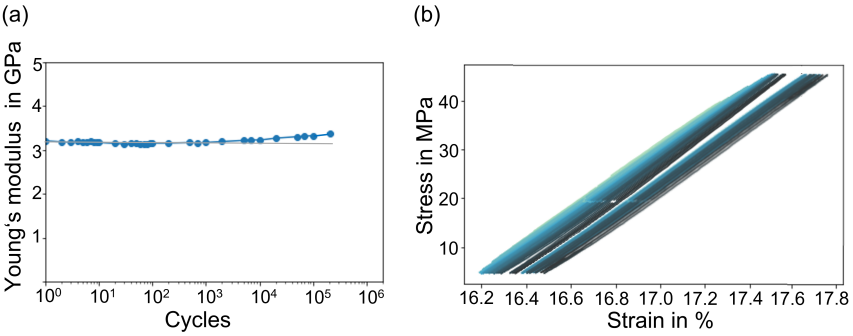

Figure 5.15: Evaluation of Young's modulus during cyclic loading cycles with a frequency of 1 Hz of a type A sample with a thickness of 30 µm and a maximum stress of 65 % UTS (a). The sample failed after 269 037 cycles (MMT-250NV-10 test machine). The cyclic test was interrupted after 100 000 cycles (predefined cycle limit) and immediately restarted. The corresponding hysteresis curves are shown in (b).

The evaluation of the Young's modulus over the cycles indicates a slight decrease after approximately 10 cycles and an increase after 1000 cycles. This is in accordance with the strain softening and hardening effects that were detected for the type C film samples during the tensile test (see Figure 5.11). The molecules might become partly oriented during the cyclic loading, which results in a slight increase in stiffness before finial failure.

5.2.4 Photoelasticity, µ-CT and Microscopy

Figure 5.16 shows photoelastic images of a representative creep-loaded film specimen with a thickness of 30 µm at an elongation of 17 % (a). In addition, a representative sample with a thickness of 30 µm tensile tested, which reaches an elongation at the break of 12 % is shown in Figure 5.16 (b). For the latter, a reduced width can be observed in the failure area of a sample, which matches the characteristic stress-strain curve of the tensile test (see Figure 5.9). The same applies to the specimen loaded in the creep test, where the neck or more precisely the width reduction of the specimen, fits to the strong strain increase in the third creep phase at the end of creep curve (see Figure 5.13). The Poisson's ratio of standard epoxy samples is around 0.35 [194]. The yellow regions indicate mechanical stresses within the epoxy samples. What is again particularly remarkable is that there are also shear bands clearly visible in the necked epoxy specimen region of the tensile and creep loaded and thereby plastically like deformed specimens, which is very unusual for thermoset materials in general and for epoxy resins in particular.

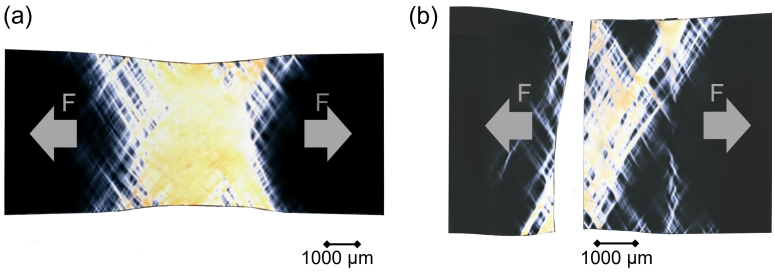

Figure 5.16: Photoelastic images of a type A film specimen (30 µm) after an elongation of 17 % in the creep test (a) and a type A film specimen (30 µm) after tensile test with failure (b), both samples have a thickness of 30 µm and illustrating a reduction in the width and shear bands.

Figure 5.17 shows a microscope image which was made by using a Keyence VK-X3000 microscope in laser scanning mode. The thickness deviation in a deformed sample region with shear bands (investigated lengths of approximately 300 µm) was exemplary for a creep-loaded type A sample with a thickness of 30 µm determined. The thickness in shear bands is for this sample region about 2.14 µm less than in the neighboring sample regions. The deformation and shear band formation results in not only a decrease in width (see Figure 5.16) but also in thickness. The latter is also measurable with a dial gauge and can be investigated with a higher spatial resolution and for the entire sample area by performing µ-CT measurements on the creep loaded sample which is shown in a photoelastic image in Figure 5.34.

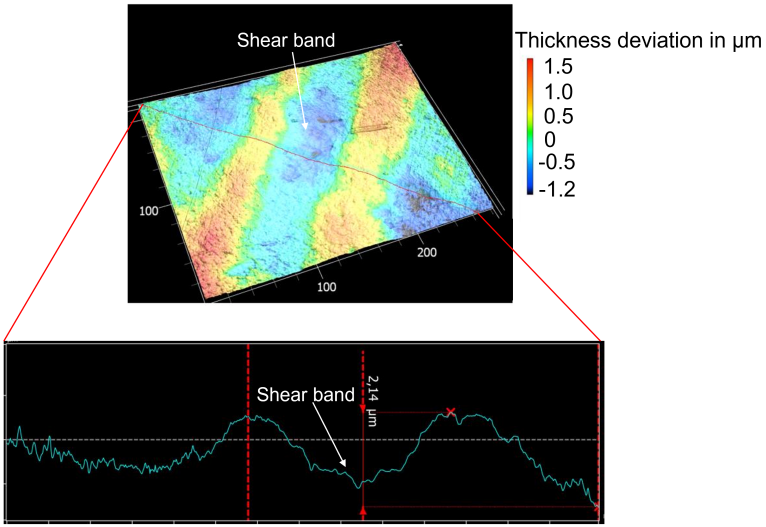

Figure 5.17: Microscopic analysis of the thickness deviation in a deformed sample region with shear bands. The thickness values are determined in a line with a length about 300 µm through shear bands. The investigated sample is a type A sample with an original thickness of 30 µm which was creep loaded (70 % UTS) with the Deben microtest device until a maximum elongation of 17 %.

Figure 5.18 (a) shows a visualization of the thickness distribution of a deformed and creep-loaded type A sample with a thickness of 30 µm. The shear bands can be recognized in this visualization in red, which corresponds to a significantly reduced thickness of up to 20 µm.

The overall reduction due to the deformation process and shear band formation is in some regions even greater than 10 µm, that is, more than a third of the initial thickness. The corresponding counts of a specific thickness in the investigated sample region are plotted in a histogram in Figure 5.18 (b). The histogram of the deformed sample differs from the symmetric bell-shaped distribution of an initial as produced sample and shows an asymmetric distribution toward lower thicknesses due to the thickness reduced shear band areas.

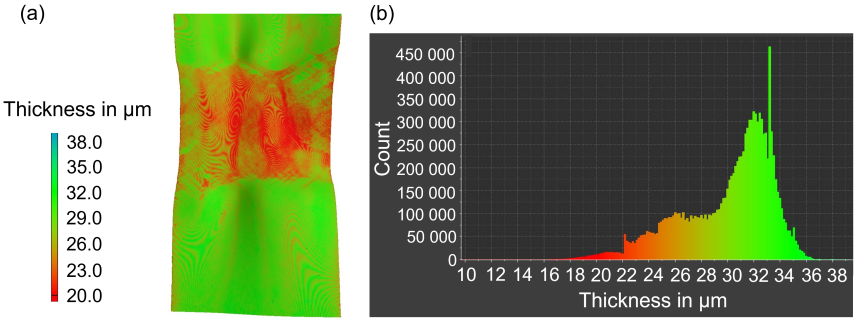

Figure 5.18: µ-CT analysis of the thickness distribution of a deformed sample with shear bands. The thickness values are determined with a voxel size of 5.5 µm through the deformed region. The investigated sample is a type A sample with an initial selected thickness of 30 µm which was creep loaded (70 % UTS) with the Deben microtest device until a maximum elongation of 17 %. (a) shows the distribution with a thickness-reduced shear band as a visualization for the investigated sample region and (b) is a histogram with pictured the counts of a specific thickness in the investigated sample region.

HBPA-DGB type A samples with a thickness of 30 µm show shear bands as well. A tensile tested HPBA-DGE sample is shown in Figure 5.19. No significant difference in the shear band structure between the DGEBA and HBPA-DGE samples is visible.

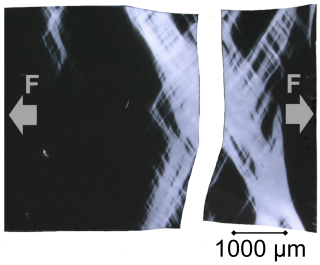

Figure 5.19: Photoelastic image of a HBPA-DGE type A film specimen (30 µm) after tensile test with a reduction in the width and shear bands.

Regions of plastic deformation due to shear stress are actually a typical example of the non-linear deformation behavior of thermoplastics, e.g. acrylonitrile-butadiene-styrene copolymerisate (ABS). The shear bands represent an orientation inhomogeneity (see Chapter 2.1) and usually occur at an angle of ± 45° to 55° to the direction of loading, which corresponds to the direction of maximun shear stresses (this angle may deviate due to superposition with normal stresses) [57]. The formation of shear bands is favored by a stress-related decrease in volume [195], as explained in Chapter 2.1. However, the explanations for thermoplastics should not be transferable to thermosets, as these are closely cross-linked and the macromolecular chains cannot slide as easily due to the cross-linking.

The shear bands and neck gauge length of the type C specimens with a significant reduced gauge volume can also be visualized in photoelastic digital microscope images, as can be seen in Figure 5.20 for two representative epoxy film samples of type C after tensile testing. The bright and yellow regions are highly deformed as the width is reduced and shear band structures can be detected.

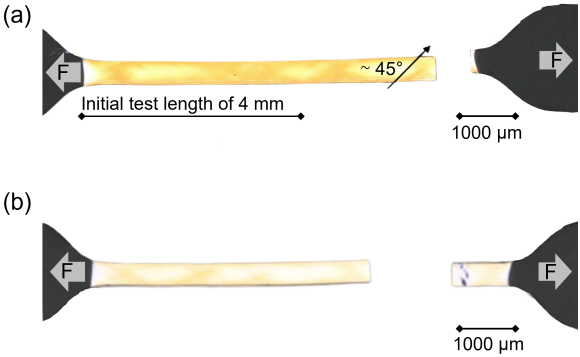

Figure 5.20: Photoelastic images of deformed film samples of type C and a thickness of 30 µm after tensile testing (elongation at break $\epsilon_b = 74\,\%$ (a) and $\epsilon_b = 71\,\%$ (b)). The initial gauge length is marked and shear band structures in 45° to 55° direction are visible.

Some of the creep loaded bulk samples with a thickness of 2000 µm show some shear band like structures which can also be visualized by photoelastic imaging as can be seen in Figure 5.21 for a bulk sample tested at a load level of 70 % UTS. The shear band formation was sometimes visible by eyes during the mechanical tests, but often not anymore after finial failure. The shear bands seems to be located close to the surfaces and the bulk samples exhibit no significant thickness and width reduction in comparison to the film samples. This means that in bulk samples shear bands are a surface phenomena. At the surface or close to it, there occurs a plane stress state (see Chapter 2.1) which favors plastic deformation. Furthermore, the molecules close to the bulk sample surfaces have less neighboring and connecting molecules and can therefore be rearranged more easily in comparison to the molecules that are more in the sample center with more spatial hindrance. This leads to a shear band formation on the bulk samples surfaces. Additionally, there might be some small surface and edge defects due to the shaping milling process, which causes stress concentrations and the required yield stress might be reached there. The stress distribution might be more uniform compared to the film samples, so that despite these near-surface effects, very early failure might be suppressed for all tested bulk samples.

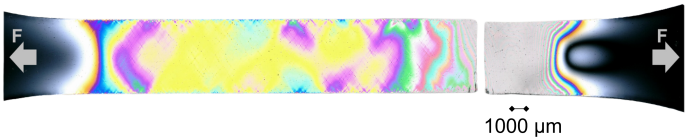

Figure 5.21: Photoelastic image of deformed bulk samples with a thickness of 2000 µm after creep loading (70 % UTS).

5.2.5 Digital Image Correlation

Digital image correlation (DIC) was used as a method to visualize local strains (and therefore also stresses) over the whole sample area during a tensile test. This is shown in Figure 5.22 for a 100 µm thick and deformed type A sample at a relatively high stress and a global strain of 20 % close to the value of elongation at break for this sample. It can be clearly seen that in regions with relatively high local strains (over 40 %), shear bands develop in approximately 45° direction.

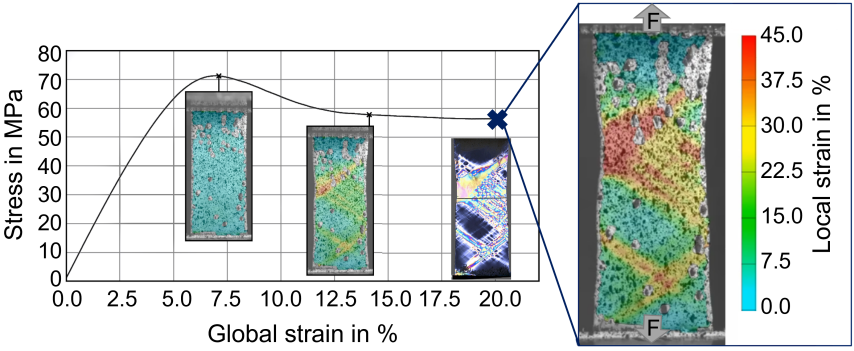

Figure 5.22: Stress-strain curve of a film specimen of type A with a thickness of 100 µm recorded during a tension test at room temperature with a crosshead speed 1 mm/min. Additionally the DIC images for the global strains of approximately 7 % , 13.5 % and 20 % are shown with the visualized local strain values. It is clearly visible that high local elongation (over 40 %) occurs in areas of the shear bands shortly before finial failure, as can be seen in the photoelastic image at a global strain of 20 %.

The shear band orientation of 45-55 degrees in the tensile direction and reduced gauge width can also be seen in the DIC deformation field data shown in Figure 5.23 (left) for a type C sample [154].

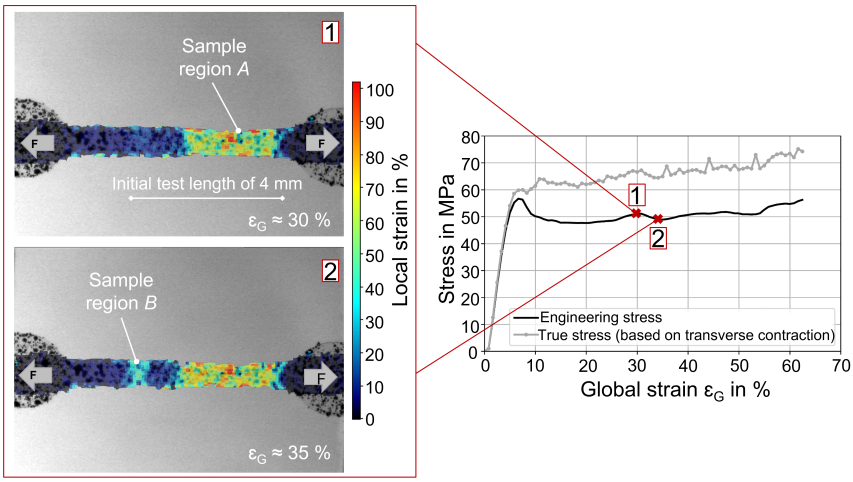

Figure 5.23: Visualized DIC data at a global strain of 30 % (image 1, top) and 35 % (image 2, bottom) and the corresponding engineering stress-strain curve (black) and true stress-strain curve (gray, based on maximal transverse contraction in the gauge length from the DIC data) of a representative type C sample. The DIC field data is shown by colorized quadrilaterals so that the subset size used in the calculation corresponds to 3 x 3 = 9 quadrilaterals in this Figure.

As described, after the yield stress is reached, the sample does not deform uniformly. Here, a distinct deformation can be seen in the right-hand part (region *A*) of the sample gauge section (see Figure 5.23 (left, 1)). The maximum local strain reaches values of up to 100 %. The local deformation phenomena are also evident in the global engineering stress-strain curve, as can be seen in Figure 5.23 (right). During the formation and growth of the local deformation region *A*, the stress remains relatively constant. After a specific level of molecular orientation in the tensile direction has been reached, strain hardening takes place, and the stress increases as the aligned molecular backbones are further stressed and stretched. The stress maximum for the deformation region *A* is reached at approximately 30 % global strain. When a global strain of 35 % is reached, larger local strain values develop in sample region B, where a second shear band begins to form within the gauge length, as can be seen in Figure 5.23 (left, 2). This correlates with a decrease in global stress, as the external mechanical energy is responded with molecular backbone movement processes, as can be seen in the corresponding engineering stress-strain curve (strain softening).

The second deformation zone probably appears because the maximum possible amount of deformation for the first deformation region is reached and the yield stress required for a second deformation zone arises in the left sample side around region *B*. Thus, the formation of a new deformation on the left-hand side of the specimen (region *B*) is energetically more feasible than continued deformation in the first zone (region *A*), where hardening resulting from local molecular reorientation has already taken place. At the end of the tensile test or before final failure, a large part of the sample gauge length is deformed, i.e. most of the backbone chains are oriented, and the stress increases again. To take the width reduction into account, the true stress-strain curve for the same sample was determined based on the local maximum contraction in transverse direction within the gauge length for each time increment. However, it is not possible to include possible load-induced thickness changes in this method. This is why the initial thickness is taken for this procedure.

The true stress curve is also shown in gray in Figure 5.23 (right). Since the measured contraction in the transverse direction depends on the quality of the DIC pattern, the true stress-strain curve contains some fluctuations. As expected, the overall trend shows increasing stress values after reaching the yield stress, since the true cross-section decreases as a result of the reduction in widths. However, in the true stress curve, the aforementioned peaks of strain hardening and strain softening are still visible at the same global strain values.

DIC data for a film sample presented in Figure 5.23 was further analyzed with respect to strain softening and hardening effects. A detailed DIC investigation was performed where different sections along the gauge length of 4 mm were compared to each other. This is visualized in Figure 5.24. The y-axis of the graph (Figure 5.24, right) shows the global strain or progress in the tensile test. By assigning the local strain values to a color scale, it was possible to visualize and determine the local strains for each selected specimen position.

The positions of the samples and the assigned numbers were selected in relation to the beginning of an increase in the local strain values (as indicated in Figure 5.24), i.e. the numbers represent the chronological order. At the beginning of the tensile test in the elastic and viscoelastic region, i.e. at low global strains, there is no reduction of the widths or high local strain values detectable (with the color scale used, the entire gauge length is blue).

At sample position 1, the local strain increases, deformation, and shear bands start and grow in the direction of positions 2 and 3. As the tensile test progresses, in these sample regions, local strain values increase further. As mentioned above (see Figure 5.23), with further increased global strain to around 35 %, a second deformation zone is created at position 4. This deformation zone extends in the direction of positions 5 and 6. At the end of the tensile test or shortly before the final failure, the entire gauge length has a reduced width except for a small sample region on the left side next to position 6.

The width averaged local strain curves at these six selected positions on the specimen gauge length during the progress of the tensile test are shown in Figure 5.25. The local strain values were calculated for each time as an average local strain across the sample width. It can be seen that the strain curves for all selected sample positions follow a similar pattern. In the beginning of the tensile test, there are only moderate local strain values and a slight gradient due to the elastic and viscoelastic behavior of the epoxy. As the tensile test progresses, a steep increase in local strain is first observed at position 1. Here, the strain increases to a maximum local strain value of approximately 60 % and the local strain value remains almost constant afterwards. When reaching the constant strain value in position 1, the local strain in position 2 starts to increase, as well as in position 3 since the deformation grows in both directions. In the same way, it can be seen that the local strain of position 5 increases sharply when the local strain of position 4 is reaching the constant or maximum value. The difference in the local strain histories for positions 5 and 6 is minor as the deformation grows from position 4 in both directions (towards positions 5 and 6). These results imply that, at the microscopic level, after a sufficient stress level is reached, the backbones can be oriented and stretched within the epoxy material until a characteristic threshold (of strain hardening), which is similar in all regions (local strain around 60 %), is reached. Stretching may include an increase in a lengths of load-bearing bonds and a more linear conformation as well as a load path orientation of the molecules. Afterward, it seems to be not possible to increase the local deformation even further and it might be energetically more favorable to continue the deformation process in another region of the sample, where the local yield stress is reached and the molecules are less oriented and stretched. When all regions reach local strain values of 60 %, a further increase might not be possible since the bond energy might be reached and simultaneous bond break could occur (see Chapter 2.3), leading to finial failure.

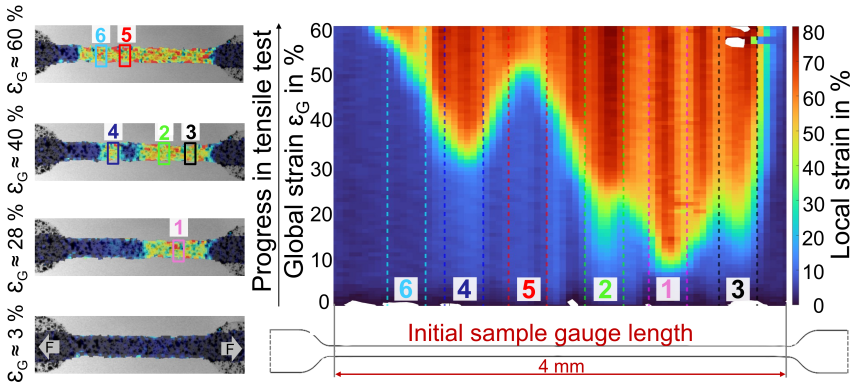

Figure 5.24: Visualized DIC data including the local strains, which are colored regarding the corresponding strain values, during the tensile test (global strain) for selected sample positions in the initial gauge length (the numbers represent the chronological order of the beginning of an increase in the local strain).

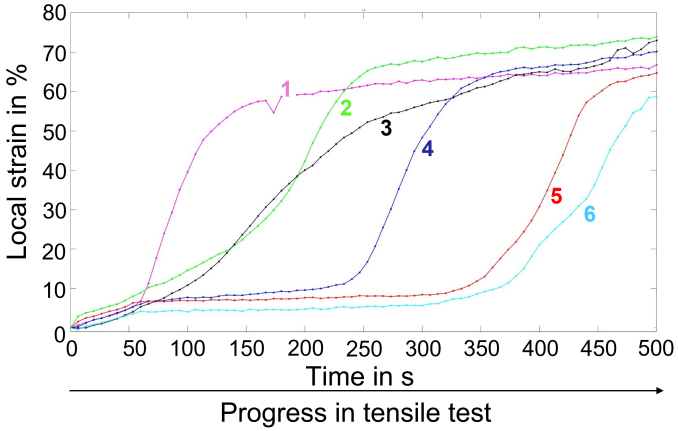

Figure 5.25: Width averaged local strain curves for 6 selected locations on the initial gauge length over the tensile test duration (see Figure 5.24).

Intermediate summary

Mechanical and supportive results show that epoxy microscale samples can behave ductile by applying a comparative slow tensile load application (crosshead speed of 1 mm/min) even at room temperature. This indicates that at room temperature the epoxy material deformation is not only energy elastic (changes in bond distance and angles), but entropy elastic (molecular rearrangements) as well. In addition, a remaining deformation occurs as well. With photoelastic imagining, it was possible to detect shear bands in the deformed sample regions. Shear bands were detected as sample zones with reduced thickness compared to initial thickness, which was observed in µ-CT and microscopic investigations. Furthermore, the locale strain values in the shear bands are comparatively high and can reach values up to 60 %. The stress within the formed shear bands might also be higher. In the shear bands, the molecular rearrangement process might take place and the backbones may be aligned in load direction. This comes together with the observed strain softening. After this process or simultaneously, the backbones are stretched and strain hardening is detectable in the stress-strain curves (see Figure 5.11). This molecular process is supported by the slight increase in stiffness or Young's modulus observed during the cyclic testing (see Figure 5.15).
Overall, it was possible to support the first and second hypotheses proposed with the mechanical tests:

1. *Micro-scaled thin epoxy resin films can deform ductile under tensile loads.*

2. *High local strains and stress results in shear bands as visible deformation mechanisms under tensile loads.*

In order to gain a deeper understanding of the molecular mechanisms that cause this mechanical behavior and to explore the molecular structure of the formed shear bands, in the following sections, the results of *ex situ* and *in situ* (polarized) Infrared (IR) and Raman spectroscopy are figured out and discussed.

5.3 Infrared spectroscopy

A transmission spectrum of an initial as-produce type A sample with a thickness of 30 µm is shown in Figure 5.26, where the individual epoxy peaks are mentioned.

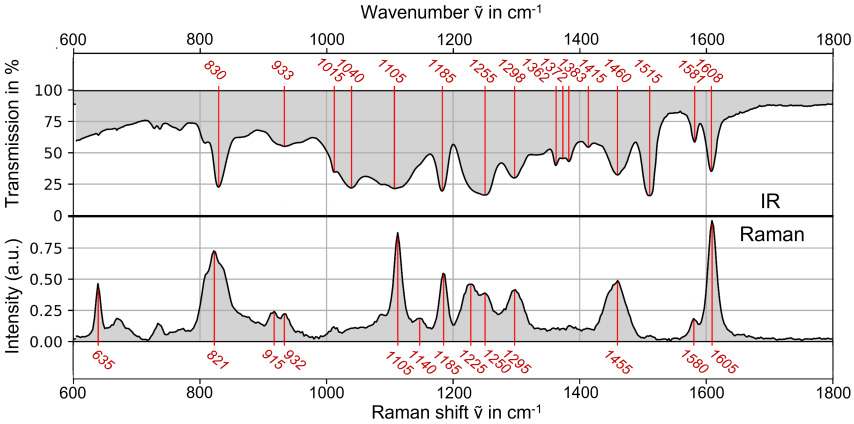

Figure 5.26: IR and Raman spectra (filled gray) of an as-produced epoxy film sample type A with a thickness of 30 µm.

In Figure 5.27 representative absorbance spectra of as-produced type A epoxy film samples with different thicknesses are shown. It is noticeable that the thicker the film, the higher the absorbance for all peaks. This relationship is described by the fundamental Beer's law (see Equation 2.12). This means that the absorbance of any component is proportional to the sample thickness if the chemical composition, e.g. the molecular concentrations, remains unchanged.

The quantitative evaluation is carried out by converting the transmission into absorbance (see Equation 4.3), whereby the noise in areas of total absorption is considerably amplified by the logarithm function. So, at relatively high absorbance values, even a small amount of noise has a dramatic effect on the absorbance. For a spectrum with a root-mean-square (rms) signal-to-noise ratio (SNR_{rms}) of 1000 : 1, the rms noise is ± 0.001 transmittance. If the rms noise is ± 0.001, the peak-to-peak noise will be approximately five times higher, or transmittance ± 0.005. This corresponds to an absorbance range of a peak ostensibly at 2.00 of 2.30 to 1.82 (a.u.) [146].

For an assessment of the absorption, the region of total absorption, i.e., with < 0.1 % transmission (absorbance A > 3) is colored red. The absorbance region close to total absorption with < 1 % transmission (A > 2) is colored orange in Figure 5.27. For the 50 µm thick samples, the noise in some wavenumber regions is obvious, and some peaks are even in the red absorbance region. For samples with a thickness of 30 µm no peaks are in the red absorbance zone, but in the orange. Only for samples with a thickness of 15 µm, all peaks have relatively low absorbances. The peak absorbances of film samples with a thickness of 100 µm are way too high for a quantitative analysis in transmission mode. That is why no IR spectroscopic results of these thick samples are presented in this theses. Due to comparatively reasons, the wavenumber axis is chosen in the same way as for the Raman spectra, even if the standard way for IR spectra is to plot the wavenumber from large to small. In this thesis, the wavenumber axes of Raman and IR spectra are shown uniformly from small to large values.

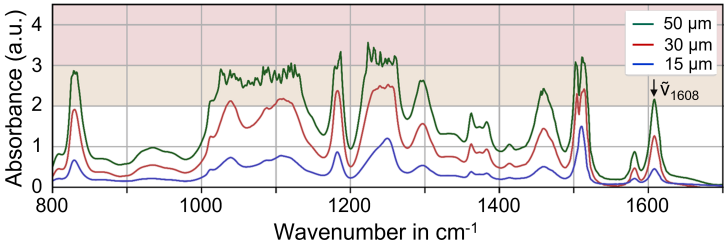

Figure 5.27: Representative IR spectra of as-produced film specimens of type A with different thicknesses are shown. All peaks in the red or orange colored absorbance zone are not suitable for the IR analysis (e.g. wavenumber $\tilde{\nu}_{\mathrm{Peak}}$) due to the high or total absorbance.

In Table 5.4 all epoxy IR peak wavenumbers $\tilde{\nu}_{Peak}$ are listed together with the corresponding molecule vibration modes. It should be noted that the literature often only gives ranges for the peak wavenumbers, since the exact peak wavenumber always depends on how the respective molecule is bound to other molecules and which substitutes are present (see Chapter 2.3.1). In addition, superpositions often occur, i.e. different molecules vibrate at the same wavenumbers. This can lead to different classifications in the literature. For this reason, this table should not be interpreted as all-encompassing and serves more as a guide.

Table 5.4: List of MIR Peak wavenumbers $\tilde{\nu}_{Peak}$ of epoxy film samples with the corresponding molecule vibration modes in the fingerprint range. The information is taken from the literature [137, 138, 196–209].

Peak wavenumber $\tilde{\nu}_{Peak}$ in cm^{-1}	**Molecule vibration modes**
829	H out-of-plane bending of *para*-phenylene
933	CH_2 out-of-plane stretching
1015	Symmetric in-plane semicircle stretching of *para*-phenylene and aliphatic ether
1040	Stretching of the aromatic ether between CH_2 and O
1105	Asymmetric stretching of aliphatic ether and secondary alcohol
1182	In-plane CC stretching of *gem*-dimethyl-groups between *para*-phenylene
1255	Stretching of the aromatic ether between *para*-phenylene and O
1298	OH in-plane bending and vibration of tertiary amines
1362	CH bending of CH_3
1383	CH bending of CH_3
1412	Asymmetric in-plane semicircle stretching of *para*-phenylene
1460	Bending of CH_2 and CH_3
1471	CH bending of CH_2 and C stretching in *para*-phenylene
1515	Symmetric in-plane semicircle stretching of *para*-phenylene
1581	Asymmetric in-plane quadrant stretching of *para*-phenylene
1608	Symmetric in-plane quadrant stretching of *para*-phenylene

The vibrations that can be assigned to the aromatic rings or more precisely the *para*-phenylene group can be clearly attributed, which is why the focus of this work is on the corresponding peaks. The *para*-phenylene group refers to an aromatic structure based on phenylene, a term that refers to compounds derived directly from benzene. The therm *para* refers to the positions of the functional groups or substitutes on an aromatic ring. If two functional groups are arranged in a 1,4-position around the ring, as in DGEBA, the oxygen atoms and the *gem*-dimethyl groups (see Figure 5.28), the carbon atoms which are connected to the other backbone parts, are in opposite *para*-position to each other with two aromatic carbon atoms in between. The carbon atoms that are connected are, therefore, named C_1 and C_4. This is shown in Figure, where C_1 is bonded on an oxygen atom and C_4 is connected to another carbon atom of the *gem*-dimethyl-groups. In the following thesis these carbon atoms are often also called aromatic C-C atoms for reasons of simplicity.

Vibrational modes of stress-sensitive bonds must exist in the spectrum of the epoxy films. Moreover, extracting peak shifts and spectral changes from complex spectra with overlapping, mutually, and dependently shifting peaks is a challenge as well. It is often only possible to consider well-resolved bands of relatively high intensity [210]. Therefore, total absorbance or relatively less intensity of the stress-sensitive bonds is not appropriate for the developed peak fitting method. The vibration modes of stress-sensitive bonds usually consist of at least one molecular component that is directly involved in a load-bearing action in the skeleton of the chain [179]. As observed in the study by Doblies et al. on epoxy samples, some peaks of stress-sensitive bonds show a load-induced change in the associated peak wavenumber [159]. Thus, a wavenumber-dependent change under loading can be detected. This allows an evaluation of the correlation between the peak position, in the following called the peak wavenumber $\tilde{v}_{Peak}$, and structural changes of stress-sensitive molecular components in epoxy. However, the ether peaks (first overtone at $2070\,\mathrm{cm}^{-1}$) selected in the study of epoxy by Doblies et al. (see Chapter 2.3.2) were not found to be a suitable vibration mode for the present study due to the low intensity caused by the comparatively lower sample thickness (Beer's law; see Equation 2.12). However, in this study, the focus is on a peak of the intramolecular aromatic C-C bonds in the DGEBA resin backbones (see Figure 5.28 (a)) and its vibration mode as this peak met the requirements for the peak analysis.

Since aromatic molecules or more precisely the *para*-phenylene group and the corresponding C (carbon) bonds are part of the backbone, they are directly responsible for the transmission of force during load application to film samples through covalent bonds. A corresponding peak can be found at 1608 cm^{-1} and is accompanied by an in-plane stretching of the aromatic ring and mainly its C atoms. In Figure 5.28 (b) the corresponding vibration mode at a wavenumber $\tilde{\nu}_{1608}$ is schematically illustrated. This peak $\tilde{\nu}_{1608}$ exhibits load-induced wavenumber changes toward lower values, called a red-shift (see Chapter 2.3.2). The peak can be found in the measured IR spectra of as-produced epoxy film specimens, as marked in Figure 5.27 and is referred to when *aromatic vibration* is mentioned in this thesis. Even if the other epoxy peaks are not as suitable for spectral analysis (e.g., peak shift) as for the presented peak and its vibration, other peaks related to the aromatic ring at 829 cm^{-1}, 1412 cm^{-1} and 1581 cm^{-1} are investigated for the sake of completeness in this thesis as well. The peaks at 1182 cm^{-1} (in-plane CC stretching of *gem*-dimethyl-groups between *para*-phenylene groups), at 1298 cm^{-1} (tertiary amines) and at 1362 cm^{-1} (CH bending of CH_3) are additionally analyzed.

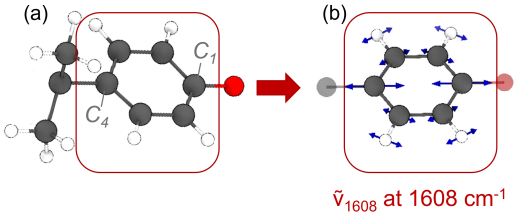

Figure 5.28: Schematically illustration of the aromatic *para*-phenylene group (connected to *gem*-dymethyl-group) (a) and of the vibration mode at a peak wavenumber $\tilde{\nu}_{1608}$ at 1608 cm^{-1} (b) (red = oxygen, white = hydrogen and gray = carbon atoms).

Another general requirement for peak shift analysis is that the device scattering of the wavenumbers in general and for the mainly investigated peak wavenumber $\tilde{\nu}_{1608}$ in particular is negligibly small compared to the load-induced peak shifts. That is why the device-related scattering of $\tilde{\nu}_{1608}$ of the initial as-produced sample state was thoroughly examined. The results show that the scattering of the peak wavenumber $\tilde{\nu}_{1608}$ is 1608.253 $\pm$ 0.016 cm^{-1} for the TENSOR II device and 1608.229 $\pm$ 0.021 cm^{-1} for the HYPERION microscope used.

5.3.1 Ex situ Infrared spectroscopy

Changes in the molecular backbone induced by load are analyzed by comparing the IR spectrum of the as-produced or unloaded film samples and at room temperature tensile loaded film samples with a thickness of 30 µm. For this purpose, 100 IR spectra are recorded in an investigated circular area with a diameter of 4 mm per specimen position with a TENSOR II spectrometer (see Chapter 4.4.2). According to the IR evaluation steps of the raw IR data (see Figure 4.4), all recorded spectra are processed in a uniform manner prior to comparison.

A load-induced difference of the peak wavenumber $\tilde{v}_{1608}$ of the aromatic *para*-phenylene group at 1608 cm^{-1} before and after mechanical loading can be identified. After mechanical loading, the deformed samples showed that the center of the aromatic peak or the maximum at $\tilde{v}_{1608}$ is shifted to lower wavenumbers compared to the initial film state, as can be seen in Figure 5.29. The peak shift $\Delta\tilde{v}_{1608}$ is considered to be significant because the detected peak shift is larger than the device-related scattering.

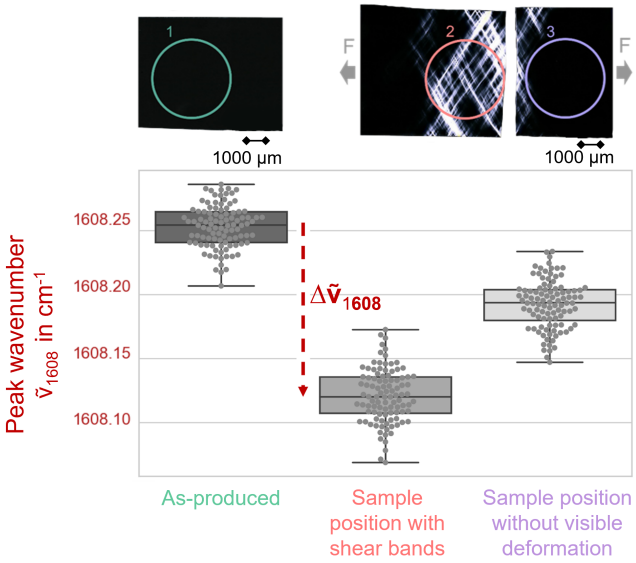

Figure 5.29: Wavenumbers of the aromatic peak $\tilde{v}_{1608}$ for an unloaded film type A sample with a thickness of 30 µm and different specimen regions of the film specimen after tensile test at room temperature. The corresponding photoelastic images are shown as well.

Three different IR measurements per film specimen are shown (1. As-produced specimen before mechanical loading, 2. Sample area of plastic like deformation with shear bands and necking after loading and 3. Sample region without visually visible plastic like deformation after loading). Each gray dot is related to a spectrum recorded and processed at the corresponding sample position. The peak wavenumber $\tilde{v}_{1608}$ is extracted from the processed spectrum, as described in Chapter 4.4. If the peak position $\tilde{v}_{1608}$ of the three spectra (as produced, non visible deformation after tensile test and visible deformation after tensile test) are compared with each other, this results in an order for the corresponding peak shift. The sample region with shear bands (2.) exhibits a significantly lower wavenumber for the aromatic C-C peak even after stress relief and elastic recovery due to final failure. The peak $\tilde{v}_{1608}$ for sample areas without visible plastic deformation after tensile testing (3.) is in the middle range, i.e. it shows higher wavenumber values than the position with shear bands and lower values than the originally unloaded film. Plastic like deformation or shear bands result in non-elastic molecular changes in the aromatic C-C bonds and the surrounding molecules as a result of the introduction of mechanical stress. The slight peak shift in the non-visibly plastically deformed areas can also be explained by these energy-elastic like molecular changes in the para-phenylene group, without any visible plastic deformation.

By investigating a circular sample area of 4 mm, which corresponds for 30 µm thick samples to an investigated sample volume of approximately 0.38 mm^3, the recorded spectra are the average of a comparatively large volume, especially with regard to the sample dimensions and the dimensions of the shear bands. However, the peak shift $\Delta\tilde{v}_{1608}$ between the initial as-produced state and the deformed state has a value of around 0.15 cm^{-1} is still detectable and significantly greater than the device scattering of 0.02 cm^{-1} for the peak at 1608 cm^{-1}. The red-shift of the aromatic peak wavenumber $\tilde{v}_{1608}$ towards lower wavenumber values can be explained with the Badger rule (see Chapter 2.3.2 and Equation 2.16). An external stress application leads to an increase in bond distance of the aromatic C_1 and C_4 atoms and comes together with a decreasing bond force constant k which is related to the corresponding peak wavenumber (Equation 2.8). As a result of stretching of the aromatic component in the backbones, the vibrational energy for the in-plane stretching at 1608 cm^{-1} slightly change and less energy is necessary (red-shift $\Delta\tilde{v}_{1608}$).

To investigate the possible influence of temperature on load-induced peak shift $\Delta\tilde{\nu}_{1608}$, the peak wavenumber $\tilde{\nu}_{1608}$ is additionally determined before and after tensile loading of type A samples with a thickness of 50 µm at different test temperatures. In Figure 5.30 the peak shift $\Delta\tilde{\nu}_{1608}$ is shown as a function of elongation at break and test temperature. Especially when taking just the measurements in the necked sample regions account (marked as dots), the trend that an elevated test temperature T leads to an increase in elongation at break values ε and a greater peak shift $\Delta\tilde{\nu}_{1608}$, becomes obvious. At test temperatures below room temperature, the absolute peak shift $\Delta\tilde{\nu}_{1608}$ decreases compared to test temperatures above room temperature. However, the peak shift and elongation at break values scatter, so if the difference between the test temperatures is only 10 °C, the corresponding values are too close together. In addition, handling the thin, small samples is difficult and, despite all caution, the introduction of defects when clamping the sample cannot be completely ruled out, which explains the scattering.

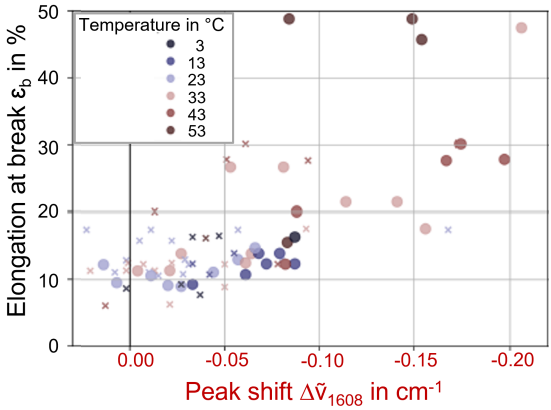

Figure 5.30: Peak Shift $\Delta\tilde{\nu}_{1608}$ is shown as a function of elongation at break and test temperature. Measurements in the necked area are marked with a dot, measurements outside the deformed area are marked with a cross. The measured sample area is a circle with a diameter of 4 mm and the recording was performed with the TENSOR II. Note that for better understanding, the abscissa runs from zero to higher negative values which corresponds to a greater red-shift $\Delta\tilde{\nu}_{1608}$.

However, $\Delta\tilde{\nu}_{1608}$ can be correlated with the corresponding test temperatures and stress-strain curves or, more precisely, with the non-uniform plastic deformation energy. For this purpose, the area under the stress-strain curves of the tensile tests is determined, which serves as a measure of the energy that is associated with the deformation process. The area under the curve can be divided into an elastic energy (E_e) and a viscoelastic and plastic energy (E_{pl}) deformation region. After elastic deformation, viscoelastic and plastic like deformation occurs throughout the entire sample ($E_{vpl,u}$), while after the necking is formed, plastic like deformation occurs more in the region of necking ($E_{pl,nu}$). This assignment of the sub-areas can be seen in Figure 5.31 (a). The area for $E_{vpl,u}$ was determined with python by using the *scipy.integrate.simps* function from 0 % to the strain that corresponds to the stress maximum (derivative = 0, dashed vertical line). The area for $E_{pl,nu}$ was calculated in the same way from the strain that corresponds to the stress maximum to the elongation at break.

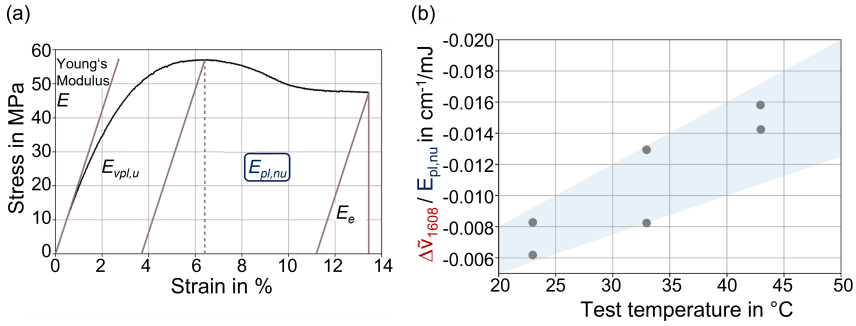

Figure 5.31: Schematic representation of a stress-strain curve including indication of the energy types for the respective section (a) and the aromatic peak shift or wavenumber $\Delta\tilde{\nu}_{1608}$ (before loading vs. after loading) related to the plastic non-uniform $E_{pl,nu}$ deformation energy as a function of the tensile test temperature for in total 6 type A samples with a thickness of 50 µm (b).

As already seen in Figure 5.30, the film samples reach higher elongation and plastic like deformation at higher temperatures. Therefore, more $E_{pl,nu}$ is recognizable at higher temperatures, even if the strength is reduced. Figure 5.31 (b) shows the ratio of the measured peak shift to the energy $E_{pl,nu}$ introduced for the different test temperatures.

Despite the relatively small number of investigated samples, the trend shows that the ratio of peak shift $\Delta\tilde{\nu}_{1608}$ (here before loading vs. after loading) to non-uniform plastic energy $E_{pl,nu}$ increases roughly linearly with temperature. This means that at a higher temperature, for the same amount of non-uniform plastic energy $E_{pl,nu}$ introduced into the deformation, the peak shift $\tilde{\nu}_{1608}$ increases more. Therefore, a significant impact of the test temperature during mechanical loading on the molecular mechanisms that occur during the plastic like deformation of epoxy can be detected. This behavior was expected since the thermal energy introduced at elevated temperatures increases the volume and molecular movement ability, and thereby molecular changes in the para-phenylene group, represented by these peak shifts, are facilitated (less yield stress is required, see Equation 2.3).

A representative deformed and creep-loaded film sample of type A with a thickness of 50 µm was investigated after mechanical creep testing (80 % UTS) at room temperature with the high spatial IR microscope because by using the HYPERION, the investigated sample volume illuminated by IR radiation is significantly reduced compared to that obtained with the TENSOR II spectrometer. This allows a higher spatial resolution, and the recorded spectra contain a low averaging of the molecular structure within the different sample regions, and a differentiation between the deformed and undeformed sample regions is improved. The measurement distance is set to 165 µm. To do so, an IR measurement without gaps in a grid was performed on a deformed sample with shear bands and the investigated sample volume for the 50 µm thick samples was only about 0.0014 mm^3. For every measurement point or pixel with a size of 165 x 165 μm^2, a spectrum was recorded. Even if it takes a long time (around 5 sec per pixel, around 10 h for the entire sample), it is possible to apply a gapless measuring grid over the entire sample area and optimize the differentiation between the deformed shear band zones and undeformed sample regions even more. The gapless grid is shown in Figure 5.32 together with the corresponding photoelastic image and the determined width-averaged peak wavenumbers $\tilde{\nu}_{1608}$ in the marked grid along the sample length, through deformed sample regions with shear bands. The measuring width is about 1 mm, so 10 pixel are positioned next to each other (each 165 µm high). From these corresponding spectra, the peak wavenumber $\tilde{\nu}_{1608}$ is extracted and the width average is determined for each length position. In the next step, the data was smoothed with a Savitzky-Golay filter.

This clearly shows that the peak wavenumber $\tilde{\nu}_{1608}$ in the deformed area with shear bands has reduced values (red-shift) compared to the less or undeformed sample regions even if the measurement lines in width direction sometime include both in different proportions.

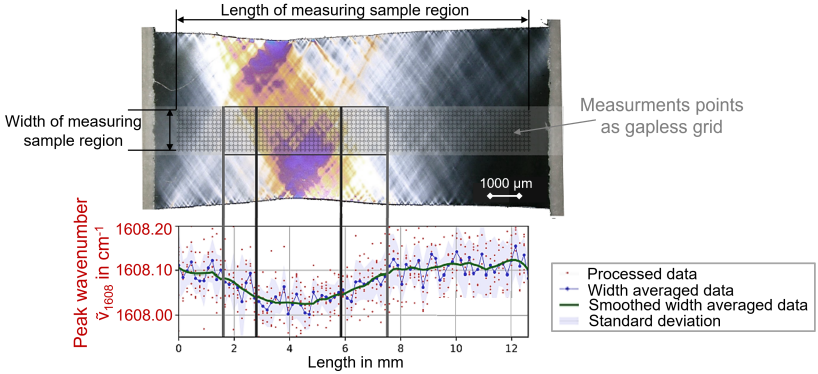

Figure 5.32: Correlation of a photoelastic image and *ex situ* IR microscope results of a creep-loaded film specimen of type A with a thickness of 50 µm at a stress level of 80 % UTS without failing during the mechanical creep loading. The gapless measuring grid is shown from which the measurement area or pixel with a size of 165 x 165 µm results. For each recorded and processed spectrum, the peak wavenumber $\tilde{\nu}_{1608}$ values were extracted and plotted as red dots in the graph. For each measurement line in width direction, the averaged peak wavenumber $\tilde{\nu}_{1608}$ values were calculated from the processed data. Afterwards the width averaged data along the length of the sample were smoothed with a Savitzky-Golay filter (5 coefficients, second degree polynomial) and the standard deviation was determined and plotted as well. After it was done this way, in the shear bands a red-shift at the *para*-phenylene group specific wavenumber $\tilde{\nu}_{1608}$ could be confirmed also for the creep loaded films.

Other representative creep-loaded and deformed type A film samples with a thickness of 30 µm were investigated after mechanical testing with the IR microscope. For every measured spectrum (in a squared sample region with a size of 165 x 165 µm^2), the aromatic peak wavenumber $\tilde{\nu}_{1608}$ at 1608 cm^{-1} was extracted. Regarding the wavenumber value of $\tilde{\nu}_{1608}$, each measurement point or pixel got a defined color of a continuous color scale. This creates an aromatic peak wavenumber visualization for the entire deformed sample and can be seen in Figure 5.33.

The sample regions with reduced aromatic peak wavenumbers, i.e., the regions with a more pronounced (red) peak shift, are colored in dark red. The peak wavenumbers in the optically non-deformed area are higher in comparison to the shear band regions.

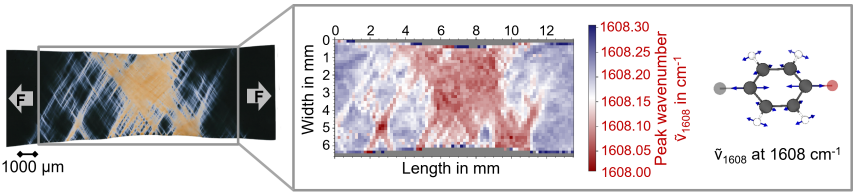

Figure 5.33: Correlation of a photoelastic image and *ex situ* IR microscope results of a creep-loaded film specimen of type A with a thickness of 30 µm at a stress level of 80 % UTS without failing during the mechanical creep loading (maximum elongation of 17 %). The corresponding creep curve is shown in Figure 5.13. Each pixel with a size of 165 x 165 µm is a measurement point and correspond to a spectrum. All recorded spectra are evaluated regarding the aromatic peak wavenumber $\tilde{v}_{1608}$. Depending on the value of $\tilde{v}_{1608}$, each pixel is colored.

The peak wavenumbers $\tilde{v}_{1581}$, $\tilde{v}_{1362}$, $\tilde{v}_{1182}$ and $\tilde{v}_{829}$ of this sample were also investigated, as can be seen in the Appendix in Figure 16. A correlation of shear bands and peak wavenumber values is not feasible for all mentioned peaks. The reason why not all peaks can be analyzed and correlated is the high absorbance, which is challenging to evaluate through peak fitting. In addition to the aromatic wavenumber $\tilde{v}_{1608}$ the peak $\tilde{v}_{1362}$ can be unambiguously correlated with the shear bands. The peak at 1362 cm^{-1} corresponds to the C-H bending of CH_3 (see Table 5.4) and indicates a blue-shift towards higher peak wavenumbers. This might indicate a decreasing distance between the backbones since the intermolecular forces are strongly distance dependent. The blue-shift can be explained as well by the Badger rule (Equation 2.16) with an increasing bond force constant k. Even the data visualization for the other aromatic peak $\tilde{v}_{1581}$ in Figure 16 scatters more, a load-induced red-shift can be seen which was expected since the peak corresponds also to an aromatic vibration (see Table 5.4) and can be explained in the same way as the aromatic red-shift $\Delta\tilde{v}_{1608}$.

Figure 5.34 shows the aromatic peak shift values $\Delta\tilde{v}_{1608}$ which were calculated from the difference between averaged initial wavenumber (as-produced state) and feature extracted wavenumber after creep loading (70 % UTS) for a type A sample with a thickness of 30 µm. It is unambiguous, that an aromatic peak red-shift towards lower wavenumbers compared to the initial sample state, can be detected only in deformed regions with shear bands. In the optical non-deformed sample region (black colored regions in the photoelastic image) the aromatic peak wavenumber $\tilde{v}_{1608}$ is close to the initial value and the $\Delta\tilde{v}_{1608}$ is approximately zero (lighter pixels).

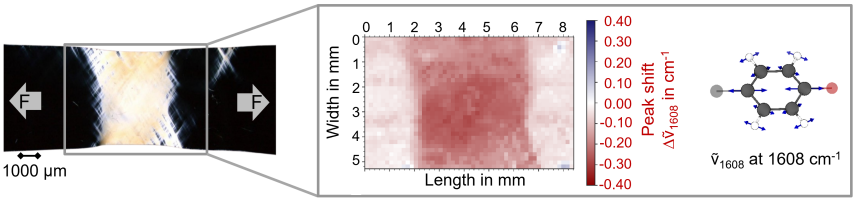

Figure 5.34: Correlation of a photoelastic image and *ex situ* IR microscope results of a creep-loaded film specimen of type A with a thickness of 30 µm at a stress level of 70 % UTS without failing during the mechanical creep loading (maximum elongation of 17 %). Each pixel with a size of 165 x 165 µm is a measurement point and correspond to a spectrum. All recorded spectra are evaluated regarding the aromatic peak shift $\Delta\tilde{v}_{1608}$. Depending on the sign and value of $\Delta\tilde{v}_{1608}$, each pixel is colored.

This validates the conclusion that shear bands contain stretched backbones with increased aromatic C_1-C_4 bond lengths and possibly changed bond angles as well compared to the energetic equilibrium state before mechanical loading and deformation. With project-related atomistic simulations it was possible to detect an increase in the bond length between the aromatic atoms C_1 and C_4 in epoxy due to tensile stress [211]. This is in line with the Badger rule already presented (see Equation 2.16). Since the *ex situ* IR measurements were performed after load or stress relief, elastic recovery had already taken place. Therefore, the detected peak shift $\Delta\tilde{v}_{1608}$ is related to a remaining change in the bond lengths or angles and not to a spontaneous energy elastic change (see Chapter 2.1). This means that the aromatic structure in the backbones is stress-sensitive and is directly related to the plastic like shear band formation. The therm *energy-related deformation* is used therefore in the following.

In the literature, Raman and IR peak shifts are detected for different materials, e.g. polyethylene or polypropylene, and are attributed to a variation of bond lengths and bond angles according to the Badger rule [10, 177, 212] or a change in the molecular environment [213, 214]. Even if the *para*-phenylene group is a particularly rigid and strongly bonded component in the backbone due to the delocalized π-electron system, an increase of the bond lengths in the aromatic structure could be detected with project-related MD simulations [211]. This MD simulations also investigated an increase in the interaction between aromatic compounds by their corresponding π-electrons, the so-called π-π-interaction, as this has been found to occur at a corresponding distance between the aromatic rings [214, 215]. Aromatic rings have large planar surfaces, and a stacked arrangement due to π-π interactions would increase the van der Waals contacts [216]. So, if aromatic rings are subjected to load-induced stretching, distance and position changes due to untwisting and unraveling of entanglements and bond lengthening, the result could be a changed non-covalent interaction and a modified molecular environment [217, 218], which could affect the required vibration energy or the peak wavenumber (see 2.3.1) as well. However, this hypothesis could not be supported by the project-related MD simulations [211]. No increase in π-π-interaction of the stretched aromatic rings could be demonstrated due to the tensile loading of epoxy materials.

Quality of peak shift evaluation

To analyze the impact of different model approximations on the extraction of the peak wavenumber $\tilde{\nu}_{1608}$ of microscopic IR data and the resulting load-induced peak shift $\Delta\tilde{\nu}_{1608}$, the Gaussian fit for this peak is exemplary compared with the Lorentzian and Voigt fits. Figure 5.35 pictured the processed or interpolated data and the three different fits of the recorded spectra from a creep-tested type A sample with a thickness of 30 µm (the corresponding photoelastic image is shown in Figure 5.33). Two different sample positions are investigated, an undeformed (a) sample region and a deformed (b) sample region with shear bands. From this, the Gaussian peak shift determined by feature extraction $\Delta\tilde{\nu}_{1608}$ can be determined and is about $-0.225\,\mathrm{cm}^{-1}$. For a Lorentzian fit $\Delta\tilde{\nu}_{1608}$ is about $-0.235\,\mathrm{cm}^{-1}$ and with a Voigt fit, the aromatic peak shift results in $-0.232\,\mathrm{cm}^{-1}$. The differences are negligible, hence only Gaussian was used for the feature extraction in the following thesis.

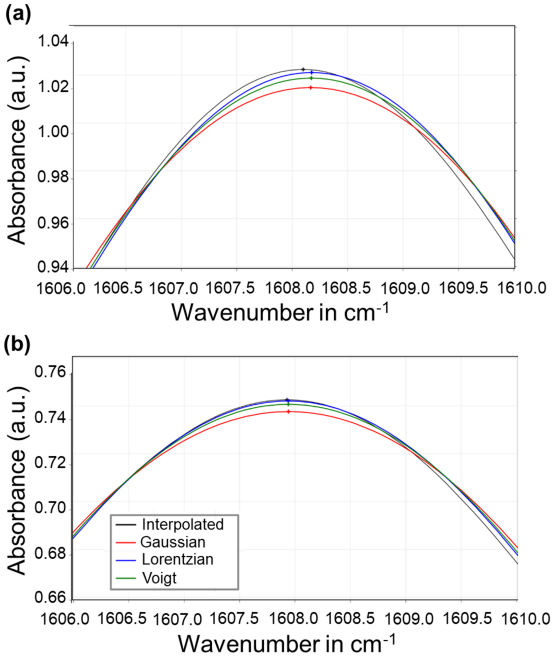

Figure 5.35: Peak fit for an *ex situ* IR measurement in the undeformed sample region (a) and in the deformed sample region (b) of a type A sample with a thickness of 30 µm.

As another analysis method for the detection of peak shifts, the Šturcová approach was presented in Chapter 4.4 as this method is often used for peak shift detection. Here, the difference spectrum is calculated from the initial state spectrum and the spectrum after loading. In the next step the difference spectrum is integrated and divided by the initial spectrum. To do so, the peak shift for a corresponding peak wavenumber can be determined. This is shown in Figure 5.36 for the peak at 1608 cm^{-1}. The peak shift $\Delta\tilde{\nu}_{1608}$ determined with the Šturcová method is about $-0.21\,\mathrm{cm}^{-1}$. This is also shown in Figure 5.37 in comparison to the Gaussian approach.

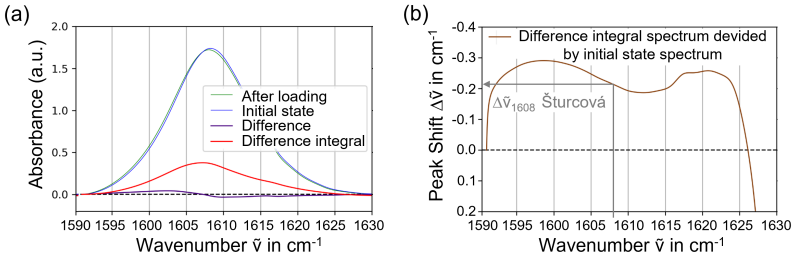

Figure 5.36: The peak shift determination $\Delta\tilde{v}_{1608}$ with the Šturcová approach [10] is shown. First the difference spectrum is calculated from the initial state spectrum and the spectrum after loading. Afterwards the resulting difference spectrum is integrated. This can be seen in (a) The integrated difference spectrum is divided by the initial state spectrum. The peak shift for a specific wavenumber can be extracted as shown exemplarily for the peak at 1608 cm^{-1} (b).

For this investigated type A film sample with a thickness of 30 µm, the Gaussian approach results in a comparatively slightly smaller peak shift $\Delta\tilde{v}_{1608}$, but both values are in the same order of magnitude. Nevertheless, the following thesis focuses on one method, the gaussian fit approach. The reason is, that, the reproducibility of the Šturcová approach depends mainly on the normalization process and is not recommended for samples that change thickness under load [10]. Since the peak area PA and the absorbance A for all investigated peaks are reduced in the deformed sample regions with shear bands compared to the undeformed sample regions (see Appendix Figure 17-21) and microscopic investigation indicate a reduction in the thickness in the shear bands (see Figure 5.17), the Šturcová approach is not as suitable for epoxy film samples with necked regions as the thickness independent Gaussian approach.

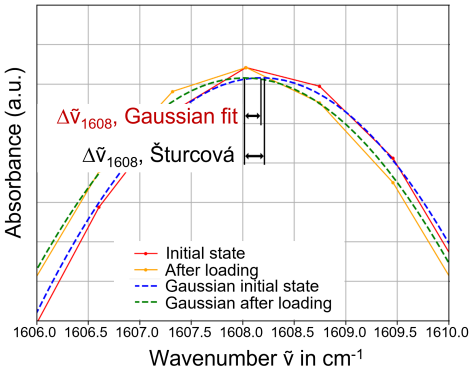

Figure 5.37: The peak shift $\Delta\tilde{v}_{1608}$ determined with the Šturcová method is compared with the Gaussian peak shift at a wavenumber of 1608 cm^{-1}.

The goodness of the Gaussian peak fitting can be investigated by determining the χ^2 values (see Chapter 4.4). The value χ^2 indicates whether the calculated model is coming into convergence with the actual peak and indicates how well the particular model matches the peaks in a measured spectrum. Figure 5.38 shows the χ^2 values determined for a Gaussian fit to the peak at 1608 cm^{-1} for a creep-loaded (70 % UTS) type A sample with a thickness of 30 µm. The corresponding photoelastic image and the visualization of the IR microscope data are shown in Figure 5.34. For each recorded spectrum of a sample size of 165 x 165 $µm^2$, the peak at 1608 cm^{-1} was investigated with respect to the goodness of fit. The pictured histogram shows the total counts of specific χ^2 values in the investigated sample region. A perfect convergence between the modeled and recorded peak is achieved when χ^2 is equal to zero [146]. Most χ^2 values are below 0.3, indicating a convenient fit for the Gaussian model and validating the peak fitting approach.

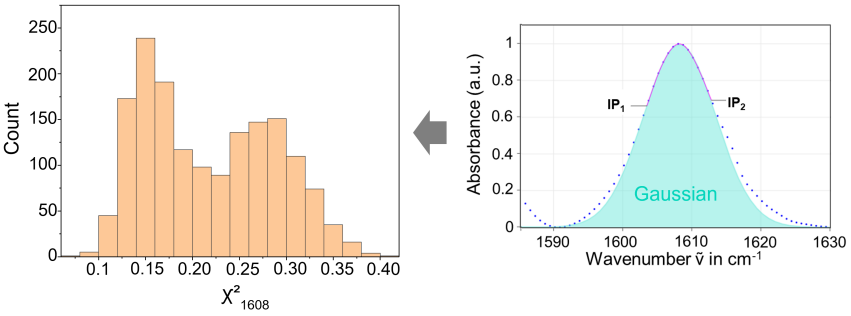

Figure 5.38: Using an IR microscope recorded spectra from a creep loaded type A sample with a thickness 30 µm is investigated regarding the peak at 1608 cm^{-1}. The baseline corrected, normalized and interpolated peak is compared to the Gaussian fitted peak and the χ^2 values are determined for each spectra. The histogram pictured the count of a specific χ^2 which appears in the investigated sample region (see Figure 5.34).

Further spectral evaluation

The recorded IR microscope data of the creep-deformed sample presented (see Figure 5.33) was further analyzed using the Gaussian peak fitting approach. Every processed spectra of a pixel is analyzed in terms of the absorbance (A_{1608}), peak area (PA_{1608}), asymmetry factor (ASF_{1608}) and *Full Width at Half Maximum* ($FWHM_{1608}$) of the aromatic vibration, as can be seen in the Appendix in Figure 21. It is obvious that the absorbance (A_{1608}) and peak area (PA_{1608}) have lower values in the shear bands compared to visually non-deformed sample regions. This is also visible for other epoxy peaks in the *ex situ* and *in situ* IR analysis (see Appendix Figure 17-20 and 22) since the reason might be the reduction of thickness in the deformed sample regions with shear bands (Beer's law, see Equation 2.12) as indicated by the laser scanning microscope and µ-CT investigations (see Figure 5.17 and 5.18). Therefore, these effects are not directly caused by load-induced molecular mechanisms. The values of $FWHM_{1608}$ and ASF_{1608} increase in the shear bands compared to the visually undeformed sample regions. This might be caused by an uneven stress distribution in the aromatic rings and backbones since a peak broadening is related to a non-uniform stress distribution of the corresponding bonds since the bond distance R and force constant k depend on the experienced stress [24].

Even if it is not as clear as for the peak at $1608\,\mathrm{cm}^{-1}$, this is also visible for another aromatic vibration at a wavenumber of $1581\,\mathrm{cm}^{-1}$ (see Appendix Figure 20).

By reduction of the film thickness to 15 µm, the absorbance of some other vibrational modes decreases according to Beer's law, and by doing so some further peaks or vibrational modes can be evaluated. In Figure 5.39 the photoelastic image and the IR microscope results (same settings and pre-processing) of a deformed epoxy film sample with a thickness of 15 µm can be seen. In addition to the aromatic peak wavenumber values at $1608\,\mathrm{cm}^{-1}$, each pixel is colored with respect to the peak shift of the peak wavenumber at $829\,\mathrm{cm}^{-1}$. To assure the comparability of both peak shifts, the difference of the peak wavenumber of the specimen in relation to the averaged peak wavenumber of unloaded specimens (initial state) is plotted and colored regarding the direction of peak shift. The peak at $829\,\mathrm{cm}^{-1}$ corresponds to an out-of-plane vibration of the aromatic hydrogen atoms $\tilde{v}_{829}$ [196, 197] and slightly shifts in the other direction towards higher wavenumbers in the shear band regions, a so-called blue-shift. The absolute peak wavenumber values $\tilde{v}_{829}$ and $\tilde{v}_{1608}$ for a creep-loaded type A sample with a thickness of 15 µm can be seen in the Appendix in Figure 23.

In the Appendix in Figure 24 - 27 the recorded IR microscope data of a 15 µm thick creep-deformed sample was also further analyzed using the Gaussian peak fitting approach. The peak $\tilde{v}_{1362}$ indicates a blue-shift in the shear band regions, which is in line with the previous discussed results for 30 µm thick creep-deformed samples (see Appendix Figure 16). The asymmetry factor of this peak ASF_{1362} in the shear band regions is larger than 1 which indicates that the right peak side of the peak at $1362\,\mathrm{cm}^{-1}$ for the 15 µm thick creep-loaded sample is wide after mechanical load application. This might be due to uneven stress distribution and could not be detected for thicker samples with a thickness of 30 µm because of the high absorbance (see Appendix Figure 19).

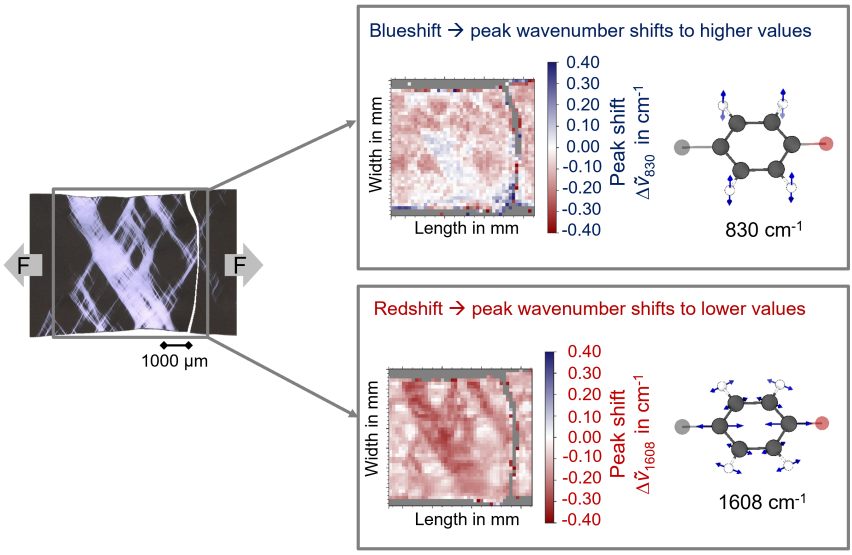

Figure 5.39: Correlation of a photoelastic image and *ex situ* IR microscope results of a representative type A loaded film specimen with a thickness of 15 µm. Each pixel with a size of 165 x 165 µm is a measurement point and correspond to a spectrum. All recorded spectra are evaluated regarding the aromatic peak wavenumber $\tilde{\nu}_{1608}$ and $\tilde{\nu}_{829}$. Depending on the values of the peak shifts $\Delta\tilde{\nu}_{1608}$ and $\Delta\tilde{\nu}_{829}$, each pixel is colored. Blue colored pixels correspond to a peak shift towards higher peak wavenumbers and red pixels show a decreased peak wavenumber compared to the initial peak wavenumber.

The absolute peak shift $\Delta\tilde{\nu}_{829}$ is smaller than the peak shift $\Delta\tilde{\nu}_{1608}$. This was expected since the aromatic C-H bonds are not integral to the main chain that directly experiences the applied load, the resulting peak shift is correspondingly less pronounced. However, it can be seen that the peak $\Delta\tilde{\nu}_{829}$ slightly shifts to higher wavenumbers in the shear band regions of the deformed specimen. The C–H bonds in the aromatic rings are assumed to be associated with more general van der Waals interactions and contribute to the load-bearing capacity of the polymer [159]. The van der Waals interactions are highly distance dependent and a small variation of the distance may already lead to significantly higher load-bearing capacity connected with higher wavenumbers for vibration of the corresponding C-H bonds [219].

The peak wavenumber at $829\,\mathrm{cm}^{-1}$ is assumed to be not only related to the distance between the backbones but may also be used as an indication of the intensity of the intermolecular forces, as shown in the study of Doblies et al. [159]. The deformation is maximal in the shear bands, as the absorbance of every peak significantly decreases there because of the reduced sample thickness resulting from the deformation process (Beer's law). This led to an increase in peak wavenumber of aromatic hydrogen bonds at $829\,\mathrm{cm}^{-1}$ due to a significant reduction in the distances between the polymeric backbones and a changed polarization. The conceivable aromatic and hydrogen bond interactions might further intensify this effect. However, project-related MD simulations have not observed a decrease in distance between polymer chains or an increase in π-π interactions between the deformation of aromatic compounds [211]. Another hypothesis for the blue-shift $\Delta\tilde{\nu}_{829}$ is, that the stretching of the aromatic rings leads to changed electron orbitals, thereby altering the vibrational energy of the aromatic hydrogen atoms. The blue-shift of the C-H vibration is thus most likely not correlated with bond length changes, suggesting an alternative mechanism. Analysis of Mulliken charges from quantum mechanical computations indicates that increased positive polarization of the aromatic hydrogen atoms in stretched aromatic rings leads to higher peak wavenumber, causing the observed blue-shift. The related atomistic simulations performed from Dr. Julian Konrad (Institute of soft matter modeling, TUHH) can be found in [211].

The spectrum of an as-produced type A HBPA-DGE film sample with a thickness of 30 µm and a spectrum after tensile test recorded in the deformed sample regions of the same sample are shown in the Appendix in Figure 28. The spectrum only contains a few well-dissolved peaks, as this epoxy resin system chemically contains only a few different molecular groups (see Figure 3.3). The requirements for a comprehensive spectral analysis, such as peak shifts, are therefore not fulfilled, which is why no further IR analysis of the HBPA-DGE samples is carried out regarding load-induced spectral changes in the context of this thesis. However, even without extensive data processing (only baseline correction), it can be seen that the absorbance of all peaks after the tensile test is lower than in the as-produced sample state because of the deformation. This is caused by the reduced sample thickness in the deformed regions and can be explained as well by Beer's law.

5.3.2 In situ Infrared spectroscopy

To analyze the molecular mechanisms of the para-phenylene group $\tilde{v}_{1608}$ at $1608\,\mathrm{cm}^{-1}$ during mechanical loading, the peak wavenumber is extracted from the pre-processed spectra and tracked during a mechanical experiment, i.e. *in situ* (see Figure 4.4). When comparing the mechanical data and the corresponding peak wavenumber $\tilde{v}_{1608}$ of a 30 µm thick film samples recorded during mechanical loading, it is noticeable that the peak wavenumber $\tilde{v}_{1608}$ of the aromatic C-C stretching can be *in situ* correlated with the mechanical deformation of the epoxy resin film. Figure 5.40 (a) shows the tracked aromatic peak wavenumber during creep testing for a 30 µm thick type A film sample at a stress level of 56 MPa (80 % UTS). For the elastic stretching that occurs in the first creep phase, a pronounced shift towards lower aromatic peak wavenumbers $\tilde{v}_{1608}$ can be found as well during the *in situ* measurements. In the second creep phase, with an almost constant strain, only a comparably small aromatic peak shift is observed. In the third creep phase, the aromatic peak wavenumber $\tilde{v}_{1608}$ decreases again sharply as a result of increased macrosopic material stretching. The strain during creep testing shown in Fig. 5.40 (b) shows that the peak wavenumber $\tilde{v}_{1608}$ of the aromatic $\tilde{v}_{1608}$ stretching can be directly and linearly correlated with the mechanical deformation or the creep strain of the epoxy resin film.

Similarly, in relaxation and cyclic mechanical experiments, the aromatic peak wavenumber can be tracked as shown in Figure 5.40 (c), (d) and (e). In the relaxation experiment, there was a steep decrease in $\tilde{v}_{1608}$ at the beginning of the experiment as the epoxy was stretched towards a set elongation of 4 %. Subsequently, a small increase in the aromatic wavenumber was detected during the further duration of a test (see Figure 5.40 (c)). The stretched molecular backbones with the aromatic *para*-phenylene groups can slowly relax over time and come close to the unloaded position of the $\tilde{v}_{1608}$ peak, i.e., an energetic and entropic more favored state of equilibrium before the macroscopic sample stretched up to an elongation above the yield stress. The molecular relaxation processes are comparatively slow at room temperature, and therefore the increase of $\tilde{v}_{1608}$ is only low. Cyclic loading experiments show clearly visible an overall decrease in $\tilde{v}_{1608}$ after mechanical loading and, to some extent, no full recovery of the aromatic peak wavenumber $\tilde{v}_{1608}$ to the initial wavenumber after unloading occurs due to the fact that not only elastic deformation takes place, but also viscoelastic processes (see Chapter 2.1).

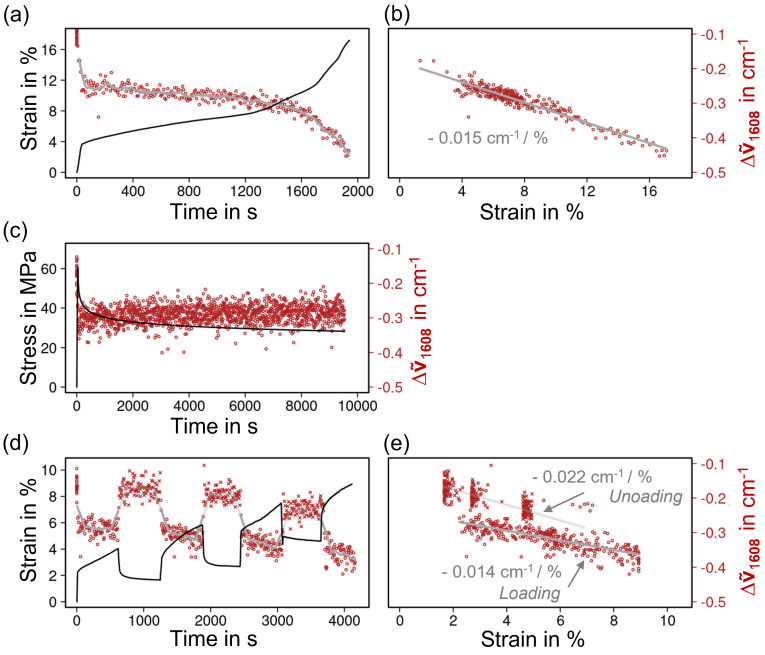

Figure 5.40: *In situ* tracked aromatic peak wavenumber $\tilde{v}_{1608}$ (each red dot represent a recorded and processed spectrum) over the time (fitted curve in gray) for type B film specimens with a thickness of 30 µm during creep (80 % UTS) (a) and (b), relaxation (4 % strain) (c) and cyclic (σ_{max} = 70 % UTS) loading (d). The corresponding mechanical data is plotted as a black line. The aromatic peak wavenumber $\tilde{v}_{1608}$ is correlated with the creep strain in (b) and with the cyclic strain in (e) together with linear regression lines (gray) and the corresponding determined slope.

The elastic behavior of epoxy is characterized by reversible and spontaneous changes in bond length and molecular angles and can be quantified by observing a red-shift of stretched bonds during the initial phase of mechanical loading (see Figure 5.40 (a) and (d)). In contrast, viscoelastic and plastic or viscous deformations involve additional, time-dependent, and irreversible phenomena, such as bond lengthening, untwisting, unraveling of entanglements, and positional changes of molecular chains within the network. This is evident in Figure 5.40 (d). During cyclic testing, the peak wavenumber does not return completely to its initial value during the unloading cycle because there is not enough time for complete relaxation.

Consequently, the material does not fully revert to its previous strain state. This behavior is also reflected in the slope of the linear fit during unloading (crosses), which is approximately $-0.022\,\mathrm{cm}^{-1}/\%$ as shown in Figure 5.40 (e). A linear fit of the strain versus wavenumber during the loading cycle is also presented. The slope of the loading cycle is approximately $-0.014\,\mathrm{cm}^{-1}/\%$, which is comparable to the slope observed in the linear fit for creep loading, as shown in Figure 5.40 (b).

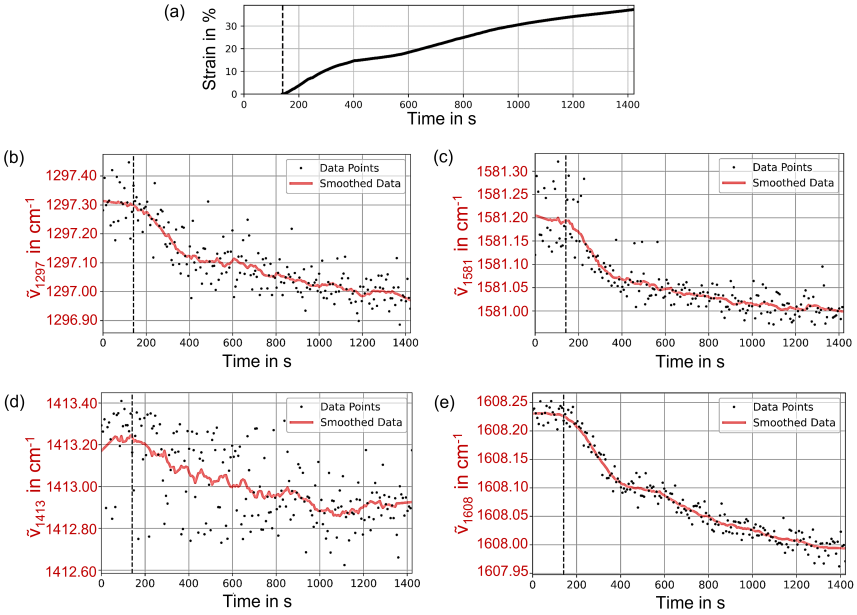

Figure 5.41: *In situ* tracked peak wavenumber $\tilde{\nu}_{1297}$ (b), $\tilde{\nu}_{1581}$ (c), $\tilde{\nu}_{1413}$ (d) and $\tilde{\nu}_{1608}$ (e) (each dot represent a recorded and processed spectrum) over the time (smoothed curve in red) for a type B film specimen with a thickness of 15 µm during creep loading (70 % UTS). The corresponding mechanical data is plotted in (a).

As already mentioned, for films with a comparatively reduced thickness of 15 µm even more peaks, corresponding to other wavenumbers or vibration modes can be recorded, pre-processed and tracked during mechanical loading. For a creep-loaded type B film sample with a thickness of 15 µm the creep curve is shown in Figure 5.41 (a).

In addition to the development of $\tilde{v}_{1608}$ during the creep test (e), the development of $\tilde{v}_{1295}$, $\tilde{v}_{1415}$ and $\tilde{v}_{1581}$ is plotted from the recorded and pre-processed spectra during the creep test as well. Due to the double shape of the peak $\tilde{v}_{1415}$ at $1415\,\mathrm{cm}^{-1}$ (see Figure 5.26) and the challenging feature extraction, the scattering is significantly higher for this peak. However, all investigated peaks exhibit a red-shift towards lower peak wavenumber values due to the creep loading. The peaks $\tilde{v}_{1415}$ and $\tilde{v}_{1581}$ are also related to the *para* -phenylene groups. The vibration at $1298\,\mathrm{cm}^{-1}$ is related to the (tertiary) amines (see Table 5.4) which can be related to the cross-linking points. This confirms once again that the backbones and molecular chain segments are stretched between the cross-linking points.

Intermediate summary

It was possible to show that *ex situ* and *in situ* IR spectral changes can be directly correlated with macroscopic mechanical deformation and shear band formation. This means that molecular processes can be detected both under load and after final failure. This also rules out the possibility that these are spontaneous, reversible rearrangement processes under load. The IR spectroscopic results confirmed the following research hypotheses:

3. *Vibrational spectroscopic analysis can be performed to correlate the molecular mechanisms within epoxy with the macroscopic mechanical behavior.*

4. *The ductility in epoxy is enabled by molecular rearrangement processes in the cross-linked network.*

5.3.3 Polarized Infrared spectroscopy

If the spectrum of an oriented sample is measured with polarized radiation, its dipole moment derivative must have a non-zero component in the direction of the polarization if that peak is to be seen in the IR spectrum [146] (see Chapter 2.3.1). This had been done, for example, on PET bottles [220]. In Figure 5.42 (a) the polarized IR spectra of a creep loaded type A sample with a thickness of 30 µm for different polarization directions with respect to the load direction (0°) are shown together with the corresponding photoelastic image and the investigated circular sample region (b).

Figure 5.42 (c) shows the peak absorbance A_{1608} dependent on the direction of polarization (10 spectra were recorded and averaged). The absorbance A_{1608} is highest in the load direction, and the difference with respect to the other polarization direction, especially to 90° (perpendicular to the load direction) is significant. This indicates that the molecular backbones with the aromatic *para*-phenylene groups are not only stretched (red-shift), but also aligned in the load direction. This may also be a necessary requirement for detectable molecular stretching of the aromatic carbon atoms within the molecular backbones. To fully capture the external load and to experience bond stretchings within the backbone, the backbones should be oriented in load direction, at least a sufficient amount of backbones.

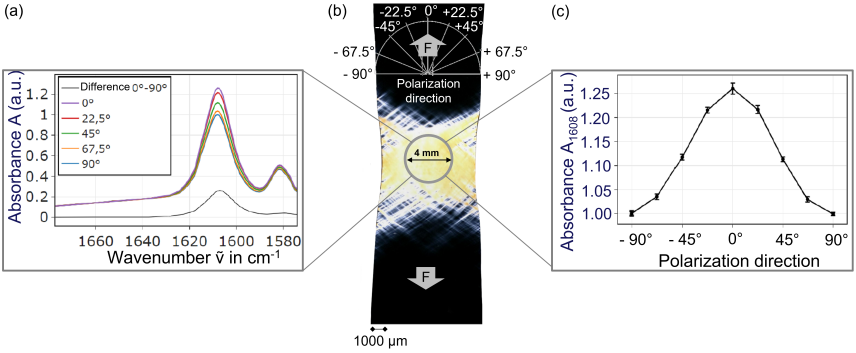

Figure 5.42: Photoelastic image of a creep-loaded type A sample with a thickness of 30 µm (b). After the creep test at a load level of 80 % UTS and an elongation until 17 %, polarized IR spectra were recorded at the circular marked highly deformed sample region with the TENSOR II spectrometer. The polarization direction or angle was changed with regard to the load direction (0°). 10 spectra were recorded and averaged. The averaged spectra around the aromatic peak at 1608 cm^{-1} for different adjusted polarization directions or angles are shown in (a). For each polarization direction, the processed and averaged spectrum was analyzed with regard to the peak absorbance A_{1608} of the aromatic peak at 1608 cm^{-1} and can be seen in (c).

Using an IR microscope with a polarizer, the entire sample can be investigated regarding molecular orientations and differences between the visually undeformed and deformed sample areas can be detected. The results of the polarized IR microscope data is shown in Figure 5.43.

The determined polarized peak absorbance values A_{1608} and A_{830} are used to calculate the molecular orientation factor f (see Equation 4.7) for each spectra or pixel. Note that the factor f runs from 0 to 1, corresponding respectively from random to perfect alignments parallel to the tensile direction (0°), but could take a negative value if the backbone has preferred orientation in the transverse direction (90°). Each pixel is colored with respect to the value and sign of the factor f. It can be seen that the in-plane vibration of the aromatic *para*-phenylene groups is oriented in the load direction, but only in the deformed sample region with shear bands. The out-of-plane aromatic C-H vibration at 830 cm^{-1} shows a slight negative molecular orientation factor in the corresponding deformed sample region. This allows the conclusion that, as a result of the backbone alignment with the aromatic structure in the load direction, the aromatic C-H bonds are aligned perpendicularly, which is additionally validation of the molecular backbone orientation in the load direction.

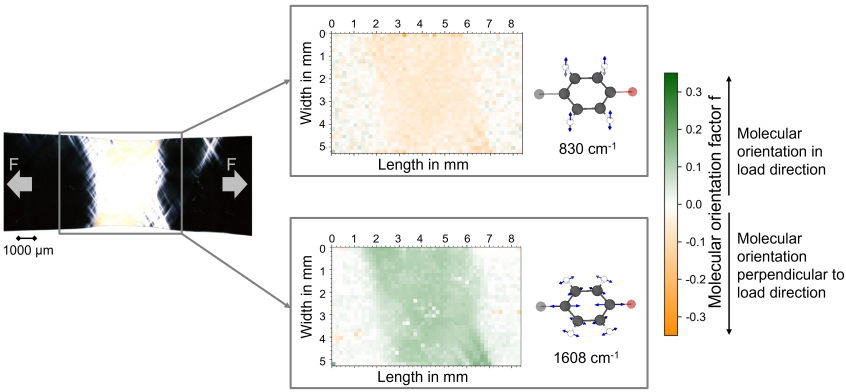

Figure 5.43: Photoelastic image of a creep-loaded type A sample with a thickness of 30 µm. After the creep test at a load level of 70 % UTS and an elongation until 17 %, images were taken of the marked and deformed sample region using HYPERION microscope and a pixel size of 165 x 165 $µm^2$. The polarization direction or angle was set to 0° (in load direction) and 90° (perpendicular to load direction). For each recorded spectra in 0° and 90°, the processed spectra were analyzed with regard to the absorbance A_{1608} and A_{830} of the aromatic peaks at 1608 cm^{-1} and 830 cm^{-1}. The corresponding vibrations are schematically visualized. With the feature extracted peak absorbance values and Equation 4.7, the molecular orientation factor f was calculated and colored for each recorded spectra and both peaks. In the shear bands the in-plane vibrations of the aromatic para-phenylene groups are oriented in the load direction and the out-of-plane aromatic C-H vibrations at 830 cm^{-1} are aligned perpendicularly.

The polarized IR results are in line with the strain softening and hardening effects detected in the tensile tests (see Figure 5.11). At a molecular level, the entanglements unravel first and the backbones are aligned in a load direction. Without significant stress concentrations and early failure, the aligned molecular backbones are further stretched by applying further external load to the material, which explains the further presented red-shift $\Delta\tilde{v}_{1608}$.

5.4 Polarized Raman spectroscopy

The polarized Raman spectra of the initial or as-produced epoxy film type A samples with a thickness of 30 µm in the polarization mode 0° and 90° are shown in Figure 5.44. A polarization-dependent intensity cannot be detected, which means that no molecular orientation is evident from the film manufacturing process.

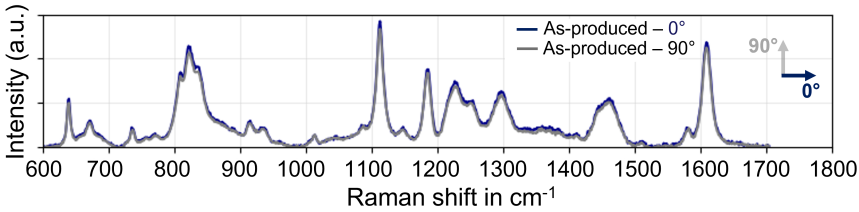

Figure 5.44: Raman spectra of an as-produced epoxy film sample type A with a thickness of 30 µm in 0° and 90° polarization mode.

This is in line with the mechanical data of the transverse and longitudinal samples and with the polarized IR investigation of as-produced samples. Between the 0° and 90° spectra of the undeformed sample regions of a loaded epoxy film sample, there is also no significant difference.

The Raman peak wavenumbers are listed in Table 5.5 together with the corresponding molecule vibration modes. It should be pointed out that the literature often only gives ranges for the peak wavenumbers or Raman shifts, since the exact peak wavenumber always depends on how the respective molecule is bound to other molecules and which substitutes are present, as is the case for IR peaks as well. In addition, superpositions often occur, i.e. different molecules vibrate at the same wavenumbers.

This can lead to different ways of characterizing the vibrations of molecules in the literature. For this reason, this table should not be interpreted as comprehensive, but rather is provided as a guideline. The wavenumbers $\tilde{v}$ of the individual Raman peaks are mentioned in Figure 5.26.

Table 5.5: List of Raman shifts or peak wavenumbers $\tilde{v}_{Peak}$ of epoxy film samples with the corresponding molecule vibration modes. The information is taken from the literature [5, 137, 138, 196, 197, 201, 221]

Peak wavenumber $\tilde{v}_{Peak}$ in cm^{-1}	**Molecule vibration modes**
635	In-plane quadrant stretching of *para*-phenylene
821	Symmetric stretching of aliphatic ether and symmetric stretching of secondary alcohol
915	Symmetric stretching of the epoxy rings
932	Symmetric stretching of the epoxy rings
1105	Asymmetric stretching of the secondary alcohol and aromatic vibration
1185	In-plane CC stretching of *gem*-dimethyl-groups between *para*-phenylene
1225	Stretching of ether bond and aromatic vibration
1250	Stretching of epoxy rings
1295	In-phase twist of CH_2 along alkane
1455	Different CH_2 and CH_3 vibrations
1580	Asymmetric in-plane quadrant stretching of *para*-phenylene
1605	Symmetric in-plane quadrant stretching of *para*-phenylene

To visualize the differences between the deformed and undeformed regions of the samples of type C in more detail, a mapping was performed in the 0° and 90° polarization modes. Afterward, a cluster analysis was applied with the WiRe software to identify repeating patterns in the recorded spectra. In Figure 5.45 it is clearly visible that the 0° polarized spectra differ between the two regions, that is, deformed (left) and undeformed (right). This is highlighted with two different colors (blue and cyan). Each color represents almost similar spectra for the corresponding measurement points. These results show that the 0° spectra change in the transition zone from a deformed to an undeformed region. Since the Raman method does not depend on the sample thickness like Infrared spectroscopy, the reduction of the thickness can be excluded as the cause of the spectral differences.

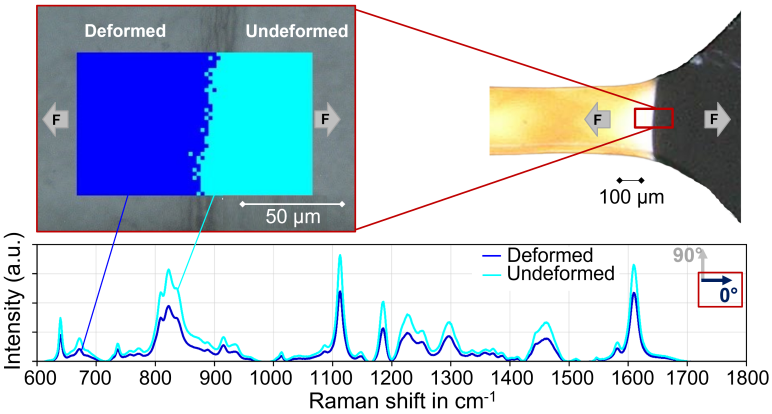

Figure 5.45: Mapping and k means cluster analysis in 0° polarization mode over the interface between the deformed (left) and undeformed region (right) of a type C sample as shown in the corresponding photoelastic image (right). The sample was stretched until an elongation at break $\epsilon_b = 73\,\%$. The cluster analysis was performed using the Renishaw Wire software. The initialization was chosen as random and the clustering type was k-means, using correlation as the distance metric. The initial number of clusters was chosen as five, but based on the similarity within the spectra of the identified clusters in different regions, the final number was reduced to two. Each pixel represents one measurement point. All blue pixels (deformed) and all cyan pixels (undeformed) have similar spectra. The averaged spectra of both regions in 0° polarization mode are shown below.

Further Raman analysis show that the polarized spectra recorded after the tensile test exhibit increased intensities of the 0° polarization mode (in tensile direction) in the necked and deformed sample regions. At the same measuring positions, comparably lower intensities were detected for the polarization mode 90° (perpendicular to the tensile direction) for most peaks, as can be seen in Figure 5.46. This is especially evident for molecular components of a backbone, such as for the different aromatic vibration modes (peaks at 1605, 1580, 1105 and 821 cm^{-1}) [221, 222], which exhibit a significantly increased intensity for the 0° polarization in the load direction.

Although normalization is generally applied when comparing spectra, this was deliberately omitted here in order to show the differences for all peaks at the same sample positions. Data processing was therefore carried out exclusively as described in Chapter 4.6 without normalization steps.

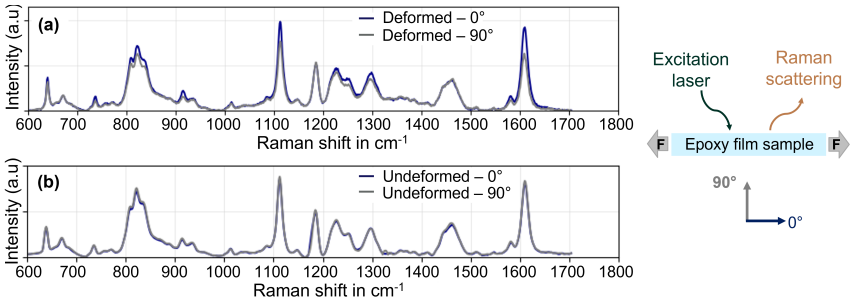

Figure 5.46: Polarized Raman spectra of a necked epoxy film sample region of type C with and without shear band regions (deformed in (a) and undeformed in (b)) for two different polarization modes (0° and 90°). The polarization is shown with regard to the tensile direction.

A suitable method to demonstrate molecular orientation is to determine the molecular orientation factor f for each peak (see Chapter 4.6 and Equation 4.8). This was done for all peaks and is shown as box plot in Figure 5.47. The peaks corresponding to backbone segments exhibit a positive value for the molecular orientation factor, which means an orientation of the corresponding molecular segments in load direction. Only the peaks at 1455 cm^{-1} and 1185 cm^{-1} exhibit a negative molecular orientation factor. This corresponds to an alignment perpendicular to the tensile direction (90°).

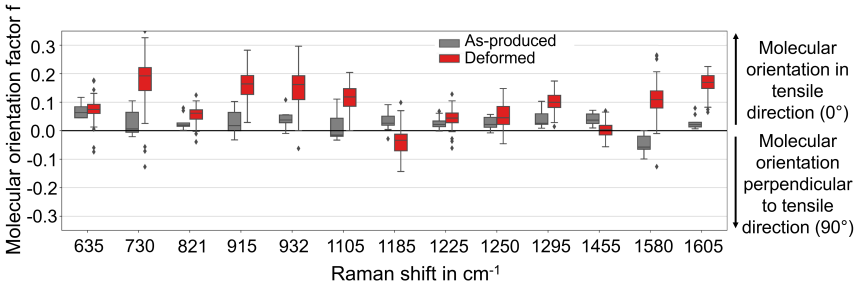

Figure 5.47: The molecular orientation factor is shown as box plot for each Raman peak of three type A samples recorded at a minimum of 2 positions for each sample and region (as-produced deformed). The factor is determined from Equation 4.8 with the 0° and 90° polarized Raman intensity.

The peak at 1185 cm^{-1} corresponds to the in-plane stretching vibration of *gem*-dimethyl group of bisphenol A between the aromatic rings and the peak at 1455 cm^{-1} is related to the methyl and methylene vibrations (see chemical structure of DGEBA in Figure 3.6) [5, 137, 221]. Both peaks correspond to molecules that are not part of the backbones. In addition, the aforementioned side bonds are almost perpendicular to the backbone [5]. If the backbones are oriented in the tensile direction (0°), these bonds are increasingly aligned perpendicular to the tensile direction (90°).

The fact that molecular orientations can only be found in severely deformed or necked sample areas can be seen visually again in Figure 5.48. At different sample positions of at type A sample within the gauge length (marked as gray dots in Figure 5.48 (a), Raman spectra in the 0° and 90° polarization directions (I_0, I_90) were recorded and used for the calculation (see Equation 4.8) of the molecular orientation factor of the peak at 1605 cm^{-1}, which corresponds to C-C stretching vibrations in aromatic rings. The calculation results are shown in Figure 5.48 (b).

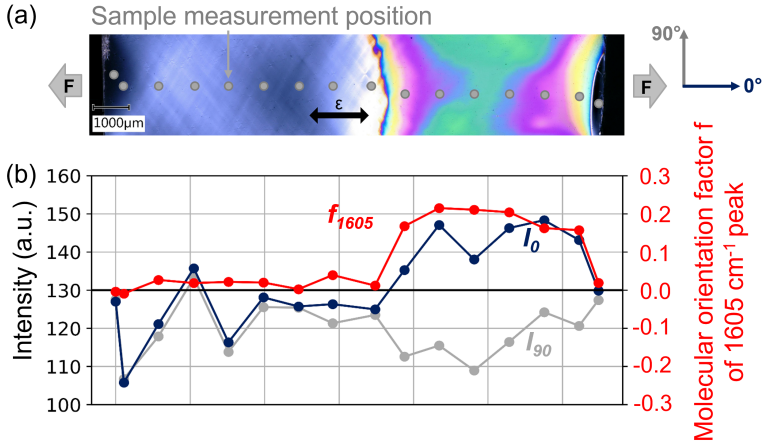

Figure 5.48: Photoelastic image of a necked type A sample with a thickness of 100 µm (reached maximum Deben elongation of $\epsilon = 17\,\%$) with white shear bands and yellow, purple and green colored mechanically stressed and deformed sample region (a) and the molecular orientation factor (red line) determined for the aromatic peak at 1605 cm^{-1} for different sample positions (marked as gray dots in photoelastic image) in the gauge length. The corresponding intensities of the aromatic peak at 1605 cm^{-1} for each sample measurement point for the 0° and 90° polarized measurements are shown as well (gray and dark blue lines in (b)).

Intermediate summary

The polarized IR (see Chapter 5.3.3) and polarized Raman outcomes lead to the conclusion that in highly deformed and necked sample areas with shear bands, the backbones with the aromatic rings are oriented in the tensile direction and the side molecules get oriented perpendicular to the backbones as a result.

This confirms the following hypothesis:

5. *Shear bands represent deformation areas with oriented and stretched molecular backbones in epoxy.*

As discussed in Chapter 2.1, in thermoplastic deformed materials with shear bands, a thermal annealing above the glass transition temperature T_g causes a shear band removal [77]. In order to figure out whether this also applies to epoxy, thermal treatment tests were carried out. The corresponding results are presented in the next chapter.

5.5 Thermal annealing

After thermal annealing for 3 h at a temperature T of 70°C, i.e, below T_g (90°C), of deformed epoxy film samples with shear bands, photoelastic images still demonstrate shear bands and deformation, as can be seen in Figure 5.49. However, the visually detectable intensity of the deformation and shear bands appears to be reduced in comparison to the photoelastic images after creep loading because the white regions are lighter after thermal annealing. In contrast to this, thermal annealing of deformed epoxy film samples with shear bands at temperatures above the glass transition temperature T_g, i.e., 100°C, shows that heat application leads to almost complete removal of the shear bands. Also the shape of the sample nearly returns to its initial dimensions. This can be seen in Figure 5.52. The removal of the deformation and shear band due to a heat treatment above T_g was detectable for the HBPA-DGE film sample as well (see Appendix Figure 29).

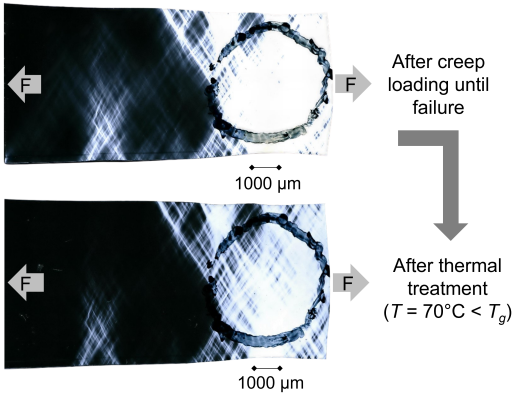

Figure 5.49: Photoelastic images of a representative type A film specimen with a thickness of 30 µm after creep loading (at 70 % UTS) until finial failure and after a subsequent thermal annealing at a temperature T of 70°C ($T < T_g$) for 3 h.

The reason for this behavior is the increased mobility of the molecules at a temperature higher than the glass transition temperature. Only in this temperature range the molecules are movable and can reorient and return to equilibrium positions. This results in a relaxation of the entire polymer network, the removal of shear bands, and the return to the initial sample shape (see Figure 5.52).

As a proof of concept, the load-induced spectral changes in the shear bands must also be reversed by thermal annealing above T_g. The spectra after mechanical loading and a subsequent thermal annealing have to be identical to the initial as-produced state spectra. Figure 5.50 shows the aromatic peak wavenumber $\tilde{v}_{1608}$ of the initial sample state, after mechanical loading and deformation and after the subsequent thermal annealing above T_g recorded with the TENSOR II device. A back shift towards higher aromatic peak wavenumbers closer to the initial state can be detected.

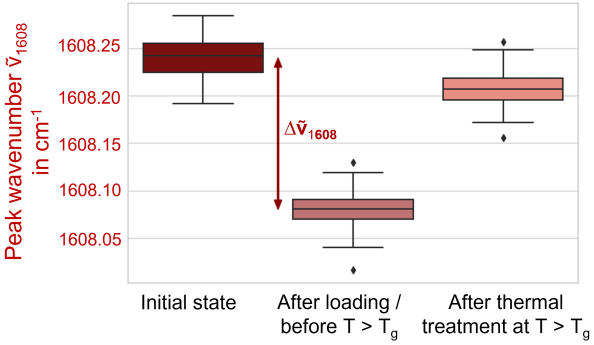

Figure 5.50: *Ex situ* IR results of a creep-loaded film specimen of type A with a thickness of 30 µm. The initial aromatic peak wavenumber at 1608 cm^{-1}, the red-shifted $\tilde{v}_{1608}$ after mechanical loading and the back shifted $\tilde{v}_{1608}$ after subsequent thermal annealing above T_g are determined. Each gray dot represent a recorded spectrum at the same specimen position.

In the context of the entropy-related deformation and the fact that the backbones can be more easily or more homogeneously stretched after a previous alignment in the load direction, there should no longer be an absorbance dependence of the polarization direction detectable in the polarized IR results after thermal annealing above T_g.

Figure 5.51 pictured the polarization angles or directions and the corresponding absorbance after mechanical creep loading and after a subsequent thermal expansion. After mechanical creep loading, the aromatic backbones are aligned in the load direction (0°) as the absorbance is highest for the polarization mode in load direction (see Chapter 5.3.3). After a subsequent thermal annealing at a temperature of 100°C, i.e., above T_g, there is no longer a significant difference in the absorbance of the different polarization directions. This is an additional indication that the backbones have returned to an equilibrium conformation as a result of the heat expansion. After thermal annealing above the glass transition temperature the molecules are not longer stretched and aligned in the load direction. Additionally, it was possible to show that the shear bands occur again at the same sample position if a second creep test is performed after thermal annealing. The stress state for shear yielding might still be appropriate in the previous formed shear bands.

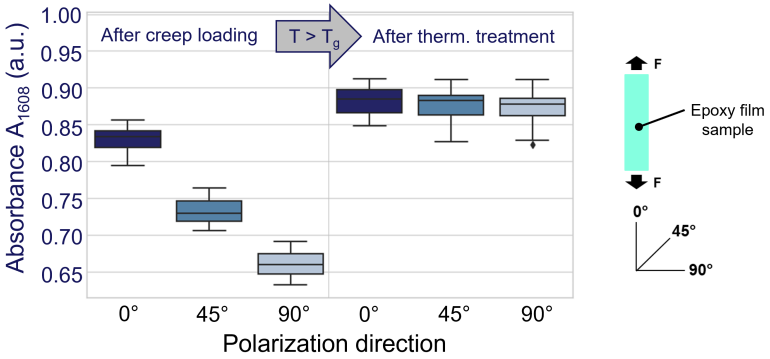

Figure 5.51: *Ex situ* polarized IR results of a creep-loaded film specimen of type A with a thickness of 30 µm. The aromatic absorbance A_{1608} is evaluated regarding the polarization direction after mechanical creep loading (left) and after subsequent thermal annealing at a temperature above T_g (right).

Figure 5.52 shows the results of the *ex situ* IR microscope of different sample states (as produced, creep loaded, and thermally treated) to improve the distinguishing between deformed and undeformed sample regions and to analyze the shear band recovery on the molecular level further. It can also be seen here that the aromatic wavenumber $\tilde{v}_{1608}$ in the shear bands assumes a reduced value after mechanical testing (red-shift) as it was presented in the last chapters.

If the mechanical creep test is followed by thermal annealing above T_g, not only do the shear bands disappear in the photoelastic image but also the reduced wavenumbers $\tilde{\nu}_{1608}$ in the previously deformed region with shear bands returns to the initial as-produce state. The peak wavenumber visualization shows that some aromatic rings might be a little bit stressed even after the thermal annealing since some random areas still exhibit slightly increased aromatic peak wavenumber values, but explicit not in the previous formed shear bands.

In Figure 5.52 it is also shown what happens after a second creep test subsequent after the thermal annealing. A second creep loading results in the reappearance of shear bands in the same specimen regions as during the first creep loading and leads again to a red-shift in the corresponding shear band areas. This is also evident in Figure 5.50. After thermal annealing at 100°C, the aromatic wavenumber $\tilde{\nu}_{1608}$ is again close to the initial peak wavenumber value. This means that despite thermal annealing, the stresses in these sample areas are still the most favorable for shear yielding and the internal energy in the aromatic rings changes again at these points when the backbone are stretched and lengthened again.

Intermediate summary

The findings from the thermal annealing confirm that *plasticity* does not mean permanent if thermal annealing is taken into account. A thermal annealing above the glass transition temperature T_g proved that the molecular rearrangement (polarized IR) and stretching processes (peak shifts) which takes place during macroscopic deformation under tension loads are reversible. The molecules return to energetically favorable equilibrium positions. This confirms the last research hypothesis:

6. *Shear bands and constricted regions in epoxy regress at temperatures above the glass transition temperature. The molecular structure then returns to a more favorable equilibrium conformation, and the sample returns in the initial geometric dimensions.*

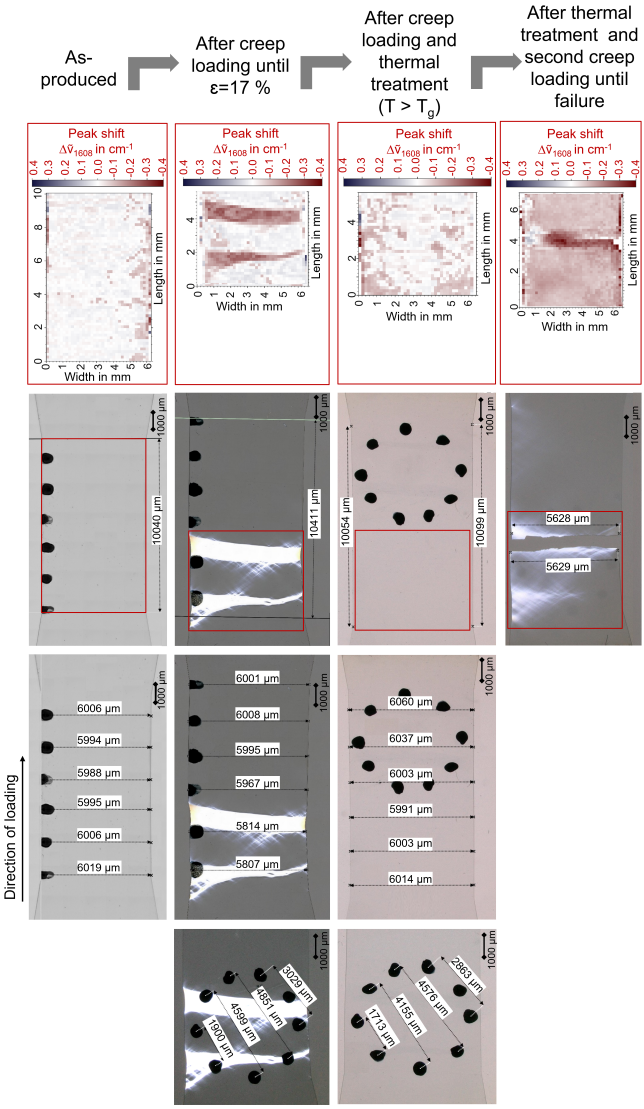

Figure 5.52: Correlation of photoelastic images and *ex situ* IR microscope results of a representative type A film specimen with a thickness of 30 µm in the as-produced state, after creep loading until $\epsilon = 17\,\%$, after thermal annealing (3 h at $T > T_g$) and after the second creep loading until final failure is shown. The photoelastic images display the geometric dimensions of the sample as well as markings for identification at different sample states. The IR visualization includes pixels where each one correspond to a spectrum. All recorded spectra are evaluated regarding the aromatic peak shift $\Delta\tilde{\nu}_{1608}$ and each pixel is colored according to the corresponding value. The sample region which are analyzed with IR are marked by a red frame in the photoelasti images.

6 Evaluation of hypotheses

The first part of this thesis deals with the development of a sophisticated manufacturing technique to produce epoxy films with thicknesses between 15 and 100 µm. The thicknesses of the epoxy films were chosen with regard to the size range or dimension of the resin-rich zones between fibers and the resin-rich zones between reinforcing prepregs or layers in polymeric composites. The manufactured film samples were extensive characterized with different methods in order to understand the relationships between deformation behavior and microstructure processes. The different testing techniques confirmed the following two hypotheses:

1. *Micro-scaled thin epoxy resin films can deform ductile under tensile loads.*
2. *High local strains and stress results in shear bands as visible deformation mechanisms under tensile loads.*

Vibrational spectroscopic analysis was found to can be performed to correlate molecular mechanisms within epoxy and the corresponding macroscopic mechanical behavior. The polarization angle-dependent IR absorbance and Raman intensity for the peak at $1608\,\mathrm{cm}^{-1}$ (IR) and $1605\,\mathrm{cm}^{-1}$ (Raman) is accompanied by an in-plane stretching of the aromatic ring and mainly its C atoms. This peak or vibration mode indicates a molecular alignment in the load direction within the deformed sample regions, since the IR absorbance or Raman intensity of the aromatic components there is highest in 0°, which is parallel to the load direction. At first glance, it might be assumed that the molecular backbones are approximately oriented in 45°, just as the macroscopic visible shear bands. However, the IR absorbance at a polarization angle of 45° is significantly lower than at 0°, which means that fewer molecular chains are oriented in the 45° direction. Approximately in 45° direction, the maximum shear stress occurs first, but with further load application, the backbones in the shear band areas get oriented in the 0° load direction like in thermoplastics.

The dimethyl groups between the aromatics show an orientation perpendicular to the load direction (90°), which is the consequence when the backbones are oriented in the load direction. This phenomenon results in a decrease of the entropy S.

After the alignment of the backbones, the bond distances in the backbones, especially between the aromatic carbon atoms increase further, as was shown in MD simulations related to the project [211] and can be measured experimentally as a decrease in the aromatic peak wavenumber at $1608\,\mathrm{cm}^{-1}$ (red-shift) and as an increase in the aromatic peak wavenumber at $829\,\mathrm{cm}^{-1}$ (blue-shift). Together with the Badger rule and a load-induced increasing bond distance between the aromatic C-C atoms, the aromatic red-shift $\Delta\tilde{\nu}_{1608}$ toward lower peak wavenumbers can be explained as a consequence of an energy-related deformation. However, the blue-shift of the aromatic C-H vibration at a wavenumber of $829\,\mathrm{cm}^{-1}$ is an indirect consequence of the stretching of the aromatic C-C, as the C-H bond is not a direct part of the backbone and is therefore not directly stretched. The blue-shift is caused by a stretch-induced increased polarization of the aromatic rings.

All spectroscopic findings strengthened each other and confirmed the following hypotheses:

3. *Vibrational spectroscopic analysis can be performed to correlate the molecular mechanisms within epoxy with the macroscopic mechanical behavior.*

4. *The ductility in epoxy is enabled by molecular rearrangement processes in the cross-linked network.*

Even if most of the peaks analyzed are related to the aromatic structures in the backbones, it was possible to exclude aromatic rings in the backbones as a requirement for shear band and neck formation in epoxy film samples. Film samples made from another epoxy system (HBPA-DGE) without aromatic rings in the backbones exhibit shear bands under tensile load as well. Shear bands occur as deformation mechanisms under tensile loads in different epoxy systems. These findings confirmed the research hypothesis as well:

5. *Shear bands represent deformation areas with oriented and stretched molecular backbones in epoxy.*

The work also showed that the neck and the shear bands are not plastic irreversible deformation processes in the classical sense. Although deformations persist at room temperature for a period of several years, thermal annealing above T_g of previously deformed specimens with shear bands has shown that film samples return to their initial geometry and all shear bands disappear due to the thermal energy contributed. The sample looks as before mechanical loading, and the corresponding (polarized) IR spectra are also almost identical to those of the initial state before mechanical testing. If a second mechanical loading is applied after the thermal annealing process, the shear bands usually appear again in similar sample areas and a red-shift of the aromatic peak at $1608\,\mathrm{cm}^{-1}$ can be detected again in the IR spectrum. The shear bands can then also be removed once again by annealing them above T_g at $100\,^{\circ}\mathrm{C}$. The thermal energy introduced must therefore exceed the deformation work performed in the mechanical test. Removals at temperatures below T_g, for example at $70\,^{\circ}\mathrm{C}$, causes a decrease of the shear band intensity, but there is no complete recovery. This is also true for HBPA-DGE film samples. Only when T_g is reached the thermal energy is high enough and the molecules can react to the restoring force because they are now mobile enough to achieve a more energetically and entropically favorable state of equilibrium. If thermal energy is supplied to the system during thermal annealing, the decreasing entropy caused by the alignment of the backbone under mechanical load is counteracted, and the macromolecules are brought closer to the disordered state again through more intensive chain movement. Polarized IR measurements have shown that molecular orientations cannot be detected anymore after a thermal annealing process above T_g. This confirmed the last research hypothesis:

6. *Shear bands and constricted regions in epoxy regress at temperatures above the glass transition temperature. The molecular structure then returns to a more favorable equilibrium conformation, and the sample returns in the initial geometric dimensions.*

The results of the hypothesis verification have shown that there is a cascade from the macroscopic level (mechanical properties) to the electron level (aromatic C-H blue-shift IR) in stressed epoxy film samples. To the author's knowledge, it was the first time that such extensive investigations were carried out on microscale epoxy resin samples, where not only the mechanical behavior in different mechanical tests was analyzed, but above all the molecular mechanisms occurring as causes could be detected by various *in situ* and *ex situ* spectroscopic methods.

Additionally, by applying thermal energy, the internal stresses in the samples and changes in the microstructure can be relieved again, so that the mechanisms and relationships described are reversible, which is a complete new finding for epoxy resins.

7 Conclusion

The key finding of this work is that epoxy film samples with small test volumes experience a significant increase in plastic (like) deformation behavior. The reduced test volume compared to standard samples favors yielding due to a larger amount of sample regions in plane stress state. After reaching the yield stress, pronounced shear bands are formed with maximum width averaged local strain values of about 60 %. This process continues until the sample is necked over the entire test length.

It was possible to show for the first time, that at the molecular level, the aromatic compounds in the backbones are directly involved in load transfer and undergo alignment and stretching during plastic like deformation and shear band formation in the regions with high local strains, as evidenced by IR peak-shifts as well as a polarization angle-dependent IR absorbance and Raman intensity for specific peaks. Together, the peak shifts and polarization-dependent absorbance show that the higher ductility and shear band formation are the result of a superimposed energy- and entropy-related deformation. This shows that although mechanical stress can lead to changes in bond lengths and angles, strains can occur only if a specific amount of entanglements are first removed and the entropy is reduced.

During the deformation process, entropy decreases due to the molecular alignment of the backbones, and the inner energy increases as a result of the change in the bond lengths and angles. To analyze the associated change in molecular density in the shear bands, a special µ-CT device with even higher density resolution could be used.

The often used term *plasticity* in the context of shear yielding in polymers should be reconsidered since it is not really a permanent irreversible deformation process as the thermal annealing results of this thesis show. Nevertheless, in the presented thesis, the term *plastic like* is used to differ the over the time at room temperature remaining deformation with shear bands from the spontaneous elastic behavior. Related to the term entropy elasticity and the new finding in this thesis, the described behavior is more like a *frozen entropy-related deformation* since it is not an elastic behavior. With thermal energy application, the material volume, respective sample width increases, the molecules have enough space to return in a preferred equilibrium position, and the sample dimensions are nearly exactly as before mechanical testing. Especially above T_g, the molecules lose their alignment and return to a coil-like structure without further order and with higher entropy. The term *plastic* or *permanent* is just true for a period of time over a few years (duration of this thesis) at room temperature (below T_g). Under these circumstances the energy barrier cannot be overcome, and the molecules cannot return to an equilibrium position as the space and flexibility is limited as a result of neighboring molecules as hindrances. These are important new findings, also for returning deformed epoxy resin materials to their original shape.

The question of how this plastic like deformation due to unraveling of entanglements, alignment of molecular backbones, and stretching of molecules similar to thermoplastics is also possible in highly cross-linked epoxy films could be answered comprehensively for the first time within this doctoral thesis, but why it is possible at all is still an open question. There may also be physical entanglements between cross-linking points that can be removed, as well as stretching and orientation of molecular chains between the cross-links to a certain extent, but this cannot explain the significant increase in ductility and the formation of shear bands. Another hypothesis is that even in an overall dense epoxy network, high- and low-density cross-linked regions exist in a statistical distribution. Under load, the stress-sensitive covalent bonds in the backbones in sample regions with less dense network structure may react first to external load with some molecular movement, followed by molecular stretching as well.

Another point that should be investigated in more detail in the future is the influence of the manufacturing conditions on these stress and strain-induced changes in the epoxy resin microstructure. Altering the thermal curing cycle during the film manufacturing offers a means to influence the development of the molecular network and, as a result, the final molecular architecture of the completely cured system.

The theory of Bowden contains similarity to the deformation of thermosets and the movement of dislocations in metals. However, a requirement might be that cross-links can be „opened“ and „closed“ several times to have a comparatively molecular mechanism like dislocations in epoxies. MD simulations clarify the competition of bond dissociation and bond reformation during plastic (like) deformation and fractures. The study of Konrad et al. [223] has shown that cross-links can recombine under load or during plastic (like) deformation shortly before finial failure. This has to be experimentally investigated further to detect possible radicals that may occur during bond dissociation, and this might be challenging because of the opportunity of very fast recombination and a new cross-link formation during plastic like deformation. However, in the *in situ* IR results, no indications were found that significant bond breakings occur. It could be that the temporal or spectral resolution was not high enough.

Further *in situ* investigation of the molecular backbone movement process during loading and deformation could be performed in the future with an IR device which allows simultaneous recording of spectra for different polarization angles (0°, 45°, 90°) and consideration of the general absorbance decrease due to the constriction or thickness decrease in the shear band zones (Beer's law) to measure the gradual molecular backbone alignment as a response to external load application.

In the next step, the behavior of epoxies as a matrix component in FRP should be investigated with regard to the plastic deformability of small-volume matrix regions under non plane-stress conditions. The knowledge about this can further help to optimize the mechanical behavior of FRPs since the matrix deformation potential significantly affects the overall mechanical behavior of FRPs. For even more accurate modeling and design of FRPs, the mechanical behavior of epoxy should not be based on the mechanical properties of bulk samples, but on the properties of microscopic epoxysamples as presented in this doctoral thesis in order to improve the accuracy of micromechanics-based models.

Bibliography

[1] O. Verschatse, L. Daelemans, W. V. Paepegem, and K. de Clerck. "In-Situ Observations of Microscale Ductility in a Quasi-Brittle Bulk Scale Epoxy". In: *Polymers* 12.11 (2020). DOI: 10.3390/polym12112581.

[2] T. J. Vaughan and C. T. McCarthy. "Micromechanical modelling of the transverse damage behaviour in fibre reinforced composites". In: *Composites Science and Technology* 71.3 (2011), pp. 388–396. DOI: 10.1016/j.compscitech.2010.12.006.

[3] W. Tan, F. Naya, L. Yang, T. Chang, B. G. Falzon, L. Zhan, J. M. Molina-Aldareguía, C. González, and J. LLorca. "The role of interfacial properties on the intralaminar and interlaminar damage behaviour of unidirectional composite laminates: Experimental characterization and multiscale modelling". In: *Composites Part B: Engineering* 138 (2018), pp. 206–221. ISSN: 13598368. DOI: 10.1016/j.compositesb.2017.11.043.

[4] M.-F. Ren, X.-W. Zhang, C. Huang, B. Wang, and T. Li. "An integrated macro/micro-scale approach for in situ evaluation of matrix cracking in the polymer matrix of cryogenic composite tanks". In: *Composite Structures* 216 (2019), pp. 201–212. DOI: 10.1016/j.compstruct.2019.02.079.

[5] X. M. Sui, I. Pinkas, and H. D. Wagner. "A polarized micro-Raman study of necked epoxy fibers". In: *Polymer* 230 (2021). DOI: 10.1016/j.polymer.2021.124034.

[6] X. M. Sui, M. Tiwari, I. Greenfeld, R. L. Khalfin, H. Meeuw, B. Fiedler, and H. D. Wagner. "Extreme scale-dependent tensile properties of epoxy fibers". In: *eXPress Polymer Letters* 13.11 (2019), pp. 993–1003. DOI: 10.3144/expresspolymlett.2019.86.

[7] J. Mittelhaus, S. P. Bhusare, N. Pournoori, M. Isakov, T. Salminen, P. Laurikainen, E. Sarlin, G. Mohanty, and B. Fiedler. "Understanding the scale dependent ductility of epoxies". In: *ECCM21 - 21th European Conference on Composite Materials* 2 (2024), pp. 300–307. DOI: 10.60691/yj56-np80.

[8] A. J. Kinloch, D. G. Gilbert, and S. J. Shaw. "A mechanism for ductile crack growth in epoxy polymers". In: *Journal of Materials Science* 21 (1986), pp. 1051–1056. DOI: 10.1007/BF01117394.

[9] R. P. Wool. "Mechanisms of frequency shifting in the infrared spectrum of stressed Polymers". In: *Journal of Polymer Science: Part B: Polymer Physics* 13 (1975), pp. 1795–1808. DOI: 10.1002/pol.1975.180130912.

[10] A. Sturcová, S. J. Eichhorn, and M. C. Jarvis. "Vibrational spectroscopy of biopolymers under mechanical stress: processing cellulose spectra using bandshift difference integrals". In: *Biomacromolecules* 7.9 (2006), pp. 2688–2691. ISSN: 1525-7797. DOI: 10.1021/bm060457m.

[11] S. N. Zhurkov, V. E. Korsukov, I. I. Novak, and V. I. Vettegren. "Determination of overstressed chemical bonds in polymers by the method of infrared spectroscopy". In: *Fiz. tverd. tela,* 11.2 (1969), pp. 290–295.

[12] V. I. Vettegren and I. I. Novak. "Determination of atomic stress distribution in stressed polymers by infrared spectroscopy". In: *Journal of Polymer Science: Part B: Polymer Physics* 11 (1973), pp. 2135–2142. DOI: 10.1002/pol.1973.180111105.

[13] V. I. Vettegren and I. I. Novak. "Determination of the true stresses on interatomic bonds in loaded polymers by the infrared spectroscopy method". In: *Fiz. tverd. tela,* 15.5 (1973), pp. 1417–1422.

[14] V. I. Vettegren, I. I. Novak, and K. J. Friedland. "Overstressed interatomic bonds in stressed polymers". In: *International Journal of fracture* 11.5 (1975), pp. 789–801. DOI: 10.1007/BF00012897.

[15] V. M. Voroboyev, I. V. Razumovskaya, and V. I. Vettegren. "Deformation of interatomic bonds in polymers". In: *Polymer* 19.11 (1978), pp. 1267–1272. DOI: 10.1016/0032-3861(78)90303-8.

[16] D. K. Roylance and K. L. DeVries. "Determination of atomic stress distribution in oriented polypropylene by infrared spectroscopy". In: *Polymer Letters* 9.6 (1971), p. 443. DOI: 10.1002/pol.1971.110090607.

[17] S. J. Eichhorn and R. J. Young. "Deformation micromechanics of natural cellulose fibre network and composites". In: *Composites Science and Technology* 63.9 (2003), pp. 1225–1240. DOI: 10.1016/S0266-3538(03)00091-5.

[18] C. Galiotis, R. J. Young, P. H. J. Yeung, and D. N. Batchelder. "The study of model polydiacetylene/epoxy composites, Part 1 The axial strain in the fibre". In: *Journal of Materials Science* 19.11 (1984), pp. 3640–3648. ISSN: 0022-2461. DOI: 10.1007/BF02396936.

[19] I. M. Robinson, R. J. Young, C. Galiotis, and D. N. Batchelder. "Study of model polydiacetylene/epoxy composites, Part 2 Effect of resin shrinkage". In: *Journal of Materials Science* 22.10 (1987), pp. 3642–3646. ISSN: 0022-2461. DOI: 10.1007/BF01161472.

[20] R. J. Young, R. J. Day, M. Zakikhani, and I. M. Robinson. "Fibre deformation and residual thermal stresses in carbon fibre reinforced PEEK". In: *Composites Science and Technology* 34.3 (1989), pp. 243–258. DOI: 10.1016/0266-3538(89)90031-6.

[21] C. Galiotis, N. Melanitis, D. N. Batchelder, I. M. Robinson, and J. A. Peacock. "Residual strain mapping in carbon fibre/PEEK composites". In: *Composites* 19.4 (1988), pp. 321–324. ISSN: 0010-4361. DOI: 10.1016/0010-4361(88)90009-2.

[22] F. A. Gilabert, D. Garoz, R.D.B. Sevenois, S.W.F. Spronk, A. Rezaei, W. V. Paepegem, and ESCM. "Composite micro-scale model accounting for debonding, strain-rate dependence and damage under impact using an explicit finite element solver". In: *17th European Conference on Composite Materials* (2016), pp. 1–8.

[23] L. Mishnaevsky. "Composite materials for wind energy applications: micromechanical modeling and future directions". In: *Computational Mechanics* 50.2 (2012), pp. 195–207. ISSN: 0178-7675. DOI: 10.1007/s00466-012-0727-5.

[24] W.-Y. Yeh and R. J. Young. "Molecular deformation processes in aromatic high modulus polymer fibres". In: *Polymer* 40.4 (1999), pp. 857–870. DOI: 10.1016/S0032-3861(98)00308-5.

[25] R. J. Young, R. J. Day, and M. Zakikhami. "The structure and deformation behaviour of poly(p-phenylene benzobisoxazole) fibres". In: *Journal of Material Science* 25 (1990), pp. 127–136. DOI: 10.1007/BF00544197.

[26] W.-Y. Yeh and R. J. Young. “Deformation processes in poly(ethylene terephthalate) fibers”. In: *Journal of Macromolecular Science, Part B* 37.1 (1998), pp. 83–118. ISSN: 0022-2348. DOI: 10.1080/00222349808220457.

[27] C. Galiotis, I. M. Robinson, R. J. Young, B. J. E. Smith, and D. N. Batchelder. “Strain dependence of the Raman frequencies of a Kevlar 49 fibre”. In: *Polymer Communications* 26.12 (1985), pp. 354–355.

[28] S. van der Zwaag, M. G. Northolt, R J. Young, I. M. Robinson, C. Galiotis, and D. N. Batchelder. “Chain Stretching in Aramid Fibers”. In: *Polymer Communications* 28 (1987), pp. 276–277.

[29] I. M. Robinson, M. Zakikhani, R. J. Day, R. J. Young, and C. Galiotis. “Strain dependence of the Raman frequencies for different types of carbon fibres”. In: *Journal of Materials Science Letters* 6.10 (1987), pp. 1212–1214. ISSN: 0261-8028. DOI: 10.1007/BF01729187.

[30] C. Galiotis and D. N. Batchelder. “Strain dependences of the first- and second-order Raman spectra of carbon fibres”. In: *Journal of Materials Science Letters* 7.5 (1988), pp. 545–547. ISSN: 0261-8028. DOI: 10.1007/BF01730722.

[31] S. J. Eichhorn, Sirichaisit, and R. J. Young. “Deformation mechanisms in cellulose fibres, paper and wood”. In: *Journal of Materials Science* 36 (2001), pp. 3129–3135. DOI: 10.1023/A:1017969916020.

[32] S. J. Eichhorn, R. J. Young, and W.-Y. Yeh. “Deformation Processes in Regenerated Cellulose Fibers”. In: *Textile Research Journal* 71.2 (2001), pp. 121–129. ISSN: 0040-5175. DOI: 10.1177/004051750107100206.

[33] A. Sturcová, G. R. Davies, and S. J. Eichhorn. “Elastic modulus and stress-transfer properties of tunicate cellulose whiskers”. In: *Biomacromolecules* 6.2 (2005), pp. 1055–1061. ISSN: 1525-7797. DOI: 10.1021/bm049291k.

[34] B. Hinterstoisser, M. Akerholm, and L. Salmén. “Load distribution in native cellulose”. In: *Biomacromolecules* 4.5 (2003), pp. 1232–1237. ISSN: 1525-7797. DOI: 10.1021/bm030017k.

[35] P. Peetla, K. C. Schenzel, and W. Diepenbrock. “Determination of mechanical strength properties of hemp fibers using near-infrared fourier transform Raman microspectroscopy”. In: *Applied Spectroscopy* 60.6 (2006), pp. 682–691. DOI: 10.1366/000370206777670602..

[36] J. Sirichaisit, V. L. Brookes, R. J. Young, and F. Vollrath. "Analyis of structure/property relationships in silkworm (Bombyx mori) and spider dragline (Nephila edulis) silks using raman spectroscopy". In: *Biomacromolecules* 4.2 (2003), pp. 387–394. ISSN: 1525-7797. DOI: 10.1021/bm0256956.

[37] J. Sirichaisit, R. J. Young, and F Vollrath. "Molecular deformation in spider dragline silk subjected to stress". In: *Polymer* 41 (2000), pp. 1223–1227. DOI: 10.1016/S0032-3861(99)00293-1.

[38] A. Jelić, M. Sekulić, M. Travica, J. Gržetić, V. Ugrinović, A. D. Marinković, A. Božić, M. Stamenović, and S. Putić. "Determination of Mechanical Properties of Epoxy Composite Materials Reinforced with Silicate Nanofillers Using Digital Image Correlation (DIC)". In: *Polymers* 14.6 (2022). DOI: 10.3390/polym14061255.

[39] J. Jefferson A., V. Arumugam, D. J. Bull, and H. N. Dhakal. "Residual strength and damage characterization of repaired glass/epoxy composite laminates using A.E. and D.I.C". In: *Composite Structures* 152 (2016), pp. 124–139. DOI: 10.1016/j.compstruct.2016.05.005.

[40] Z. Jin, S. Li, H. Song, Z. Li, and D. Zhu. "Experimental and simulative study of bonding properties on fiber/epoxy interfaces by digital image correlation (DIC) technique and molecular dynamics". In: *Cement and Concrete Composites* 131 (2022), p. 104569. ISSN: 09589465. DOI: 10.1016/j.cemconcomp.2022.104569.

[41] K. Naresh, K. Shankar, R. Velmurugan, and N. K. Gupta. "High strain rate studies for different laminate configurations of bi-directional glass/epoxy and carbon/epoxy composites using DIC". In: *Structures* 27 (2020), pp. 2451–2465. ISSN: 23520124. DOI: 10.1016/j.istruc.2020.05.022.

[42] A. Taylor Owens and Hareesh V. Tippur. "Measurement of mixed-mode fracture characteristics of an epoxy-based adhesive using a hybrid digital image correlation (DIC) and finite elements (FE) approach". In: *Optics and Lasers in Engineering* 140 (2021), p. 106544. ISSN: 01438166. DOI: 10.1016/j.optlaseng.2021.106544.

[43] S. Zike, B. F. Sørensen, and L. P. Mikkelsen. "Experimental determination of the micro-scale strength and stress-strain relation of an epoxy resin".

In: *Materials & Design* 98 (2016), pp. 47–60. ISSN: 02641275. DOI: 10.1016/j.matdes.2016.02.102.

[44] D. I. Bower. "Investigation of molecular orientation distributions by polarized raman scattering and polarized fluorescence". In: *Journal of Polymer Science: Polymer Physics Edition* 10.11 (1972), pp. 2135–2153. ISSN: 00981273. DOI: 10.1002/pol.1972.180101103.

[45] D. I. Bower. "Raman scattering from an assembly of partially oriented scatterers". In: *Journal of Physics B: Atomic and Molecular Physics* 9.18 (1976), pp. 3275–3293. ISSN: 00223700. DOI: 10.1088/0022-3700/9/18/018.

[46] B. Jasse and J. L. Koenig. "Orientational Measurements in Polymers Using Vibrational Spectroscopy". In: *Journal of Macromolecular Science, Part C: Polymer Reviews* 17.1 (1979), pp. 61–135. ISSN: 1532-1797. DOI: 10.1080/00222357908080905.

[47] B. Jasse and J. L. Koenig. "Polarized Raman study of molecular orientation in uniaxially stretched atactic polystyrene". In: *Journal of Polymer Science: Polymer Physics Edition* 18.4 (1980), pp. 731–738. ISSN: 00981273. DOI: 10.1002/pol.1980.180180406.

[48] L. Svenningsson and L. Nordstierna. "Polarized Raman Spectroscopy Strategy for Molecular Orientation of Polymeric Fibers with Raman Tensors Deviating from the Molecular Frame". In: *ACS Applied Polymer Materials* 2.11 (2020), pp. 4809–4813. ISSN: 2637-6105. DOI: 10.1021/acsapm.0c00762.

[49] R. P. Wool and W. O. Statton. "Dynamic Polarized Infrared Studies of Stress Relaxation and Creep in Polypropylene". In: *Journal of Polymer Science: Part B: Polymer Physics* 12 (1974), pp. 1575–1586.

[50] E. Unsal, I. I. Nugay, I. Offenbach, M. Gross, C. Manning, and M. Cakmak. "Rapid integrated rheo-optical and polarized Fourier-transform infrared spectrometry measurement system for polymer films undergoing chemo-mechanical changes". In: *The Review of scientific instruments* 84.7 (2013), p. 073901. DOI: 10.1063/1.4811845.

[51] S. Frisk, R. M. Ikeda, D. B. Chase, and J. F. Rabolt. "Determination of the molecular orientation of poly(propylene terephthalate) fibers using polarized Raman spectroscopy: a comparison of methods". In: *Applied*

Spectroscopy 58.3 (2004), pp. 279–286. ISSN: 0003-7028. DOI: 10.1366/000370204322886618.

[52] A. Soto, S. M. Iconomopoulou, A. C. Manikas, and G. A. Voyiatzis. "Molecular orientation of poly(ethylene terephthalate) and poly(butylene terephthalate) probed by polarized Raman spectra: a parallel study". In: *Applied Spectroscopy* 59.10 (2005), pp. 1257–1269. DOI: 10.1366/000370205774430882.

[53] C.C.C. Lesko, J. F. Rabolt, R. M. Ikeda, B. Chase, and A. Kennedy. "Experimental determination of the fiber orientation parameters and the Raman tensor of the 1614cm−1 band of poly(ethylene terephthalate)". In: *Journal of Molecular Structure* 521.1-3 (2000), pp. 127–136. DOI: 10.1016/S0022-2860(99)00430-5.

[54] S. Yang and S. Michielsen. "Orientation Distribution Functions Obtained via Polarized Raman Spectroscopy of Poly(ethylene terephthalate) Fibers". In: *Macromolecules* 36.17 (2003), pp. 6484–6492. DOI: 10.1021/ma034486q.

[55] M. J. Citra, D. B. Chase, R. M. Ikeda, and K. H. Gardner. "Molecular Orientation of High-Density Polyethylene Fibers Characterized by Polarized Raman Spectroscopy". In: *Macromolecules* 28.11 (1995), pp. 4007–4012. DOI: 10.1021/ma00115a037.

[56] X. Chen, M. A. Leugers, T. Kirch, and J. Stanley. "Orientation Mapping of Extruded Polymeric Composites by Polarized Micro-Raman Spectroscopy". In: *Journal of Spectroscopy* (2015), pp. 1–7. ISSN: 2314-4920. DOI: 10.1155/2015/518054.

[57] G. W. Ehrenstein. *Polymer Werkstoffe: Struktur-Eigenschaften-Anwendung*. 3rd ed. München: Carl Hanser, 2011. ISBN: 978-3-446-42283-4. DOI: 10.3139/9783446429673.

[58] A. J. Kinloch and R. J. Young. *Fracture behaviour of Polymers*. Springer_Science+Business Media, 1995. ISBN: 978-94-017-1596-6.

[59] A. A. Griffith. "The Phenomena of Rupture and Flow in Solids". In: *Philosophical Transactions of the Royal Society of London. Series A, Containing Papers of a Mathematical or Physical Character* 221 (1920), pp. 163–198. URL: www.jstor.org/stable/91192.

[60] J. N. Goodier. “Concentration of Stress Around Spherical and Cylindrical Inclusions and Flaws”. In: *Journal of Applied Mechanics* 1.2 (1933), pp. 39–44. ISSN: 0021-8936. DOI: 10.1115/1.4012173.

[61] L. Mirandy and B. Paul. “Stresses at the Surface of a Flat Three-Dimensional Ellipsoidal Cavity”. In: *Journal of Engineering Materials and Technology* 98.2 (1976), pp. 164–172. DOI: 10.1115/1.3443360.

[62] E. M. Odom and D. F. Adams. “Specimen size effect during tensile testing of an unreinforced polymer”. In: *Journal of Material Science* 27 (1992), pp. 1767–1771. DOI: 10.1007/BF01107202.

[63] T. Hobbiebrunken, B. Fiedler, M. Hojo, and M. Tanaka. “Experimental determination of the true epoxy resin strength using micro-scaled specimens”. In: *Composites Part A: Applied Science and Manufacturing* 38.3 (2007), pp. 814–818. DOI: 10.1016/j.compositesa.2006.08.006.

[64] H.-H. Kausch, ed. *Crazing in Polymers*. 2nd ed. Vol. POLYMER, volume 91/92. Advances in Polymer Science. Berlin Heidelberg: Springer, 1990. ISBN: 978-3-540-51306-3.

[65] H.-J. Sue, E. I. Garcia-Meitin, P. C. Yang, and M. T. Bishop. “Crazing in high-performance thermoset resins”. In: *Journal of Materials Science Letters* 12 (1993), pp. 1463–1466.

[66] J. Rottler, S. Barsky, and M. O. Robbins. “Cracks and Crazes: On Calculating the Macroscopic Fracture Energy of Glassy Polymers from Molecular Simulations”. In: *Physical Review Letters* 14 (2002), p. 89.

[67] K. Viswanathan, S. Yadav, and D. Sagapuram. “Shear Bands in Materials Processing: Understanding the Mechanics of Flow Localization From Zener’s Time to the Present”. In: *Applied Mechanics Reviews* 72.6 (2020). ISSN: 0003-6900. DOI: 10.1115/1.4049353.

[68] A. L. Greer, Y. Q. Cheng, and E. Ma. “Shear bands in metallic glasses”. In: *Materials Science and Engineering: R: Reports* 74.4 (2013), pp. 71–132. ISSN: 0927796X. DOI: 10.1016/j.mser.2013.04.001.

[69] Q. Wei, D. Jia, K. T. Ramesh, and E. Ma. “Evolution and microstructure of shear bands in nanostructured Fe”. In: *Applied Physics Letters* 81.7 (2002), pp. 1240–1242. ISSN: 0003-6951. DOI: 10.1063/1.1501158.

[70] N. Golding, E. M. Schulson, and C. E. Renshaw. “Shear faulting and localized heating in ice: The influence of confinement”. In: *Acta Materialia* 58.15 (2010), pp. 5043–5056. DOI: 10.1016/j.actamat.2010.05.040.

[71] A. Fall, F. Bertrand, G. Ovarlez, and D. Bonn. "Yield stress and shear banding in granular suspensions". In: *Physical Review Letters* 103.17 (2009), p. 178301. DOI: 10.1103/PhysRevLett.103.178301.

[72] P. C. F. Møller, S. Rodts, M. A. J. Michels, and Daniel Bonn. "Shear banding and yield stress in soft glassy materials". In: *Physical review. E, Statistical, nonlinear, and soft matter physics* 77.4 Pt 1 (2008), p. 041507. ISSN: 1539-3755. DOI: 10.1103/PhysRevE.77.041507.

[73] M. Hatherly and A. S. Malin. "Shear bands in deformed metals". In: *Scripta Metallurgica* 18.5 (1984), pp. 449–454. ISSN: 00369748. DOI: 10.1016/0036-9748(84)90419-8.

[74] P. B. Bowden and R. J. Young. "Deformation mechanisms in crystalline polymers". In: *Journal of Materials Science* 9.12 (1974), pp. 2034–2051. ISSN: 0022-2461. DOI: 10.1007/BF00540553.

[75] J. C. M. Li. "Behavior and properties of shear bands". In: *Polymer Engineering and Science* 24.10 (1984), pp. 750–760. ISSN: 0032-3888. DOI: 10.1002/pen.760241005.

[76] G. H. Michler and F. J. Balta-Calleja. *Nano- and Micromechanics of Polymers Structure Modification and Improvement of Properties*. 2012. ISBN: 978-3-446-42767-9.

[77] C. C. Chau and J. C. M. Li. "Fracture of shear bands in atactic polystyrene". In: *Journal of Materials Science* 16.7 (1981), pp. 1858–1873. ISSN: 0022-2461. DOI: 10.1007/BF00540634.

[78] A. S. Argon and M. I. Bessonov. "Plastic deformation in polyimides, with new implications on the theory of plastic deformation of glassy polymers". In: *The Philosophical Magazine: A Journal of Theoretical Experimental and Applied Physics* Vol. 35, Issue 4 (1977), pp. 917–933.

[79] R. N. Haward, B. M. Murphy, and E. F. T. White. "Relationship between compressive yield and tensile behavior in glassy thermoplastics". In: *Journal of Polymer Science Part A-2: Polymer Physics* 9.5 (1971), pp. 801–814. ISSN: 0449-2978. DOI: 10.1002/pol.1971.160090503.

[80] K. H. Schwalbe. *Bruchmechanik metallischer Werkstoffe*. 1st ed. Hanser, 1980. ISBN: 9783446129832.

[81] R. N. Haward, ed. *The Physics of Glassy Polymers: Bowden, P.B., Ch. 5*. Dordrecht: Springer Netherlands, 1973. DOI: 10.1007/978-94-010-2355-9.

[82] H. Eyring. “Viscosity, Plasticity, and Diffusion as Examples of Absolute Reaction Rates”. In: *The Journal of Chemical Physics* 4.4 (1936), pp. 283–291. ISSN: 0021-9606. DOI: 10.1063/1.1749836.

[83] R. N. Haward and G. Thackray. “The use of a mathematical model to describe isothermal stress-strain curves in glassy thermoplastics”. In: *Proceedings of the Royal Society of London. Series A. Mathematical and Physical Sciences* 302.1471 (1968), pp. 453–472. ISSN: 0080-4630. DOI: 10.1098/rspa.1968.0029.

[84] J. Y. Lim, H. J. Donahue, and S. Y. Kim. “Strain Rate, Temperature, and Microstructure–Dependent Yield Stress of Poly(ethylene terephthalate)”. In: *Macromolecular Chemistry and Physics* 204.4 (2003), pp. 653–660. ISSN: 1022-1352. DOI: 10.1002/macp.200390033.

[85] S. Chattaraj, P. Pant, D. N. Pawaskar, and H. Nanavati. “How many network chains of a densely crosslinked glassy thermoset deform cooperatively at yield?” In: *Polymer* 82 (2016), pp. 305–318. DOI: 10.1016/j.polymer.2015.11.023.

[86] D. W. van Krevelen and K. T. Nijenhuis. *Properties of Polymers -Their Correlation with Chemical Structure their Numerical Estimation and Prediction from Additive Group Contributions*. 4th ed. Elsevier, 2009. ISBN: 978-0-08-054819-7.

[87] J. Chevalier, L. Brassart, F. Lani, C. Bailly, T. Pardoen, and X. P. Morelle. “Unveiling the nanoscale heterogeneity controlled deformation of thermosets (Pardeon 1)”. In: *Journal of Mechanics and Physics of Solids* 121 (2018), pp. 432–446. URL: 10.1016/j.jmps.2018.08.014.

[88] G. Z. Voyiadjis and A. Samadi-Dooki. “Constitutive modeling of large inelastic deformation of amorphous polymers: Free volume and shear transformation zone dynamics”. In: *Journal of Applied Physics* 119.22 (2016). DOI: 10.1063/1.4953355.

[89] A. Samadi-Dooki, L. Malekmotiei, and G. Z. Voyiadjis. “Characterizing shear transformation zones in polycarbonate using nanoindentation”. In: *Polymer* 82 (2016), pp. 238–245. DOI: 10.1016/j.polymer.2015.11.049.

[90] A. S. Argon. “Plastic deformation in metallic glasses”. In: *Acta Metallurgica* 27.1 (1979), pp. 47–58. ISSN: 00016160. DOI: 10.1016/0001-6160(79)90055-5.

[91] J. S. Langer. “Shear-transformation-zone theory of defomration in metallic glasses”. In: *Scripta Materialia* 54 (2006), pp. 375–379.

[92] A. S. Argon. “A theory for the low-temperature plastic deformation of glassy polymers”. In: *The Philosophical Magazine: A Journal of Theoretical Experimental and Applied Physics* (1973), pp. 839–865.

[93] A. S. Argon and M. I. Bessonov. “Plastic flow in glassy polymers”. In: *Polymer Engineering and Science* 17.3 (1977), pp. 174–182. ISSN: 0032-3888. DOI: 10.1002/pen.760170306.

[94] A. S. Argon. *The Physics of Deformation and Fracture of Polymers*. 2013. ISBN: 978-0-521-82184-1.

[95] S. Yamini and R. J. Young. “The mechanical properties of epoxy resins: Part 1: Mechanisms of plastic deformation”. In: *Journal of Material Science* 15 (1980), pp. 1814–1822.

[96] P. B. Bowden and S. Raha. “A molecular model for yield and flow in amorphous glassy polymers making use of a dislocation analogue”. In: *The Philosophical Magazine: A Journal of Theoretical Experimental and Applied Physics* 29 (1974), pp. 149–166.

[97] A. Thierry, R. J. Oxborough, and P. B. Bowden. “A molecular model for yield and flow in polymethylmethacrylate”. In: *Philosophical Magazine* 30.3 (1974), pp. 527–536. ISSN: 1478-6435. DOI: 10.1080/14786439808206578.

[98] R. W. K. Honeycombe. *The plastic deformation of metals*. 2nd ed. London, 1984.

[99] K. Chung and M.-G. Lee. *Basics of Continuum Plasticity*. Singapore: Springer Singapore, 2018. DOI: 10.1007/978-981-10-8306-8.

[100] T. W. Clyne and J. E. Campbell. *Testing of the Plastic Deformation of Metals*. Cambridge University Press, 2021. DOI: 10.1017/9781108943369.

[101] K. A. Kozielski, G. A. George, N. A. St John, and N. C. Billingham. “Kinetic studies by FT-NIR of the curing reactions of two glycidyl ether epoxy resins mixed with stoichiometric quantities of 4,4′ - DDS”. In: *High Performance Polymers* 6.3 (1994), pp. 263–286. ISSN: 0954-0083. DOI: 10.1088/0954-0083/6/3/010.

[102] C. M. Sahagun and S. E. Morgan. “Thermal control of nanostructure and molecular network development in epoxy-amine thermosets”. In: *ACS applied materials & interfaces* 4.2 (2012), pp. 564–572. DOI: 10.1021/am201515y.

[103] U. Braun, K. Brademann-Jock, and W. Stark. “Cure Monitoring of Epoxy Films by Heatable In Situ FTIR Analysis: Correlation to Composite Parts”. In: *Journal of Applied Polymer Science* Vol. 131, Issue 3 (2014), pp. 1–10.

[104] M. Müller-Pabel, J. A. Rodríguez Agudo, and M. Gude. “Measuring and understanding cure-dependent viscoelastic properties of epoxy resin: A review”. In: *Polymer Testing* 114 (2022), p. 107701. DOI: 10.1016/j.polymertesting.2022.107701.

[105] J. Lange, N. Altmann, C.T Kelly, and P.J Halley. “Understanding vitrification during cure of epoxy resins using dynamic scanning calorimetry and rheological techniques”. In: *Polymer* 41.15 (2000), pp. 5949–5955. DOI: 10.1016/S0032-3861(99)00758-2.

[106] M. Dornbusch, U. Christ, and R. Rasing. *Epoxidharze*. Hannover: Vincentz Network, 2015. ISBN: 9783748600138. DOI: 10.1515/9783748600138.

[107] B Ellis. *Chemistry and technology of Epoxy ResinsEpoxy Resins*. Springer_Science+Business Media, 1993. ISBN: 978-94-010-5302-0.

[108] P. J. Aspbury and W. C. Wake. “The supermolecular structures found in cured epoxy resins”. In: *British Polymer Journal* 11.1 (1979), pp. 17–27. ISSN: 0007-1641. DOI: 10.1002/PI.4980110105.

[109] K. Dušek, J. Pleštil, F. Lednický, and S. Luňák. “Are cured epoxy resins inhomogeneous?” In: *Polymer* 19.4 (1978), pp. 393–397. DOI: 10.1016/0032-3861(78)90243-4.

[110] V. B. Gupta, L. T. Drzal, W. W. Adams, and R. Omlor. “An electron microscopic study of the morphology of cured epoxy resin”. In: *Journal of Materials Science* 20.10 (1985), pp. 3439–3452. ISSN: 0022-2461. DOI: 10.1007/BF01113751.

[111] T. Takahama and P. H. Geil. “Structural inhomogeneities of cured epoxy resins”. In: *Die Makromolekulare Chemie, Rapid Communications* 3.6 (1982), pp. 389–394. ISSN: 0173-2803. DOI: 10.1002/marc.1982.030030603.

[112] L. M. Bogdanova, I. M. Belgovskii, V. I. Irzhak, and B. A. Rosenberg. "On the problem of structural microinhomogeneity of epoxy network polymers". In: *Polymer Bulletin* 4.1-2 (1981), pp. 119–125. ISSN: 0170-0839. DOI: 10.1007/BF01045249.

[113] U. T. Kreibich and R. Schmid. "Inhomogeneities in epoxy resin networks". In: *Journal of Polymer Science Part C: Polymer Symposia* 53.1 (1975), pp. 177–185. ISSN: 04492994. DOI: 10.1002/polc.5070530122.

[114] J. Duchet and J. P. Pascault. "Do epoxy–amine networks become inhomogeneous at the nanometric scale?" In: *Journal of Polymer Science Part B: Polymer Physics* 41.20 (2003), pp. 2422–2432. ISSN: 08876266. DOI: 10.1002/POLB.10585.

[115] X. Gu, T. Nguyen, M. Oudina, D. Martin, B. Kidah, J. Jasmin, A. Rezig, L. Sung, E. Byrd, J. W. Martin, D. L. Ho, and Y. C. Jean. "Microstructure and morphology of amine-cured epoxy coatings before and after outdoor exposures—An AFM study". In: *Journal of Coatings Technology and Research* 2.7 (2005), pp. 547–556. ISSN: 1547-0091. DOI: 10.1007/s11998-005-0014-x.

[116] H. Kishi, T. Naitou, S. Matsuda, A. Murakami, Y. Muraji, and Y. Nakagawa. "Mechanical properties and inhomogeneous nanostructures of dicyandiamide–cured epoxy resins". In: *Journal of Polymer Science Part B: Polymer Physics* 45.12 (2007), pp. 1425–1434. ISSN: 08876266. DOI: 10.1002/polb.21170.

[117] R. Lovell and A. H. Windle. "WAXS investigation of local structure in epoxy networks". In: *Polymer* 31.4 (1990), pp. 593–601. DOI: 10.1016/0032-3861(90)90274-3.

[118] J. Feng, K. R. Berger, and E. P. Douglas. "Water vapor transport in liquid crystalline and non-liquid crystalline epoxies". In: *Journal of Materials Science* 39.10 (2004), pp. 3413–3423. ISSN: 0022-2461. DOI: 10.1023/B:JMSC.0000026944.85440.f3.

[119] J. Mijović and J. A. Koutsky. "Correlation between nodular morphology and fracture properties of cured epoxy resins". In: *Polymer* 20.9 (1979), pp. 1095–1107. DOI: 10.1016/0032-3861(79)90301-X.

[120] A. Shundo, S. Yamamoto, and K. Tanaka. "Network Formation and Physical Properties of Epoxy Resins for Future Practical Applications". In: *JACS Au* 2.7 (2022), pp. 1522–1542. DOI: 10.1021/jacsau.2c00120.

[121] C. Li and A. Strachan. “Free volume evolution in the process of epoxy curing and its effect on mechanical properties”. In: *Polymer* 97 (2016), pp. 456–464. DOI: 10.1016/j.polymer.2016.05.059.

[122] H. Kim and J. Choi. “Subcontinuum Interpretation of Mechanical Behavior for Cross-Linked Epoxy Networks”. In: *Macromolecules* 55.14 (2022), pp. 5916–5925. DOI: 10.1021/acs.macromol.2c00593.

[123] W. W. Feng, K. L. Reifsnider, G. P. Sendeckyj, T. T. Chiao, W. Steve Johnson, G. L. Rodericks, W. W. Stinchcomb, L. de Vore, and D. L. Hunston. “Composite Interlaminar Fracture: Effect of Matrix Fracture Energy”. In: *Journal of Composites Technology and Research* 6.4 (1984), p. 176. ISSN: 08846804. DOI: 10.1520/CTR10842J.

[124] R. J. Young. “Strength and toughness”. In: *Comprehensive Polymer Science: the Synthesis, Characterization, Reactions & Applications of Polymers* 2 (1989), pp. 511–532.

[125] L. D. Landau, E. M. Lifshitz, J. B. Sykes, W. H. Reid, and Ellis H. Dill. “Theory of Elasticity: Vol. 7 of Course of Theoretical Physics”. In: *Physics Today* 13.7 (1960), pp. 44–46. ISSN: 0031-9228. DOI: 10.1063/1.3057037.

[126] M. Demleitner, Hübner, F. Mainz, A., H. Ruckdäschel, V. Altstädt, L. Michely, and A. Rios de Anda. “Influence of network structure determined by Time-domain 1H Double Quantum NMR on the creep properties of non-stoichiometric epoxy-amine resins aimed for chemical anchoring applications”. In: *Polymer* 286 (2023), p. 126373. DOI: 10.1016/j.polymer.2023.126373.

[127] S. Yamini and R. J. Young. “The mechanical properties of epoxy resins: Part 2: Effect of plastic deformation upon crack propagation”. In: *Journal of Materials Science* 15.7 (1980), pp. 1823–1831. ISSN: 0022-2461. DOI: 10.1007/BF00550603.

[128] B. Fiedler, T. Hobbiebrunken, M. Hojo, and K. Schulte, eds. *Influence of stress state and temperature on the strength of epoxy resins*. Vol. 3. 2271-2275. 2005.

[129] Z. Bazant and E. P. Chen. “Scaling of structural failure”. In: *Appl Mech Rev* Vol. 50, No. 10 (1997), pp. 593–627.

[130] J. Misumi, R. Ganesh, S. Subramani Sockalingam, J. Gillespie Jr, Jun Misumi, Raja Ganesh, Subramani Sockalingam, and John W. Gillespie. "Experimental characterization of tensile properties of epoxy resin by using micro-fiber specimens". In: *Journal of Reinforced Plastics and Composites* 35.24 (2016), pp. 1792–1801. DOI: 10.1177/0731684416669924.

[131] A. T. Detwiler and A. J. Lesser. "Aspects of network formation in glassy thermosets". In: *Journal of Applied Polymer Science* 117.2 (2010), pp. 1021–1034. ISSN: 0021-8995. DOI: 10.1002/app.31681.

[132] M. Harada, M. Morimoto, and M. Ochi. "Influence of network chain orientation on the mechanical property of epoxy resin filled with silica particles". In: *Journal of Applied Polymer Science* 87.Vol. 87 // 5 (2003), pp. 787–794. DOI: 10.1002/app.11454.

[133] A. I. Leonov. "A theory of necking in semi-crystalline polymers". In: *International Journal of Solids and Structures* 39.24 (2002), pp. 5913–5926. ISSN: 00207683. DOI: 10.1016/S0020-7683(02)00478-X.

[134] D. A. Skoog, F. J. Holler, and S. R. Crouch. *Principles of instrumental analysis*. 7. edition. Boston, MA: Cengage Learning, 2018. ISBN: 9781305577213.

[135] M. W. Sigrist. *Laser: Theorie, Typen und Anwendungen // Laser Theorie, Typen und Anwendungen*. 8. Auflage. Springer eBook Collection. Berlin, Heidelberg: Springer Berlin Heidelberg and Springer Spektrum, 2018. ISBN: 978-3-662-57515-4. DOI: 10.1007/978-3-662-57515-4.

[136] P. K. Mallick. *Fundamentals of Molecular Spectroscopy*. Singapore: Springer Nature Singapore, 2023. DOI: 10.1007/978-981-99-0791-5.

[137] P. Larkin. *Infrared and Raman spectroscopy: Principles and spectral interpretation*. 2nd ed. Amsterdam: Elsevier, 2018. ISBN: 978-0-12-804162-8. DOI: 10.1016/C2015-0-00806-1.

[138] G. G. Hoffmann. *Infrared and Raman Spectroscopy: Principles and Applications*. 1. Auflage. De Gruyter STEM. Berlin and Boston: de Gruyter, 2023. ISBN: 978-3-11-071755-6. DOI: 10.1515/9783110717556.

[139] R. M. Silverstein, G. C. Bassler, and T. C. Morrill. *Spectrometric identification of organic compounds*. 5. ed. New York: Wiley, 1991. ISBN: 0471634042.

[140] W. Demtröder. *Molekülphysik: Theoretische Grundlagen und experimentelle Methoden*. 2., überarb. und erw. Aufl. München: Oldenbourg, 2013. ISBN: 978-3-486-70678-9. DOI: 10.1524/9783486714890.

[141] J. A. Kerr, ed. *Molecular spectra and molecular structure: IV constants of diatomic molecules: K.P. Huber and G. Herzberg,* vol. 144. 1982. DOI: 10.1016/S0003-2670(01)95552-7.

[142] P. L. Polavarapu. *Vibrational spectra: Principles and applications with emphasis on optical activity*. 1st ed. Vol. 85. Studies in physical and theoretical chemistry. Amsterdam and New York: Elsevier, 1998. ISBN: 978-0-444-89599-8.

[143] T. Wolfram. *Applications of group theory to atoms, molecules, and solids*. Cambridge: Cambridge University Press, 2014. ISBN: 978-1-107-02852-4. DOI: 10.1017/CBO9781139236294.

[144] H. Haken and H. C. Wolf. *Molecular Physics and Elements of Quantum Chemistry: Introduction to Experiments and Theory*. Second Enlarged Edition. Advanced Texts in Physics. Berlin and Heidelberg: Springer, 2004. ISBN: 9783662088203. DOI: 10.1007/978-3-662-08820-3.

[145] J. E. Huheey and B. Reuter. *Anorganische Chemie: Prinzipien von Struktur und Reaktivität*. Berlin: de Gruyter, 1988. ISBN: 3-11-008163-6.

[146] P. R. Griffiths and J. A. Haseth. *Fourier Transform Infrared Spectrometry*. 2nd ed. John Wiley & Sons, 2007. ISBN: 9780470106310. DOI: 10.1002/047010631X.

[147] J. J. Laserna. *Modern techniques in Raman spectroscopy*. Chichester: Wiley, 1996. ISBN: 978-0-471-95774-4.

[148] C. N. Banwell and E. M. McCash. *Fundamentals of molecular spectroscopy*. 4. ed. London: McGraw-Hill, 1994. ISBN: 0-07-707976-0.

[149] D. K. Singh, M. Pradhan, and A. Materny. *Modern techniques of spectroscopy: Basics, instrumentation, and applications*. 1st ed. 2021. Vol. volume 13. Springer eBook Collection. Singapore: Springer, 2021. ISBN: 978-981-33-6084-6. DOI: 10.1007/978-981-33-6084-6.

[150] J. L. Koenig. *Spectroscopy of Polymers*. 2nd ed. Elsevier, 1999. ISBN: 978-0-444-10031-3.

[151] M. Tanaka and R. J. Young. "Review Polarised Raman spectroscopy for the study of molecular orientation distributions in polymers". In: *Journal of Materials Science* 41.3 (2006), pp. 963–991. ISSN: 0022-2461. DOI: 10.1007/s10853-006-6595-7.

[152] T. Miyazawa, K. Fukushima, and Y. Ideguchi. "Molecular Vibrations and Structure of High Polymers. III. Polarized Infrared Spectra, Normal Vibrations, and Helical Conformation of Polyethylene Glycol". In: *The Journal of Chemical Physics* 37.12 (1962), pp. 2764–2776. ISSN: 0021-9606. DOI: 10.1063/1.1733103.

[153] T. Scherzer. "Rheo-optical FTIR spectroscopy of epoxy resins". In: *Journal of Applied Polymer Science* 58.3 (1995), pp. 501–514. ISSN: 0021-8995. DOI: 10.1002/app.1995.070580303.

[154] J. Mittelhaus, J. Jacobs, S. Bhusare, N. Pournoori, M. Isakov, T. Salminen, H. Schmalz, G. Mohanty, E. Sarlin, and B. Fiedler. "Performing polarized Raman and Digital Image Correlation analysis to understand the increased ductility of microscale epoxy materials". In: *Journal of Polymer Science* 63.9 (2025), pp. 2091–2101. DOI: 10.1002/pol.20240971.

[155] R. M. Badger. "A Relation Between Internuclear Distances and Bond Force Constants". In: *The Journal of Chemical Physics* 2.3 (1934), pp. 128–131. ISSN: 0021-9606. DOI: 10.1063/1.1749433.

[156] R. S. Bhatta, P. P. Iyer, A. Dhinojwala, and M. Tsige. "A brief review of Badger–Bauer rule and its validation from a first-principles approach". In: *Modern Physics Letters B* 28.29 (2014). ISSN: 0217-9849. DOI: 10.1142/S0217984914300142.

[157] L. Jensovsky. "Über die Badgersche Regel". In: *Zeitschrift für Chemie* 11.2 (1962).

[158] Y. L. Lee, R. S. Bretzlaff, and R. P. Wool. "Fourier-Transform Infrared Studies of Polypropylene during Mechanical Deformation". In: *Journal of Polymer Science: Part B: Polymer Physics* 22 (1984), pp. 681–698.

[159] A. Doblies, B. Fiedler, T. Würger, E. Schill, H. R. Meißner, and C. Feiler. "Mechanical Degradation Estimation of Thermosets by Peak Shift Assessment: General Approach using Infrared Spectroscopy and Atomistic Simulations". In: *Polymer* 221 (2021), p. 123585. DOI: 10.1016/j.polymer.2021.123585.

[160] P. Hobza and Z. Havlas. “Blue-Shifting Hydrogen Bonds”. In: *Chemical reviews* 100.11 (2000), pp. 4253–4264. DOI: 10.1021/cr990050q.

[161] X. Li, L. Liu, and H. B. Schlegel. “On the physical origin of blue-shifted hydrogen bonds”. In: *Journal of the American Chemical Society* 124.32 (2002), pp. 9639–9647. ISSN: 0002-7863. DOI: 10.1021/ja020213j.

[162] A. Masunov, J. J. Dannenberg, and R. H. Contreras. “C−H Bond-Shortening upon Hydrogen Bond Formation: Influence of an Electric Field”. In: *The Journal of Physical Chemistry A* 105.19 (2001), pp. 4737–4740. ISSN: 1089-5639. DOI: 10.1021/jp0043470.

[163] B. Reimann, K. Buchhold, S. Vaupel, B. Brutschy, Z. Havlas, V. Špirko, and P. Hobza. “Improper, Blue-Shifting Hydrogen Bond between Fluorobenzene and Fluoroform”. In: *The Journal of Physical Chemistry A* 105.23 (2001), pp. 5560–5566. ISSN: 1089-5639. DOI: 10.1021/jp003726q.

[164] K. Mizuno, S. Imafuji, T. Ochi, T. Ohta, and S. Maeda. “Hydration of the CH Groups in Dimethyl Sulfoxide Probed by NMR and IR”. In: *The Journal of Physical Chemistry B* 104.47 (2000), pp. 11001–11005. ISSN: 1520-6106. DOI: 10.1021/jp001079x.

[165] B. Reimann, K. Buchhold, S. Vaupel, and B. Brutschy. “Blue-Shift in the Frequencies of the CH Stretches of Chloro- and Fluoroform Induced by C–H...p Hydrogen Bonding with Benzene Derivatives: the Influence of Electron Donating and Withdrawing Substituents”. In: *Zeitschrift für Physikalische Chemie* 215.6 (2001). ISSN: 0942-9352. DOI: 10.1524/zpch.2001.215.6.777.

[166] S. Y. Liu and C. E. Dykstra. “A theory of vibrational transition frequency shifts due to hydrogen bonding”. In: *The Journal of Physical Chemistry* 90.14 (1986), pp. 3097–3103. ISSN: 0022-3654. DOI: 10.1021/j100405a013.

[167] C. A. Parish and C. E. Dykstra. “Partially coupled electrical model of vibrational frequency shifts in weak atom-diatomic and diatomic-diatomic complexes”. In: *The Journal of Physical Chemistry* 97.37 (1993), pp. 9374–9379. ISSN: 0022-3654. DOI: 10.1021/j100139a020.

[168] C. Billaud, M. Vandeuren, R. Legras, and V. Carlier. “Quantitative Analysis of Epoxy Resin Cure Reaction: A Study by Near-Infrared Spectroscopy”. In: *Applied Spectroscopy* 56.11 (2002), pp. 1413–1421. ISSN: 0003-7028. DOI: 10.1366/00037020260377706.

[169] R. Unger, U. Braun, J. Fankhänel, B. Daum, B. Arash, and R. Rolfes. "Molecular modelling of epoxy resin crosslinking experimentally validated by near-infrared spectroscopy". In: *Computational Materials Science* 161 (2019), pp. 223–235. ISSN: 09270256. DOI: 10.1016/j.commatsci.2019.01.054.

[170] N. Poisson, G. Lachenal, and H. Sautereau. "Near- and mid-infrared spectroscopy studies of an epoxy reactive system". In: *Vibrational Spectroscopy* 12.12 // 2 (1996), pp. 237–247. DOI: 10.1016/0924-2031(96)00027-6.

[171] M. G. González, J. C. Cabanelas, and J. Baselga. "Applications of FTIR on Epoxy Resins - Identification, Monitoring the Curing Process, Phase Separation and Water Uptake". In: (2012). DOI: 10.5772/36323.

[172] H. L. Friedman. "Kinetics of thermal degradation of char–forming plastics from thermogravimetry. Application to a phenolic plastic". In: *Journal of Polymer Science Part C: Polymer Symposia* 6.1 (1964), pp. 183–195. ISSN: 04492994. DOI: 10.1002/polc.5070060121.

[173] M. Walter, M. Neubacher, and B. Fiedler. "Using thermokinetic methods to enhance properties of epoxy resins with amino acids as biobased curing agents by achieving full crosslinking". In: *Scientific reports* 14.1 (2024), p. 4367. DOI: 10.1038/s41598-024-54484-0.

[174] DIN EN ISO 11357-2. "Kunststoffe - Dynamische Differenzkalorimetrie DSC - Teil 2: Bestimmung der Glasübergangstemperatur und der Glasübergangsstufenhöhe". In: (2020). DOI: 10.31030/3127571.

[175] E. Jones and M. Iadicola. "A Good Practices Guide for Digital Image Correlation". In: *International Digital Image Correlation Society* (2018). DOI: 10.32720/idics/gpg.ed1.

[176] Bernhard Ilschner. *Hochtemperatur-Plastizität: Warmfestigkeit und Warmverformbarkeit metallischer und nichtmetallischer Werkstoffe*. Vol. 23. Reine und angewandte Metallkunde in Einzeldarstellungen. Berlin and Heidelberg: Springer, 1973. ISBN: 9780387059662.

[177] J. M. Chalmes, M. W. Mackenzie, and H. A. Willis. "FTIR spectroscopic studies of isotactic polypropylene films under stress". In: *Spectrochimica Acta* 47A.12 (1991), pp. 1677–1683.

[178] R. P. Wool. "Infrared Studies of Deformation in Semicrystalline Polymers". In: *Polymer Engineering and Science* 20.12 (1980), pp. 805–815.

[179] R. P. Wool. “Measurements of infrared frequency shifts in stressed polymers”. In: *Journal of Polymer Science: Part B: Polymer Physics* 19 (1981), pp. 449–457. DOI: 10.1002/pol.1981.180190305.

[180] M. Bradley. “Curve fitting in Raman and IR spectroscopy: basic theory of line shapes and Application”. In: *Thermo Fisher Scientific* Note 50733 (2007).

[181] M. Bradley. “Lineshapes in IR and Raman Spectroscopy: A Primer”. In: *Spectroscopy* 30.11 (2015), pp. 42–46.

[182] P. R. Griffiths. *Introduction to Vibrational Spectroscopy: Introduction to the Theory and Practice of Vibrational Spectroscopy: Artikel aus Handbook of Vibrational Spectroscopy*. 2006. ISBN: 9780471988472.

[183] J. Kiusalaas. “Numerical Methods in Engineering with Python 3”. In: (2014). DOI: 10.1017/CBO9781139523899.

[184] D. W. Marquardt. “An Algorithm for Least-Squares Estimation of Nonlinear Parameters”. In: *Journal of the Society for Industrial and Applied Mathematics* 11.2 (1963), pp. 431–441. ISSN: 0368-4245. DOI: 10.1137/0111030.

[185] X. Liao, M. Dulle, Souza E S., J. M., Wehrspohn, R. B., S. Agarwal, S. Förster, H. Hou, P. Smith, and A. Greiner. “High strength in combination with high toughness in robust and sustainable polymeric materials”. In: *Science* 366.6471 (2019), pp. 1376–1379. DOI: 10.1126/science.aay9033.

[186] D. Bryce, J. Thomason, and L. Yang. “Micromechanical and spectroscopic characterisation of the curing performance of epoxy resins in the microbond test: 41st Risø International Symposium on Materials Science”. In: *IOP Conf. Series: Materials Science and Engineering* 942 (2020). DOI: 10.1088/1757-899X/942/1/012019.

[187] J. Mittelhaus, P. Röttger, E. Schill, J. Jacobs, and B. Fiedler. “Investigation of the ductile deformation potential of microscale epoxy materials”. In: *Polymer Testing* 128 (2023), p. 108217. DOI: 10.1016/j.polymertesting.2023.108217.

[188] B. Fiedler, M. Hojo, S. Ochiai, K. Schulte, and M. Ando. “Failure behavior of an epoxy matrix under different kinds of static loading”. In: *Composites Science and Technology* Vol. 61 (2001) (2001), pp. 1615–1624. URL: 10.1016/S0266-3538(01)00057-4.

[189] J. Drummer, D. Gibhardt, J. Körbelin, and B. Fiedler. "General influence of the environmental temperature on the matrix strength under tensile and compressive loading - a comprehensive study on high performance matrices". In: *Composites Science and Technology* 230.Part 2 (2022). DOI: 10.1016/j.compscitech.2022.109486.

[190] H.G.H. van Melick, L. E. Govaert, and H.E.H. Meijer. "On the origin of strain hardening in glassy polymers". In: *Polymer* 44.8 (2003), pp. 2493–2502. DOI: 10.1016/S0032-3861(03)00112-5.

[191] R. N. Haward. "Strain hardening of thermoplastics". In: *Macromolecules* 26 (1993), pp. 5860–5869. DOI: 10.1021/ma00074a006.

[192] C. Tian, R. Xiao, and J. Guo. "An Experimental Study on Strain Hardening of Amorphous Thermosets: Effect of Temperature, Strain Rate, and Network Density". In: *Journal of Applied Mechanics* 85.10 (2018). ISSN: 0021-8936. DOI: 10.1115/1.4040692.

[193] K. W. Thomson and L. J. Broutman. "Strain softening in an epoxy resin". In: *Journal of Materials Science* 17.9 (1982), pp. 2700–2708. ISSN: 0022-2461. DOI: 10.1007/BF00543907.

[194] S. Yamini and R. J. Young. "Stability of crack propagation in epoxy resins". In: *Polymer* 18.10 (1977), pp. 1075–1080. DOI: 10.1016/0032-3861(77)90016-7.

[195] W. Retting. *Mechanik der Kunststoffe: Die mechanischen Eigenschaften von Polymer-Werkstoffen*. München: Carl Hanser, 1992.

[196] D. Lin-Vien, Colthup N. B., W. G. Fateley, and J. G. Grasselli. *The Handbook of Infrared and Raman Characteristic Frequencies of Organic Molecules*. Bosten: Academic Press, 1991. ISBN: 9780080571164.

[197] N. Colthup and Daly, L.H. . Wiberley, S. E. *Introduction to Infrared and Raman Spectroscopy*. 3rd ed. Academic Press, 1990. DOI: 10.1016/C2009-0-21628-X.

[198] M. Sabu, E. Bementa, Y. Jaya Vinse Ruban, and S. Ginil Mon. "A novel analysis of the dielectric properties of hybrid epoxy composites". In: *Advanced Composites and Hybrid Materials* 3.3 (2020), pp. 325–335. ISSN: 2522-0128. DOI: 10.1007/s42114-020-00166-0.

[199] L. Wang, S. Liu, T. Wang, and D. Sun. "Effect of poly(oxypropylene)diamine adsorption on hydration and dispersion of montmorillonite particles in aqueous solution". In: *Colloids and Surfaces A: Physicochemical and Engineering Aspects* 381.1-3 (2011), pp. 41–47. ISSN: 09277757. DOI: 10.1016/j.colsurfa.2011.03.008.

[200] S. C. Lin, B. J. Bulkin, and E. M. Pearce. "Epoxy resins. III. Application of fourier transform IR to degradation studies of epoxy systems". In: *Journal of Polymer Science: Polymer Chemistry Edition* 17.10 (1979), pp. 3121–3148. ISSN: 0360-6376. DOI: 10.1002/pol.1979.170171006.

[201] C. Hemalatha. "FT-Raman, FTIR Spectra and Normal Co-Ordinate Analysis of Isoquinoline". In: *International Journal of Physics and Applications* 3.1 (2011), pp. 83–90.

[202] C. D. Zangmeister, U. Bertocci, C. R. Beauchamp, and G. R. Stafford. "In situ stress measurements during the electrochemical adsorption/desorption of self-assembled monolayers". In: *Electrochimica Acta* 53.23 (2008), pp. 6778–6786. ISSN: 00134686. DOI: 10.1016/j.electacta.2007.12.013.

[203] J. Coates. "Interpretation of Infrared Spectra, A Practical Approach". In: *Encyclopedia of Analytical Chemistry* (2000), pp. 10815–10837. DOI: 10.1002/9780470027318.a5606.

[204] H. Sukanto, W. W. Raharjo, D. Ariawan, and J. Triyono. "Investigation of cycloaliphatic amine-cured bisphenol-A epoxy resin under quenching treatment and the effect on its carbon fiber composite lamination strength". In: *Journal of the Mechanical Behavior of Materials* 32.1 (2023). DOI: 10.1515/jmbm-2022-0266.

[205] Z. Wu, S. Li, M. Liu, Z. Wang, and X. Liu. "Liquid oxygen compatible epoxy resin: modification and characterization". In: *RSC advances* 5.15 (2015), pp. 11325–11333. DOI: 10.1039/c4ra14100h.

[206] S. Yoshida. "Quantitative evaluation of an epoxy resin dispersion by infrared spectroscopy". In: *Polymer Journal* 46.7 (2014), pp. 430–434. ISSN: 0032-3896. DOI: 10.1038/pj.2014.15.

[207] L. Karpati, M. Fejer, D. Kalocsai, J. Molnar, and V. Vargha. "Synthesis and characterization of isophorondiamine based epoxy hardeners from aminolysis of PET". In: *eXPress Polymer Letters* 13.7 (2019), pp. 618–631. ISSN: 1788618X. DOI: 10.3144/expresspolymlett.2019.52.

[208] T. Arunkumar and S. Ramachandran. “Surface coating and characterisation of polyurea for liquid storage”. In: *International Journal of Ambient Energy* 38.8 (2017), pp. 781–787. ISSN: 0143-0750. DOI: 10.1080/01430750.2016.1222966.

[209] A. Doblies, B. Boll, and B. Fiedler. “Prediction of Thermal Exposure and Mechanical Behavior of Epoxy Resin using Artificial Neural Networks and Fourier Transform Infrared Spectroscopy”. In: *Polymers* 11(2),363 (19 February 2019). URL: https://doi.org/10.3390/polym11020363.

[210] S.-I. Morita and Y. Ozaki. “Pattern recognitions of band shifting, overlapping, and broadening using global phase description derived from generalized two-dimensional correlation spectroscopy”. In: *Applied Spectroscopy* 56.4 (2002), pp. 501–508. DOI: 10.1366/00037020219549.

[211] J. Mittelhaus, J. Konrad, J. Jacobs, P. Röttger, R. Meißner, and B. Fiedler. “Load-induced shear band formation in microscale epoxy materials”. In: *Journal of Polymer Science* 63.10 (2025), pp. 2174–2186. DOI: 10.1002/pol.20240971.

[212] R. M. Badger. “The Relation Between Internuclear Distances and the Force Constants of Diatomic Molecules”. In: *Physical Review* 48.3 (1935), pp. 284–285. ISSN: 0031-899X. DOI: 10.1103/PhysRev.48.284.2.

[213] A. A. Profit, V. Felsen, J. Chinwong, E.-R. E. Mojica, and R. Z. B. Desamero. “Evidence of p-stacking interactions in the self-assembly of hIAPP(22-29)”. In: *Proteins* 81.4 (2013), pp. 690–703. DOI: 10.1002/prot.24229..

[214] E. M. Cabaleiro-Lago and J. Rodríguez-Otero. “On the Nature of s-s, s-p, and p-p Stacking in Extended Systems”. In: *ACS omega* 3.8 (2018), pp. 9348–9359. DOI: 10.1021/acsomega.8b01339.

[215] S. K. Burley and G. A. Petsko. “Aromatic-aromatic interaction: a mechanism of protein structure stabilization”. In: *Science* 229.4708 (1985), pp. 23–28. DOI: 10.1126/science.3892686.

[216] C. A. Hunter, K. R. Lawson, J. Perkins, and C. J. Urch. “Aromatic interactions”. In: *Journal of the Chemical Society, Perkin Transactions 2* 5 (2001), pp. 651–669. ISSN: 1472779X. DOI: 10.1039/b008495f.

[217] A. Farrokhzadeh, A. R. Modarresi-Alam, F. B. Akher, and A. Ebrahimi. "A theoretical study of p-stacking interactions in C-substituted tetrazoles". In: *Journal of molecular graphics & modelling* 67 (2016), pp. 85–93. DOI: 10.1016/j.jmgm.2016.05.005.

[218] P. Laurikainen, S. Bhusare, G. Mohanty, and E. Sarlin. "Length-scale discrepancy in the properties of epoxy resin specimens". In: *Polymer* 283 (2023), p. 126148. DOI: 10.1016/j.polymer.2023.126148.

[219] M. Fischer. "Properties and failure of polymes with tailored distances between crosslinks". In: *Macromolecules: Synthesis, Order and Advanced Properties* 100/1 (1992), pp. 313–355. DOI: 10.1007/BFb0051639.

[220] R. Ikeda, B. Chase, and N. Everall, eds. *Basics of Orientation Measurements in Infrared and Raman Spectroscopy*. Handbook of Vibrational Spectroscopy. John Wiley & Sons/American Cancer Society, 2006. ISBN: 9780471988472. DOI: 10.1002/0470027320.s6102.

[221] R. E. Lyon, K. E. Chike, and S. M. Angel. "In situ cure monitoring of epoxy resins using fiber–optic Raman spectroscopy". In: *Journal of Applied Polymer Science* 53.13 (1994), pp. 1805–1812. ISSN: 0021-8995. DOI: 10.1002/app.1994.070531310.

[222] A. F. Betancur, A. García, and F. R. Pérez. "Thermal stability and chemical analysis of hybrid materials reinforced with graphene oxide". In: *Journal of Physics: Conference Series* 1219.1 (2019), p. 012003. ISSN: 1742-6588. DOI: 10.1088/1742-6596/1219/1/012003.

[223] J. Konrad, R. H. Meißner, E. Bitzek, and D. Zahn. "A Molecular Simulation Approach to Bond Reorganization in Epoxy Resins: From Curing to Deformation and Fracture". In: *ACS Polymers Au* (2021). ISSN: 2694-2453. DOI: 10.1021/acspolymersau.1c00016.

Appendix

Figure 1: Microscopic image of a punched type A sample with a thickness of 30 µm.

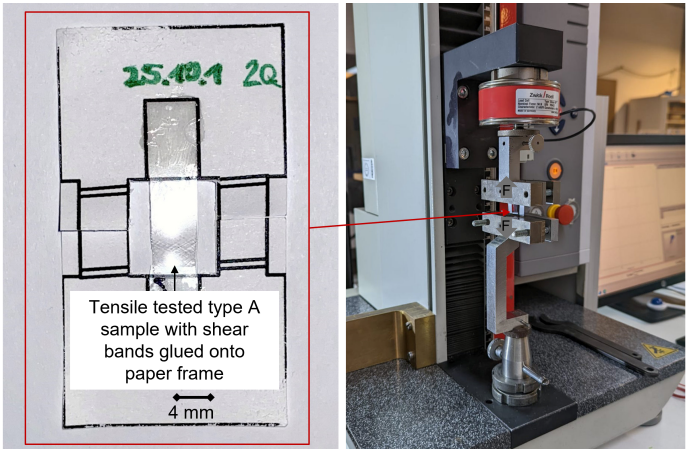

Figure 2: Photo images of a type A sample glued onto a paper frame (left) and both clamped in a Zwick Z2.5 tensile machine (right).

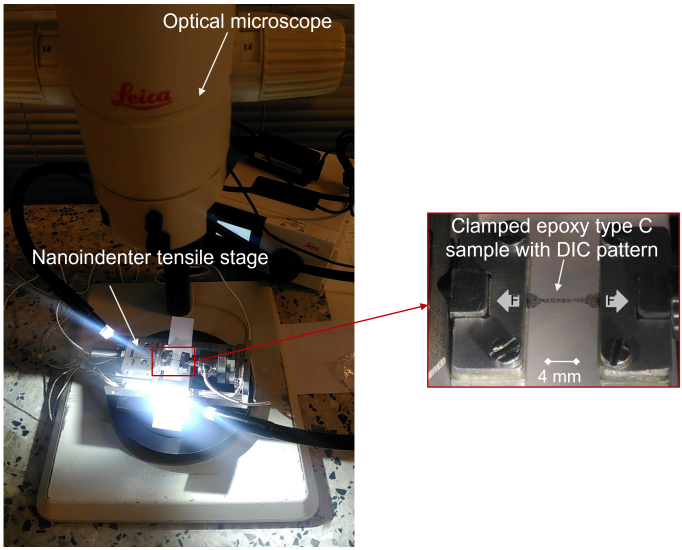

Figure 3: Photos of the DIC setup for a type C sample are shown. The optical microscope with the nanoindenter tensile stage are shown (left) and a clamped type C sample with DIC pattern (right).

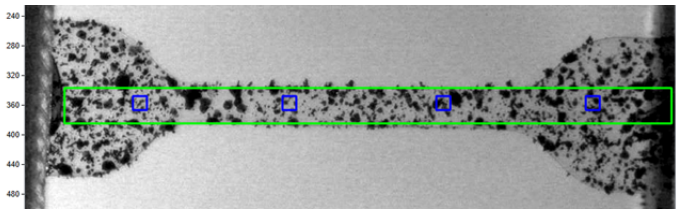

Figure 4: Clamped DIC tape C sample with a thickness of 30 µm and a suitable speckle pattern. An illustration of the smallest used subset size of 19 pixels is shown: example subsets are denoted by blue rectangles and the green rectangle indicates the area of interest in the DIC analysis.

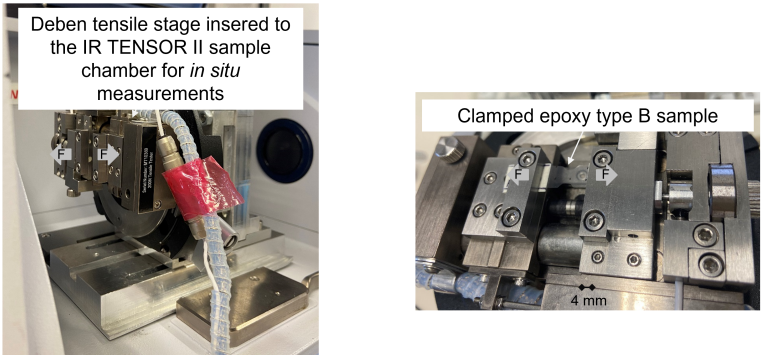

Figure 5: Photos of the *in situ* test setup are shown. The Deben tensile stage positioned in the TENSOR II chamber are shown (left) and a clamped type B sample with the Deben tensile stage (right) are shown.

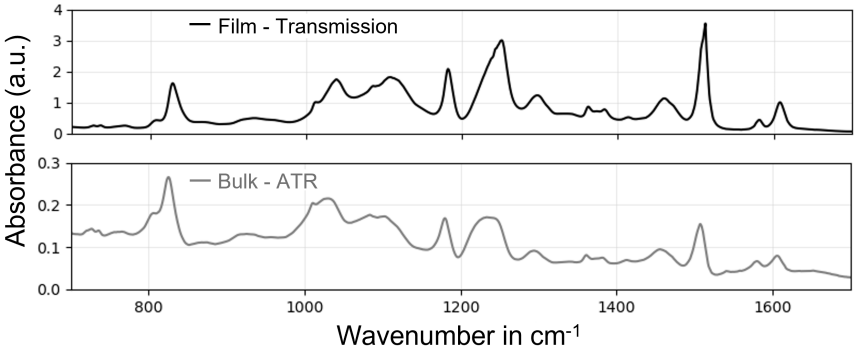

Figure 6: In transmission mode recorded spectrum of a film sample with a thickness of 30 µm (top) and ATR spectrum of a bulk specimen (bottom). No chemical differences can be found between the spectra.

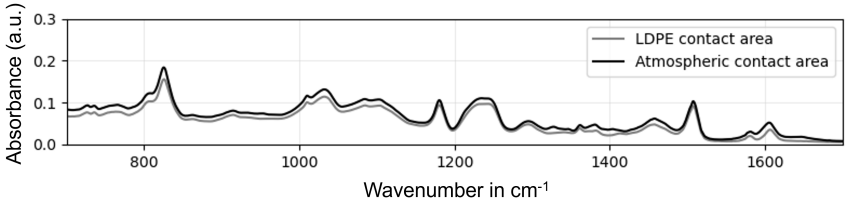

Figure 7: The ATR spectra of a film with a thickness of 100 µm made with a rackel on the LDPE carrier foil is shown. One surface of the epoxy film was in contact with the atmospheric environment (black spectrum) and the other surface with the LDPE carrier foil (gray spectrum) during the curing process. Both spectra are averaged from 3 spectra, recorded at three different film positions on both surfaces after curing. No chemical differences can be found between the spectra.

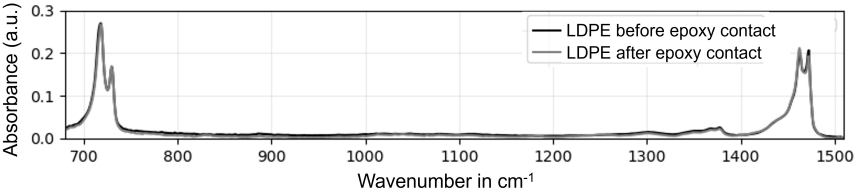

Figure 8: The ATR spectra of the LDPE carrier foil is shown before epoxy contact (black) and after epoxy contact (gray) during the epoxy film manufacturing process of an epoxy film with a thickness of 50 µm.

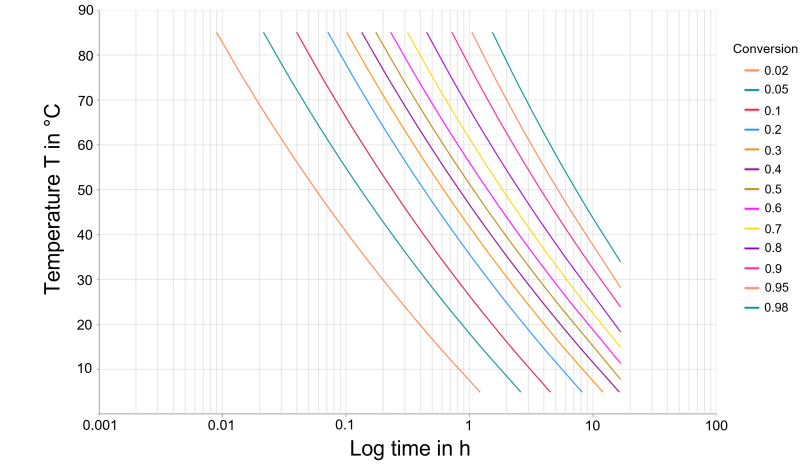

Figure 9: With NETZSCH Kinetics Neo software and DSC curing measurements determined Time-Temperature-Transition (TTT) diagram for the DGEBA epoxy system. The time axis is plotted in log scale.

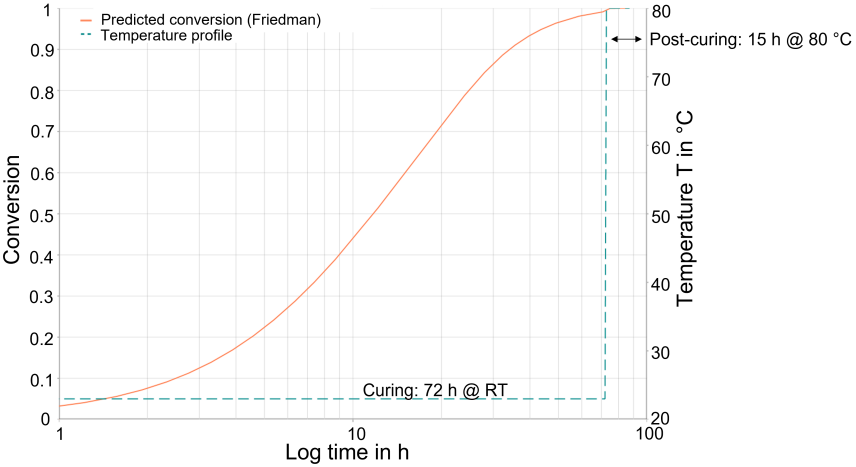

Figure 10: With NETZSCH Kinetics Neo software and DSC curing measurements predicted conservation for the selected and to the DGEBA epoxy film samples applied (post-)curing process. The Friedman model is used for the prediction. The time axis is plotted in log scale.

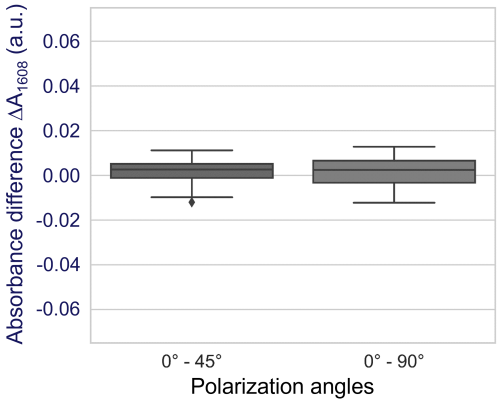

Figure 11: Absorbance difference $\Delta\tilde{\nu}_{1608}$ for 0°, 45°and 90°polarization angle of an as-produced epoxy type A sample in the initial state before mechanical testing.

Table 1: Mechanical parameters (tensile strengths (UTS), Young's modulus (E) and elongation at break (ϵ_b)) of epoxy films of type A with different thicknesses and epoxy bulk samples determined in a tensile test using a Zwick Z2.5 and Z 10.0 with a crosshead speed of 1 mm/min at room temperature.

	Film thickness d of type A sample in µm				Bulk ($d = 2000$ µm)
	15	30	50	100	
$UTS_{\parallel}$ in MPa	63.1 ± 3.5	69.8 ± 1.0	71.2 ± 1.1	70.4 ± 0.4	78.9 ± 1.1
$UTS_{\perp}$ in MPa	61.2 ± 6.2	68.8 ± 2.7	69.4 ± 0.7	69.5 ± 1.2	
$E_{\parallel}$ in MPa	2642 ± 201	3043 ± 170	3242 ± 133	3024 ± 122	2708 ± 33
$E_{\perp}$ in MPa	2646 ± 385	3153 ± 168	3135 ± 270	3032 ± 68	
$\epsilon_{\parallel}$ in %	8.0 ± 3.7	7.5 ± 2.9	11.5 ± 6.0	20.7 ± 8.0	8.4 ± 1.2
$\epsilon_{\perp}$ in %	6.1 ± 3.9	6.5 ± 3.6	6.7 ± 2.1	10.6 ± 4.9	

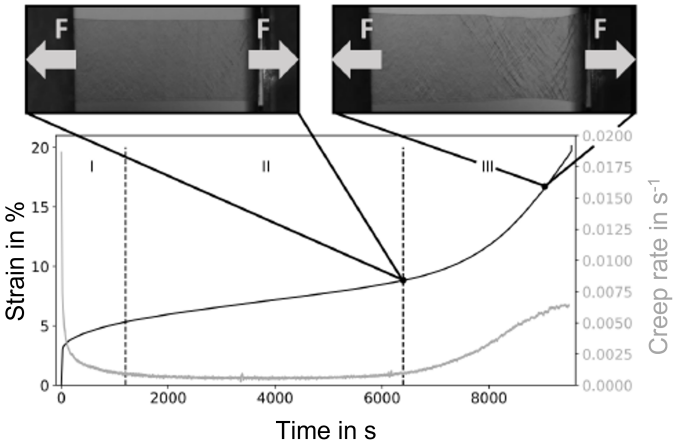

Figure 12: Strain-time curve and a creep-rate-time curve of type A film sample with a thickness of 30 µm. The stress level was at 70 % UTS (testing machine Z 2.5). Two photos were taken during the creep test to track the shear band formation.

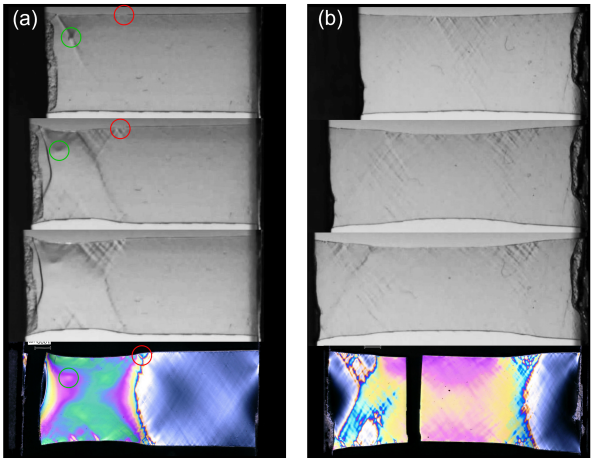

Figure 13: Type A sample with a thickness of 100 µm with photos taken over time during a creep test and with a stress-optical image after failure (from top to bottom). (a) Sample with central necking and creep tested at 80 % UTS and (b) Sample creep tested at 70 % UTS with necking at surface defect (green) and with shear band formation at edge defect (red).

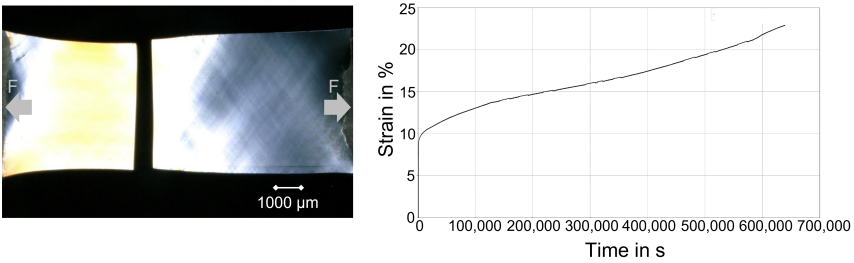

Figure 14: Creep curve of type A film sample with a thickness of 30 µm and a photoelastic image of the tested sample. The stress level was set to 42 MPa (= 60 % UTS).

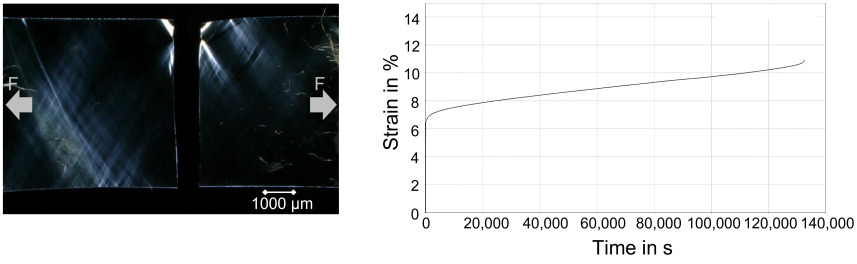

Figure 15: Creep curve of type A film sample with a thickness of 30 µm and a photoelastic image of the tested sample. The stress level was set to 45 MPa (= 65 % UTS)

.

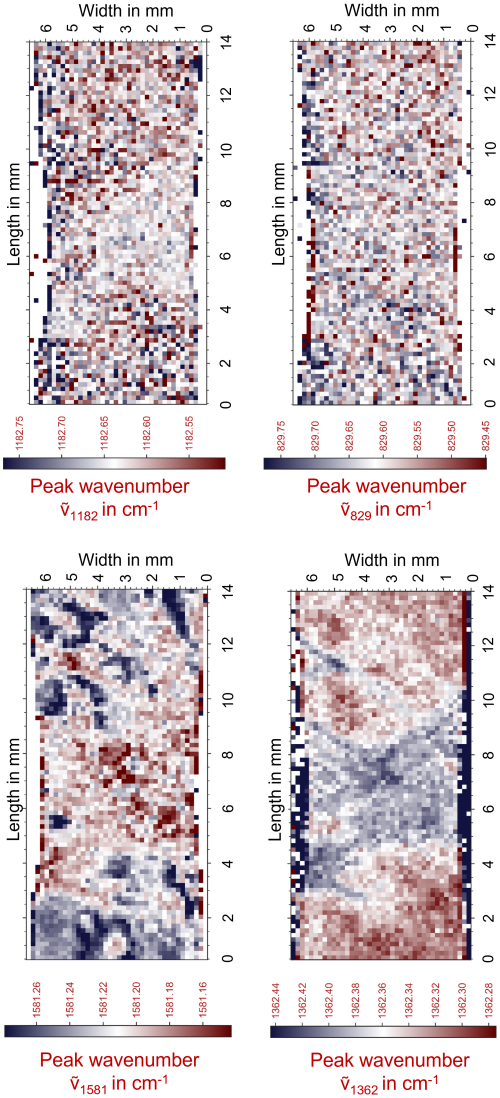

Figure 16: *Ex situ* IR microscope results of a representative creep-loaded film specimen of type A with a thickness of 30 µm without failing during the mechanical creep loading (maximum elongation of 17 %). Each pixel with a size of 165 x 165 µm is a measurement point and correspond to a spectrum. All recorded spectra are evaluated regarding the peak wavenumber $\tilde{\nu}_{829}$, $\tilde{\nu}_{1182}$, $\tilde{\nu}_{1362}$ and $\tilde{\nu}_{1581}$. Depending on the value of $\tilde{\nu}$, each pixel is colored. The corresponding photoelastic image and the visualization of the aromatic peak wavenumber $\tilde{\nu}_{1608}$ of this sample are shown in Figure 5.33.

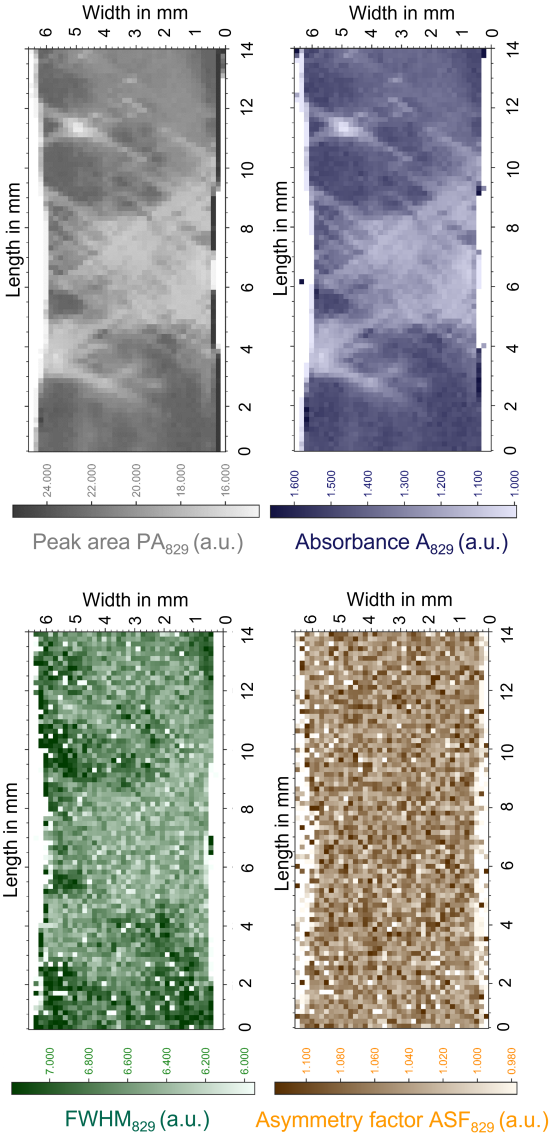

Figure 17: *Ex situ* IR microscope results of a representative creep-loaded film specimen of type A with a thickness of 30 µm without failing during the mechanical creep loading (maximum elongation of 17 %). Each pixel with a size of 165 x 165 µm is a measurement point and correspond to a spectrum. All recorded spectra are evaluated regarding the peak at 829 cm^{-1}. The absorbance (A_{829}), peak area (PA_{829}), asymmetry factor (ASF_{829}) and Full Width at Half Maximum ($FWHM_{829}$) are determined and visualized. The corresponding photoelastic image of this sample is shown in Figure 5.33.

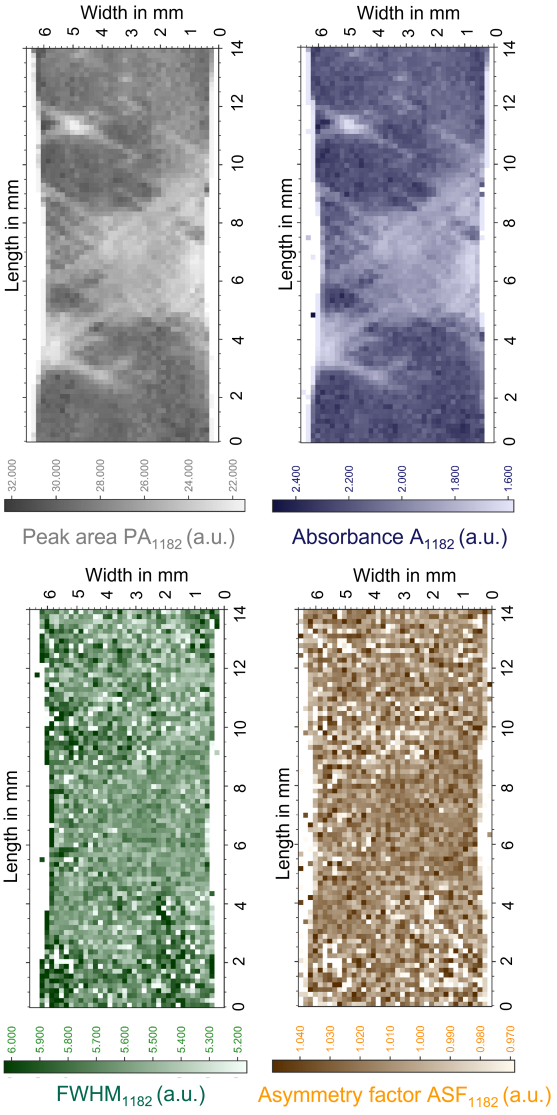

Figure 18: *Ex situ* IR microscope results of a representative creep-loaded film specimen of type A with a thickness of 30 µm without failing during the mechanical creep loading (maximum elongation of 17 %). Each pixel correspond to a spectrum. All recorded spectra are evaluated regarding the peak at 1182 cm^{-1}. The absorbance (A_{1182}), peak area (PA_{1182}), asymmetry factor (ASF_{1182}) and Full Width at Half Maximum ($FWHM_{1182}$) are determined and visualized. The corresponding photoelastic image of this sample is shown in Figure 5.33.

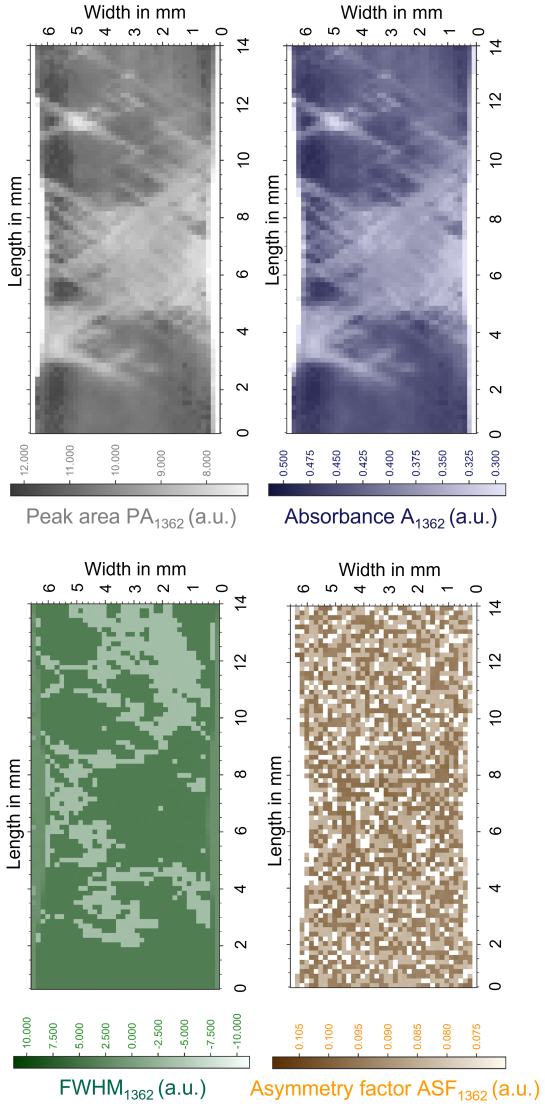

Figure 19: *Ex situ* IR microscope results of a representative creep-loaded film specimen of type A with a thickness of 30 µm without failing during the mechanical creep loading (maximum elongation of 17 %). Each pixel correspond to a spectrum. All recorded spectra are evaluated regarding the peak at 1362 cm^{-1}. The absorbance (A_{1362}), peak area (PA_{1362}), asymmetry factor (ASF_{1362}) and Full Width at Half Maximum ($FWHM_{1362}$) are determined and visualized. The corresponding photoelastic image of this sample is shown in Figure 5.33.

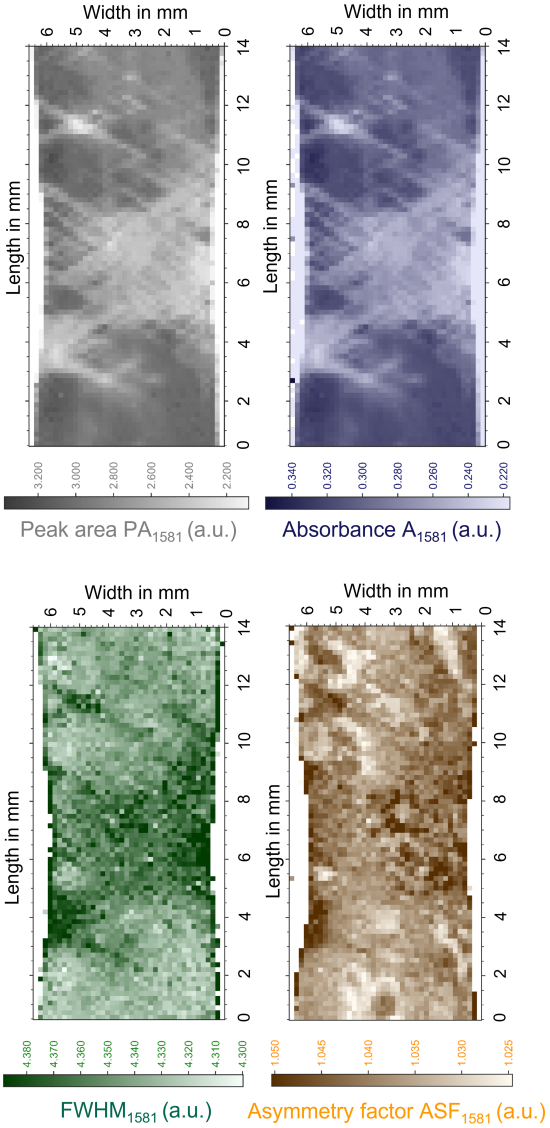

Figure 20: *Ex situ* IR microscope results of a representative creep-loaded film specimen of type A with a thickness of 30 µm without failing during the mechanical creep loading (maximum elongation of 17 %). Each pixel correspond to a spectrum. All recorded spectra are evaluated regarding the peak at 1581 cm^{-1}. The absorbance (A_{1581}), peak area (PA_{1581}), asymmetry factor (ASF_{1581}) and Full Width at Half Maximum ($FWHM_{1581}$) are determined and visualized. The corresponding photoelastic image of this sample is shown in Figure 5.33.

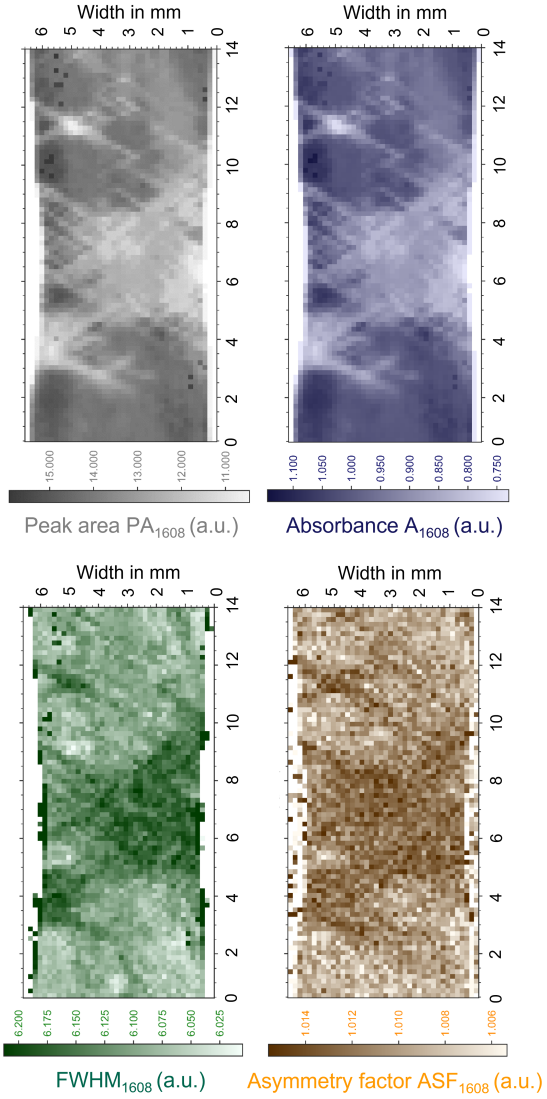

Figure 21: *Ex situ* IR microscope results of a representative creep-loaded film specimen of type A with a thickness of 30 µm without failing during the mechanical creep loading (maximum elongation of 17 %). All recorded spectra are evaluated regarding the peak at 1608 cm^{-1}. The absorbance (A_{1608}), peak area (PA_{1608}), asymmetry factor (ASF_{1608}) and Full Width at Half Maximum ($FWHM_{1608}$) are determined and visualized. The corresponding photoelastic image and the visualization of the peak wavenumber $\tilde{v}_{1608}$ of this sample are shown in Figure 5.33.

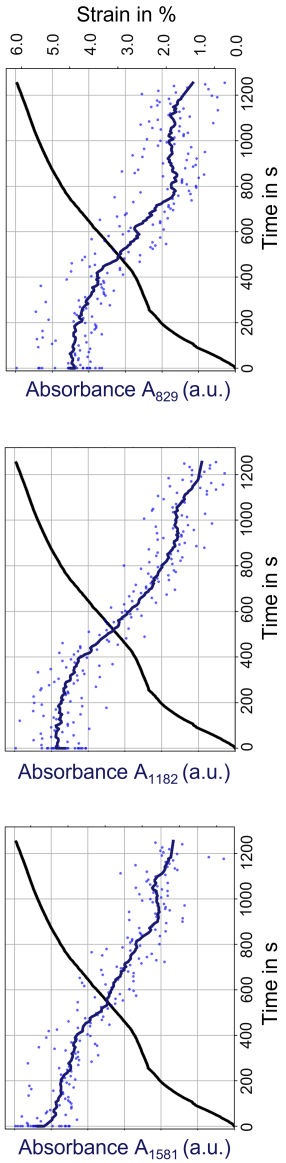

Figure 22: *In situ* tracked absorbance A_{829}, A_{1182} and A_{1581} (each blue dot represent a recorded and processed spectrum) over the time (fitted curve in blue) for type B film specimen with a thickness of 30 µm during creep loading (70 % UTS). The corresponding mechanical data is plotted as a black line.

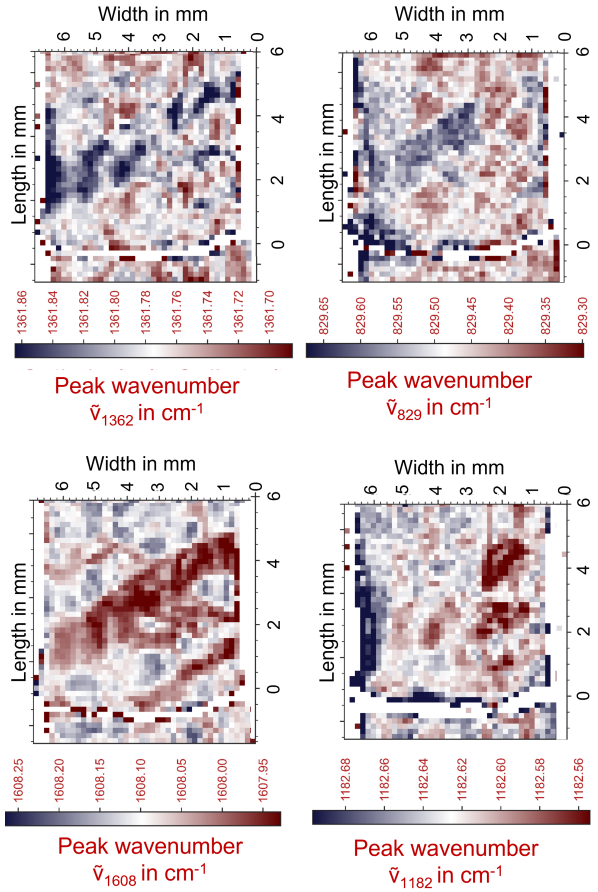

Figure 23: *Ex situ* IR microscope results of a representative film specimen of type A with a thickness of 15 µm after final failure during tensile testing. Each pixel with a size of 165 x 165 µm is a measurement point and correspond to a spectrum. All recorded spectra are evaluated regarding the peak wavenumber $\tilde{\nu}_{829}$, $\tilde{\nu}_{1182}$, $\tilde{\nu}_{1362}$ and $\tilde{\nu}_{1608}$. Depending on the value of $\tilde{\nu}$, each pixel is colored. The corresponding photoelastic image of this sample is shown in Figure 5.39.

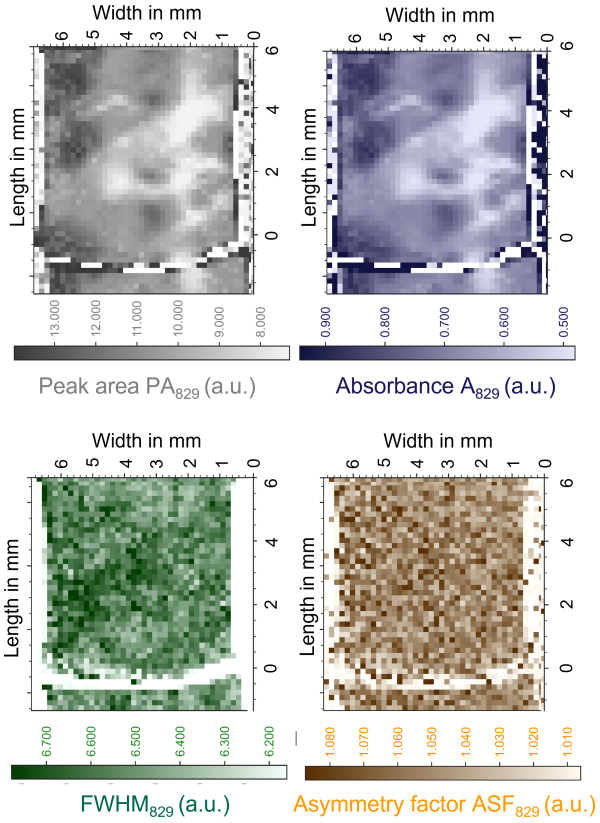

Figure 24: *Ex situ* IR microscope results of a representative film specimen of type A with a thickness of 15 µm with final failure during tensile testing. Each pixel with a size of 165 x 165 µm is a measurement point and correspond to a spectrum. All recorded spectra are evaluated regarding the peak at 829 cm^{-1}. The absorbance (A_{829}), peak area (PA_{829}), asymmetry factor (ASF_{829}) and Full Width at Half Maximum ($FWHM_{829}$) are determined and visualized. The corresponding photoelastic image of this sample is shown in Figure 5.39.

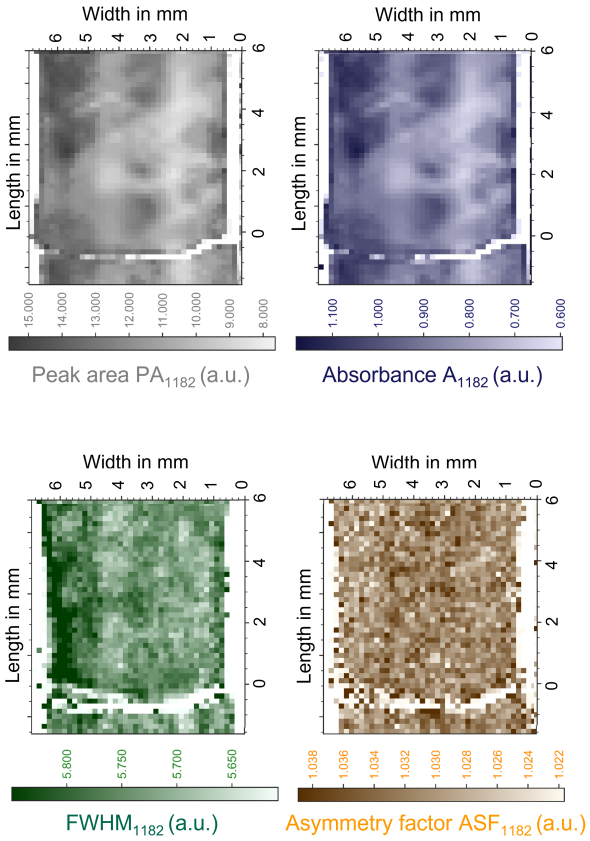

Figure 25: *Ex situ* IR microscope results of a representative film specimen of type A with a thickness of 15 µm with final failure during tensile testing. Each pixel correspond to a spectrum and all recorded spectra are evaluated regarding the peak at 1182 cm^{-1}. The absorbance (A_{1182}), peak area (PA_{1182}), asymmetry factor (ASF_{1182}) and Full Width at Half Maximum ($FWHM_{1182}$) are determined and visualized. The corresponding photoelastic image of this sample is shown in Figure 5.39.

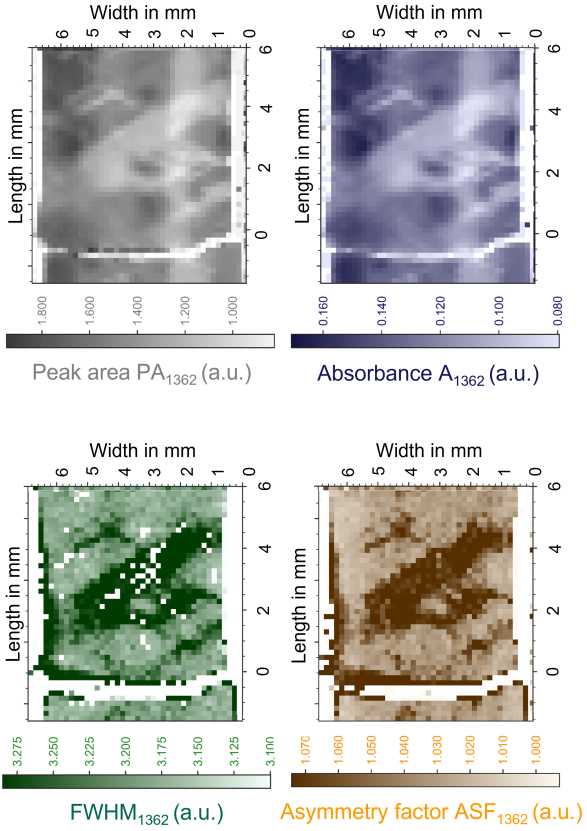

Figure 26: *Ex situ* IR microscope results of a representative film specimen of type A with a thickness of 15 µm with final failure during tensile testing. Each pixel correspond to a spectrum and all recorded spectra are evaluated regarding the peak at 1362 cm^{-1}. The absorbance (A_{1362}), peak area (PA_{1362}), asymmetry factor (ASF_{1362}) and Full Width at Half Maximum ($FWHM_{1362}$) are determined and visualized. The corresponding photoelastic image of this sample is shown in Figure 5.39.

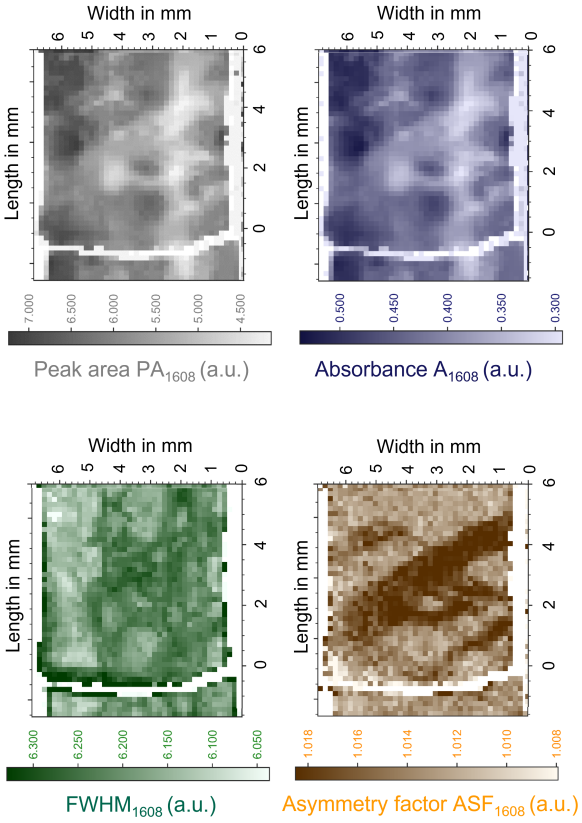

Figure 27: *Ex situ* IR microscope results of a representative film specimen of type A with a thickness of 15 µm with final failure during tensile testing. Each pixel correspond to a spectrum and all recorded spectra are evaluated regarding the peak at 1608 cm^{-1}. The absorbance (A_{1608}), peak area (PA_{1608}), asymmetry factor (ASF_{1608}) and Full Width at Half Maximum ($FWHM_{1608}$) are determined and visualized. The corresponding photoelastic image of this sample is shown in Figure 5.39.

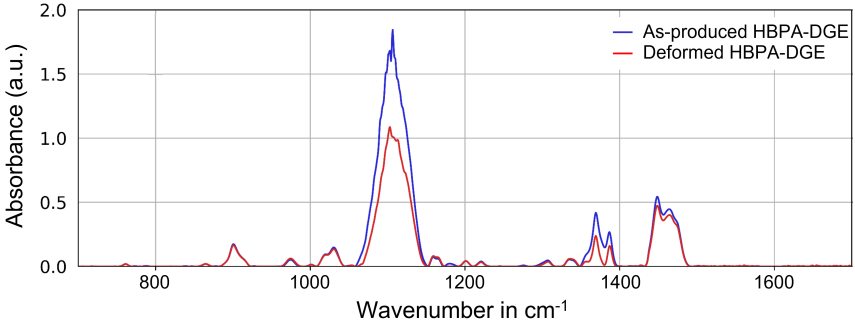

Figure 28: Spectrum of an as-produced type A HBPA-DGE film sample with a thickness of 30 µm (blue) and a spectrum recorded after tensile test in the deformed region of the same sample (red).

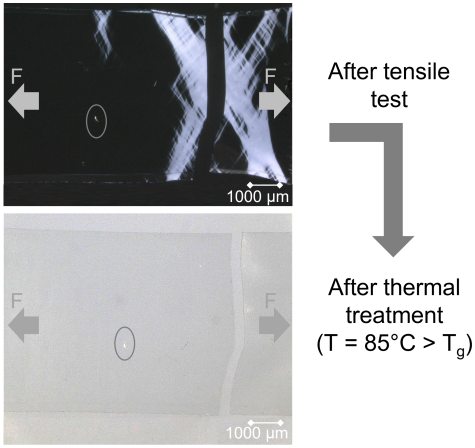

Figure 29: Photoelastic images of a HBPA-DGE type A film sample after tensile test and after subsequent thermal annealing at a temperature T of 85°C above the glass transition temperature T_g for 3 h. After the thermal annealing no shear bands and width reduction around the fracture are visible anymore. A small defect inside the sample (marked with a gray ellipse) which may be due to challenging handling during the tensile test remains after thermal annealing.